PERKIN ELMER

ELECTRO-OPTICAL DIVISION NORWALK, CONNECTICUT

ENGINEERING REPORT NO. 7994

FINAL TECHNICAL SUMMARY REPORT
INFLUENCE OF ATMOSPHERIC TURBULENCE ON
AZIMUTH LAYING TECHNIQUES

DATE: JUNE 15, 1965

PREPARED FOR: GEORGE C. MARSHALL SPACE FLIGHT CENTER

HUNTSVILLE, ALA.

Contract # NAS 8-11142
SPO 26296

Manager of Optical Instruments

Manager of Systems Programs

Contributors:
Frank Replogle

TABLE OF CONTENTS

TABLE OF CONTENTS (Con't)

APPENDICES

LIST OF ILLUSTRATIONS

LIST OF ILLUSTRATIONS (con't)

ABSTRACT

A serious limitation in the use of optical equipment in prelaunch alignment of missile guidance systems over long distances is imposed by the effects of atmospheric turbulence. The errors introduced in an instantaneous determination of the direction of a light beam are frequently the largest errors.

The purpose of this study is to find methods of predicting the size of the errors caused by atmospheric turbulence, and to compare such predictions with actual measurements made on a typical alignment theodolite. Another purpose is to investigate the possibility of modifying the design or use of such theodolites to reduce the errors.

Current theory of the transmission of light through a turbulent atmosphere predicts that the rms deviation of a collimated beam depends on the temperature gradient. Measurements were made to verify this dependence and determine the extent to which actual factors of proportionality can be predicted.

The random nature of the turbulence has been investigated and the theoretical form of the autocorrelation function and the power density spectrum determined. These functions have also been calculated from experimental data and comparison verifies the theoretical model. The use of the technique of modulation transfer functions enables the total performance to be predicted from measurements or calculations of the characteristics of the separate factors.

Theoretical and experimental comparison of the action of a roof prism and a trihedral lead to the conclusion that there is no correlation between the noise from these two types of return optics.

A discussion and bibliography on the subject of atmospheric attenuation in the visible and near infrared portion of the spectrum is included.

SECTION I

SUMMARY

1.1 INTRODUCTION

The problem which led to this study arises when theodolites are used for pre-launch alignment of missile guidance systems. The errors arising during such procedures due to the variation of the index of refraction of the atmosphere become significant when the required accuracy of the alignment is less than a minute of arc.

Similar effects have been observed by astronomers, by surveyors and by photographers working outdoors over long distances. Objects viewed along light paths passing over surfaces hotter than the atmosphere can be seen to vibrate. This phenomenon is called "shimmer" and is an exagerration of the phenomenon affecting alignment equipment. The errors in alignment as well as atmospheric shimmer are caused by thermal inhomogeneities in the atmosphere. In the case of visible shimmer, these inhomogeneities are carried across the field of view by convection while the errors in alignment measurements are usually moved at higher velocities across the field of view by air currents or wind. In either case, the motion is turbulent and our analysis starts with a consideration of atmospheric turbulence.

The causes of atmospheric turbulence may be found by a study of the thermodynamics of the earth-atmosphere-sunlight system. The factors of importance are the temperature and its variation with height above the ground,

the wind velocity, the humidity of the air and also of the topmost layer of the ground, as well as the transfer of heat between sun, air and ground. Not all of these factors will be considered in this report since a detailed thermodynamic analysis is beyond the scope of this study. Only those factors which are of direct utility in predicting the magnitude and temporal frequency of the errors in theodolite outputs due to atmospheric turbulence will concern us.

1.2 STATEMENT OF THE PROBLEM

The alignment procedure previously mentioned involves transmitting a collimated light beam through the intervening atmosphere, its reflection from a roof prism and its return to the theodolite again passing through the atmosphere. The motion of the roof prism in azimuth will result in the deviation of the wave front of the return beam and an error signal in the theodolite output. The effect of atmospheric turbulence is to distort the plane wavefront and to change its average direction. This also leads to error signals appearing in the theodolite output thus adding noise to the system and reducing its resolution and accuracy.

As the resolution of theodolites has improved, the errors added by atmospheric turbulence have become of increasing significance. The questions that arose were "What is the form of the error signal? Can it be predicted, can it be avoided or can it be compensated for?"

1.3 OBJECTIVES OF THE STUDY

The theodolite currently in use in prelaunch alignment is the Perkin-Elmer LR2A/GS Alignment Theodolite.

One object of this study was to measure the signals produced in the output of the LR2A/GS Alignment Theodolite by the turbulence in the atmosphere when the retro-prism is stationary. It was a further object to make measurements of atmospheric conditions and use current turbulence theory to predict the errors in theodolite readout and compare theory with actual measured results.

Since the meteorological measurements are taken at isolated points, they can only be used, in conjunction with theory, to predict general trends or average errors. In particular they can be used to predict the distribution of error as a function of its frequency. This prediction is then to be compared with the calculated power spectrum of the error signals to verify that the theory can indeed be applied to the instrument as used here.

A convenient measure of the error is the rms seeing error. This can also be predicted from the meteorological data or else calculated from microdensitometer traces over the image of a sharp edge transmitted over the range. The predictions were to be compared with measurements and thus establish the applicability of current theory to the prediction of seeing errors.

In considering the influence of the errors due to atmospheric turbulence on the design of alignment theodolites, we are led to a study of the effect of time of integration on the signals transmitted by the theodolite to the guidance platform. An analysis is to be made of the effect of integration and this compared with measurements of the power spectra and its effect on system design.

It has been suggested that the use of a trihedral and a roof prism simultaneously should lead to instrumental estimation of the seeing error. For this reason, a study was to be made of the effect of turbulence on the return beams from both these types of optical elements and measurements were to be made of actual error signals.

1.4 Summary of Experiments

A Perkin-Elmer model LR2A/GS Alignment Theodolite was set up on a range of 850 foot length at the Perkin-Elmer Corporation in Wilton, Connecticut, together with suitable return optics. In addition, instruments for measurement of temperature and wind velocity were disposed along this 850 foot path and readings of these meteorological parameters were taken while the deviations of the return beam to the theodolite were recorded on a strip chart recorder. Similar measurements were made at the launching site at Cape Kennedy.

The return optics used were a roof prism and a trihedral, the latter being used for a study of possible methods of compensation for errors due to atmospheric turbulence.

In a separate series of experiments, a square aperture was illuminated and the resulting object collimated and projected down the 850 foot range to a small telescope and a camera. The resulting photographs were processed and subjected to analysis by a microdensitometer whose output record was used to compute the modulation transfer function of the system and hence the modulation transfer function of the atmosphere.

The results of these experiments were used to compare predictions of the atmospheric seeing with actual measurements.

1.5 SUMMARY OF RESULTS

The predicted rms errors caused by atmospheric turbulence agree quite well with the current theory as far as their form is concerned. They show a linear dependence on the logarithmic temperature gradient although there is a difference between theory and measurement in the slope. The cause of this difference is to be found in the limitations in our experimental technique and equipment.

The Power Density Spectra of the noise in the instrumental output conforms to the theoretical predictions. This confirms again the validity of the theory and the preponderance of the errors with frequencies below 10 cps. This is one of the fundamental limitations to the improvement of performance azimuth alignment theodolites when they are used in systems with servos having response times of the order of large fractions of a second or greater.

The modulation transfer function of the atmosphere can be predicted or measured and its form used to predict system performance. Experimental results show the preponderant importance of this parameter in the over-all system transfer function. This leads to a suggestion for an economic study of the possible design criteria for future systems.

The effect of time of integration is found and although it is small, it is possible that in the future, with much larger launch vehicles being built, their much lower natural frequencies may enable the system designer to take advantage of this effect, to increase accuracy by increasing integration time. The possibility of using the return signal from a trihedral to compensate for the noise in the return signal of a roof prism was investigated. There does **not**

seem to be a practical method at this time. Finally, the advantage of selecting dawn and dusk as preferred times for take-off is graphically shown.

In general, the theory has been verified but there appears to be no straightforward method of significantly improving the present system. However, with continued study and the development of new systems, the guide lines developed in this report may indicate the direction for such improvements.

SECTION II

THE EFFECT OF METEOROLOGICAL CONDITIONS ON ATMOSPHERIC SEEING

2.1 DESCRIPTION OF INSTRUMENT

The instrument used in pre-launch alignment of the Saturn guidance package is the Perkin-Elmer LR2A/GS Alignment Theodolite. This instrument consists of a light source, a field divider, a telescope and detectors with associated optics, electronics and readout devices. Light from an incandescent source is chopped and allowed to fall alternately on the two reflective faces of the field divider, a "sensing prism." This prism is constructed so that there is a clear face (of dimensions 0.005" x 0.250") separating the reflective faces and the source optics forms two images of the filament of the lamp on the plane of this clear face. These images are then collimated by an 8 inch off-axis Maksutov catadioptric system of about 30 inch focal length and transmitted along a path of about 800 feet to a pair of roof prisms. These two prisms have their front faces dichroically coated so that the return beams can be separated by means of a dichroic filter so that the prisms can be monitored independently.

For the purposes of this study we are concerned only with the effect of the atmospheric turbulence on the position and shape of the return images of the lamp filament. These images are located in the plane of the narrow slit of the sensing prism and when there is no azimuth error in the

position of the retro-prisms none of the light* from these images passes through the (transparent) slit. However, when the images shift, one or the other image is partially transmitted through the slit and, since they are of opposite phase, both magnitude and direction of the azimuth error is detected.

A more detailed description of the principle of operation of this alignment theodolite will be found in Section V where the effects of actual operating parameters on seeing errors are considered.

It is readily seen that changes in size, shape or position of the images due to atmospheric disturbances can independently lead to error signals from a perfectly aligned return prism. Changes in position of the images are attributable to changes in the angle of arrival of the returning wavefront. Changes in shape and size are attributable to curvature of the returning wavefront. Since these latter are difficult to detect and measure whereas the output of the theodolite is given as the (equivalent) angle of the returning wavefront, all error signals are measured in angular measure (usually arc seconds).

2.2 BASIC SEEING THEORY

The effect of the turbulent atmosphere on the operation of azimuth alignment equipment, such as the Perkin-Elmer Model LR2A/GS, is best described in terms of the perturbation of the wavefronts of the return beam caused by

---

* It would be more correct to say that an equal amount of spill-over from each image takes place. These equal amounts are of opposite phase and are cancelled electrically after detection.

inhomogeneities in the atmosphere induced by turbulence. When the azimuth alignment equipment is operating, these perturbations are averaged over the theodolite aperture and can be equated to a net instantaneous tilt of the entire wavefront. Since the theodolite recovers information on the azimuth alignment of the target prism by measuring the tilt (angle of arrival) of the wavefronts reflected from the target prism, the equivalent net tilt of the wavefront due to atmospheric turbulence can be directly related to an equivalent apparent angular motion of the target prism.

One direct measure of this equivalent wavefront tilt is the value of the phase structure function as given in Equation 2.1 below. The phase structure function is defined as the average value of the mean squared difference in phase between two points on a reference plane perpendicular to the direction of propagation. For our analysis we use a reference plane in the theodolite aperture. Since non-deformed wavefronts are plane, and exhibit constant phase to any reference plane perpendicular to their direction of propagation, $D_S = 0$ for such planes. The phase structure function has a non-zero value only for perturbed wavefronts.

In terms of the phase structure function we can use Equation D-10 and D-11 to find the mean square wavefront deviation, $< S^2(p) >$, as

$$< S^2(p) > = \frac{D_s(p)}{k^2} = 2.91\, p^{5/3} \int_0^R C_N^2\,(z')\, dz' \qquad (2.1)$$

where $D_S(p)$ = phase structure function

p = separation of two points in the aperture

$C_N(z')$ = Structure function of the atmosphere

z' length along optical path

k wave number $\frac{2\pi}{\lambda}$

R total length of optical path

The structure function contains the functional dependence of the strength of the seeing upon the meteorological parameters describing the atmospheric driving. If we divide Equation 2.1 by p, and set p equal to the aperture width, we find

$$\sigma^2 = \frac{\langle S^2(p) \rangle}{p^2} \tag{2.2}$$

which represents the mean squared angular wavefront deformation, or tilt, resulting from the atmospheric turbulence. A more complete derivation of Equation 2.1 is found in Appendix D. It is shown there that the phase structure function, and thus the mean squared angle of arrival error, is a function of the 5/3 power of the aperture size. This follows from the Kolmogoroff nature of atmospheric turbulence.

In Appendix D, we find an expression (Equation D-11a) for the structure function of the atmosphere, C_N.

$$C_N = 1.3 \left| \frac{d\theta}{dh} + 0.98 \times 10^{-4} \right|^{-2/3} \times 0.9 \times 10^{-6} \tag{2.3}$$

where $\frac{d\theta}{dh}$ is the temperature gradient at altitude h.

For the turbulent layer of air several tens of meters thick lying near the earth's surface, the temperature follows a logarithmic law

$$\theta(h) = \theta + \theta^* \log \left(\frac{h}{ho} \right) \tag{2.4}$$

If we differentiate Equation (2.4) we obtain

$$\frac{d\theta}{dh} = \frac{\theta^*}{h} \tag{2.5}$$

where θ^* is a parameter equal to the logarithmic slope of the temperature gradient. It is worth noting that θ^* is the only meteorological parameter that appears when Equation 2.5 is substituted into Equation 2.3 and Equation 2.1. Thus C_N is a function of h only. The effect of all the basic meteorological driving factors, such as solar radiation levels, wind velocity, humidity, soil moisture, etc., is reflected in the value of the temperature gradient, hence only the temperature gradient need be measured to predict the magnitude of the effect of atmospheric turbulence.

If we substitute Equation 2.5 and 2.3 into Equation 2.1, we find

$$\sigma^2 = AB(2.91)(1.3)(0.9 \times 10^{-6})\, p^{5/3} \int_0^R C_N^2\,(h)\, dz' \tag{2.6}$$

where p = aperture width.

R = total length of path

A = 3.5 and corrects for the fact that the derivation of 2.1 in Appendix A is based on a single pass through the turbulent atmosphere, while the operation of azimuth laying equipment involves two passes.

B is an aperture correction factor calculated in Appendix D which takes into account the reduction in seeing that occur because of vertical averaging of the wavefront deviations that occurs over the aperture.

2.3 RMS SEEING AT WILTON

For the case of the nearly horizontal optical path employed at the Perkin-Elmer Seeing Range Facility, Equation 2.6 becomes,

$$\sigma^2 = AB\,(2.91)(1.3)(0.9 \times 10^{-6})\,p^{5/3}\,C_N^{\,2}\,(h_e)\,R \qquad (2.7)$$

where h_e - equivalent path altitude - 5.5 feet

R - one way path length 850 feet

p - 1.5 inch 0.125 foot

Evaluating and taking the root of Equation 2.7 yields

$$\sigma = 83 \times 10^{-6}\,\theta^* \text{ radians}$$

or $$\sigma = 17.1\,\theta^* \text{ arc seconds} \qquad (2.8)$$

2.4 RMS SEEING AT CAPE KENNEDY

For the range at Cape Kennedy where the elevation angle of the line of sight from the theodolite to the target prism is 25°, Equation 2.6 becomes,

$$\sigma^2 = \frac{10.4}{p^{1/3}} \int_{h_o}^{h_m} \frac{C_N^{\,2}(h)\,dh}{\sin \alpha} \qquad (2.9)$$

Performing the integration in 2.9 yields

$$\sigma = \frac{(31.2)^{1/2}\,(1.17 \times 10^{-6})}{p^{1/6}\,\sin \alpha}\,\theta^*\,\left[h_m^{\,1/3} - h_o^{\,1/3}\right]^{\frac{1}{2}} \qquad (2.10)$$

where p - aperture (2 inches or 0.167 feet)

α - elevation angle (25 degrees)

h_m - maximum height (185 feet)

h_o - minimum height (12 feet)

Evaluating Equation 2.10 yields

$$\alpha = 38.3 \times 10^{-6}\ \theta^{*} \text{ radians} \qquad (2.11)$$

or $\alpha = 7.9\ \theta^{*}$ arc seconds

2.5 EXPERIMENTAL RESULTS

Figures 2.1 and 2.2 illustrate the body of data taken at the Wilton, Conn. Seeing Range and at Cape Kennedy, Florida. The differences between the best fit lines and the theoretical lines arise from the approximate nature of the constants used in the derivation of Equations 2.8 and 2.11 while the large spread of the points results from the uncertainty in the value of θ^{*} calculated from experimental temperature data. The uncertainty in θ^{*} results from both variations in the temperature gradient that occur as a function of time as well as variations in the temperature gradient along the optical path resulting from the non-uniform surrounding terrain. Typical temperature gradient data, as shown in Figures 2.3, 2.4 and 2.5, illustrate the approximate nature of the calculated temperature gradients.

In order to reduce the effect of varying meterological conditions along the Wilton, Conn. path, temperature data was taken at three separate positions along the 850' line of sight of the theodolite. The positions were selected to cover different regions of the path where the immediate surrounding terrain was different from the terrain surrounding the other regions. A value of θ^{*} was calculated for each temperature station, and an average θ^{*} was then calculated from the θ^{*} obtained at each station. The data plotted reflects this attempt to average the temperature gradient along the path.

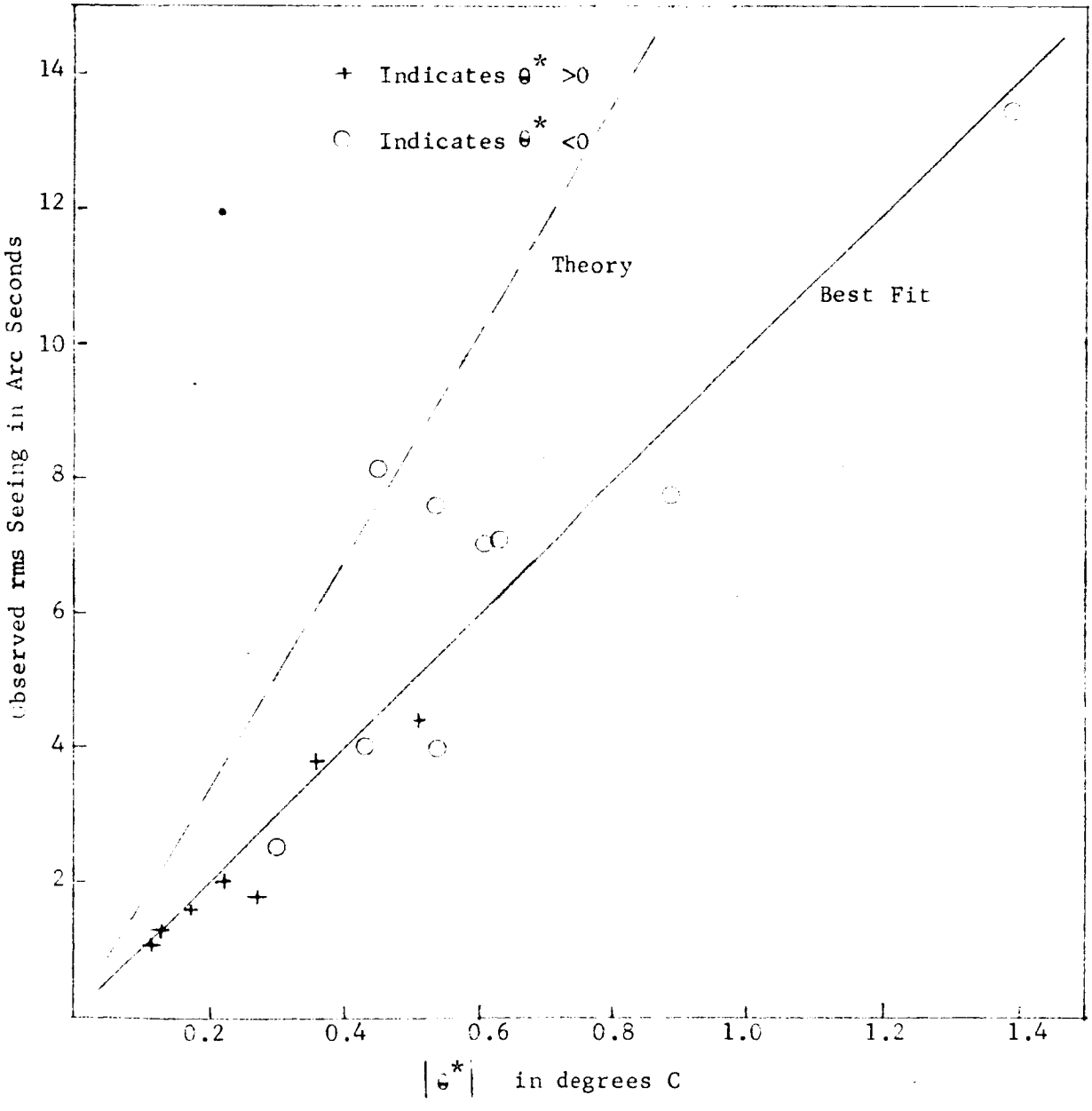

Figure 2.1 Theodolite Seeing Error vs. Characteristic Temperature For Data Taken at Wilton, Connecticut

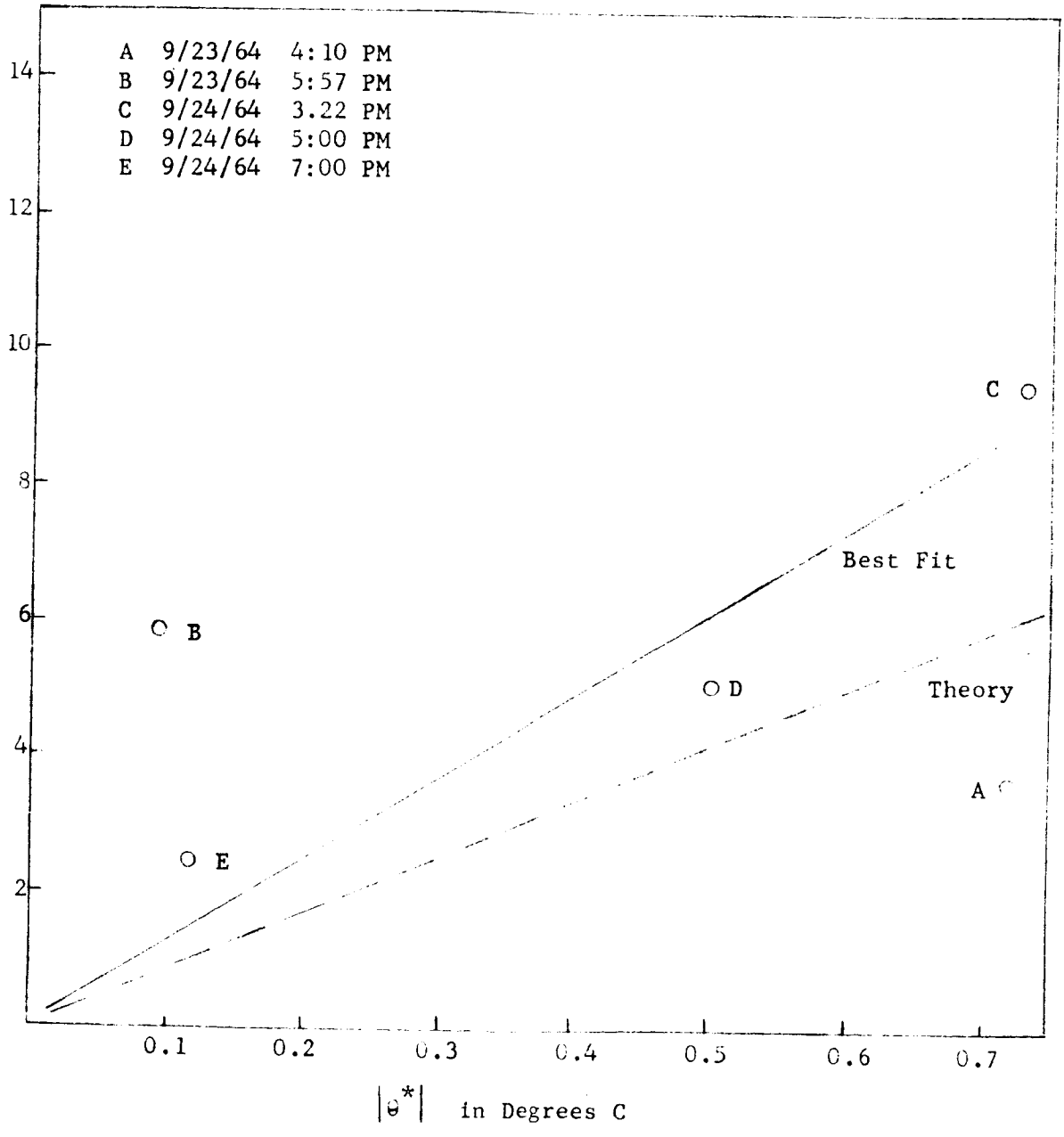

Figure 2.2. Theodolite Seeing Error vs Characteristic Temperature For Data Taken at Cape Kennedy

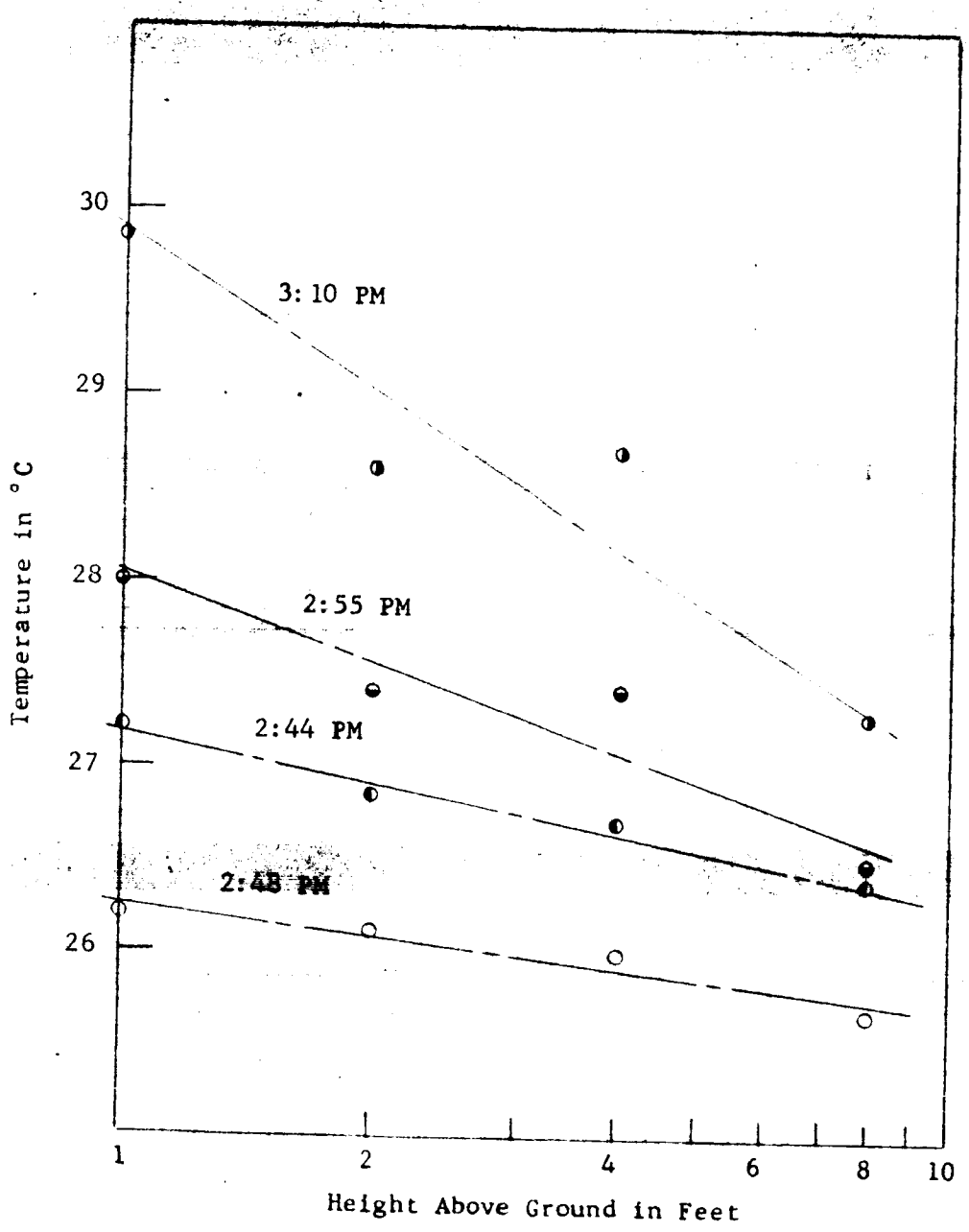

Location: Wilton Date: May 26, 1964

Conditions: Clear, gusts of 2 to 7 mph

Figure 2.3 Typical Temperature Profiles

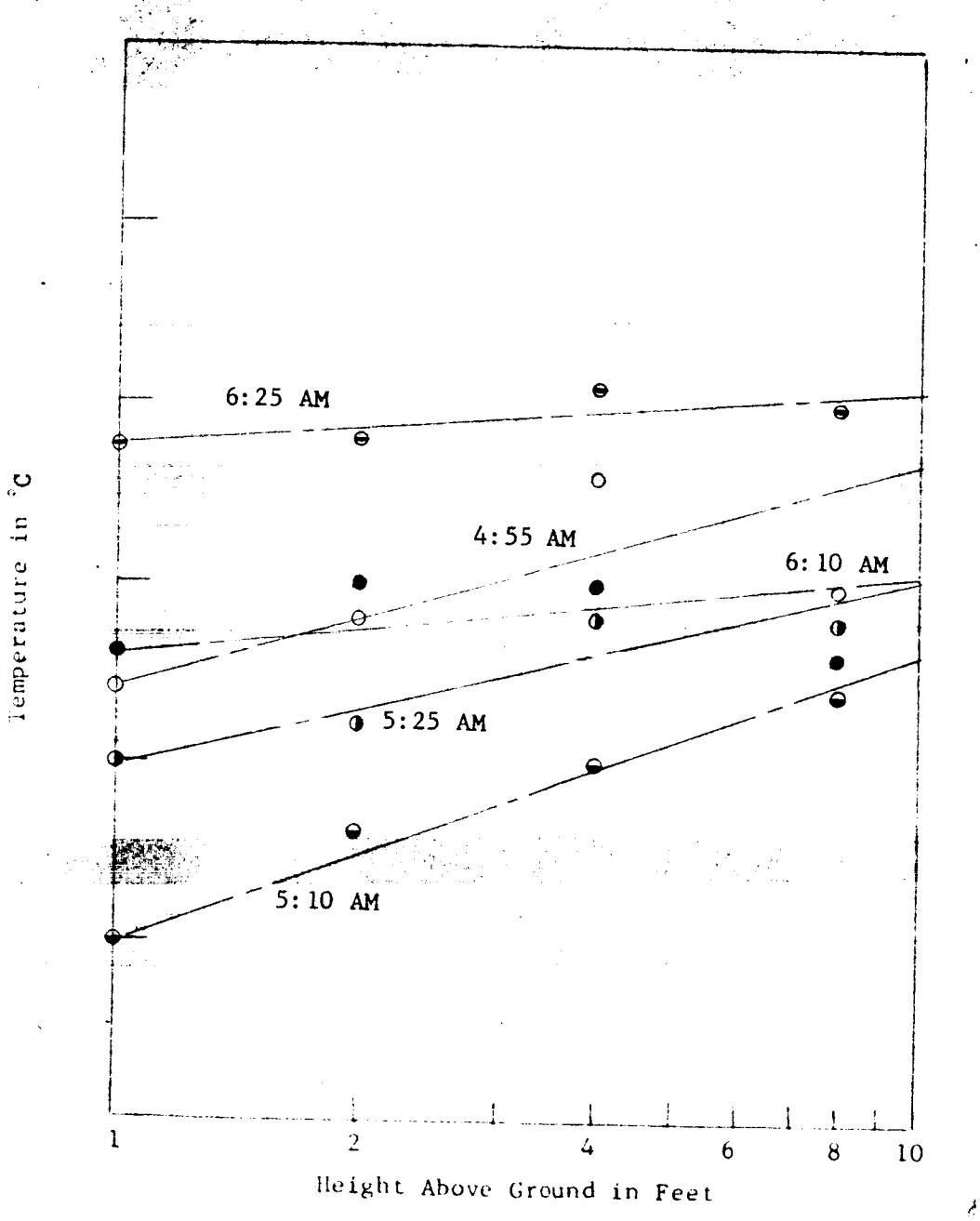

Location: Wilton Date: June 10, 1964

Conditions: Dawn, Clear, gusts of 2 to 7 mph

Figure 2.4 Typical Temperature Profiles

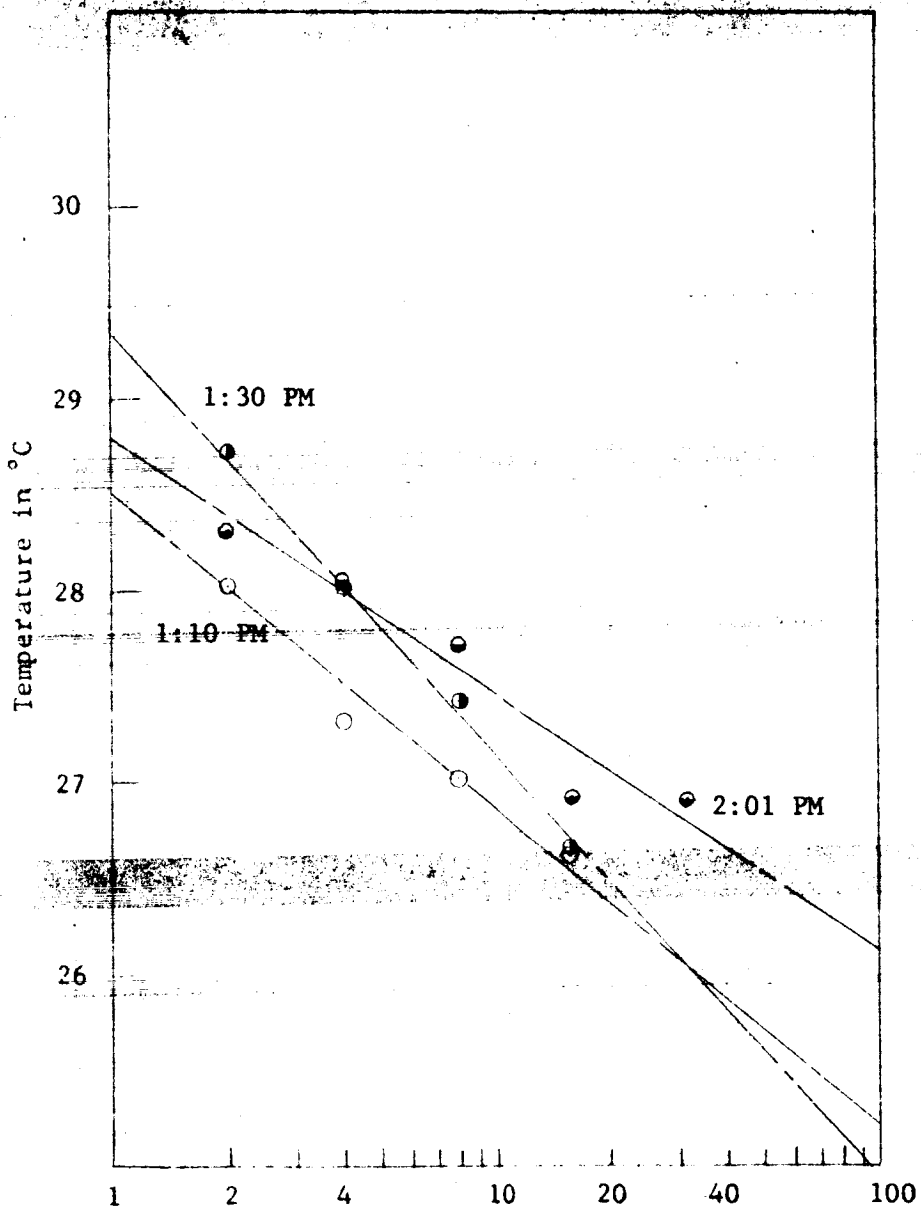

Location: Cape Kennedy Date: Sept. 23; 1964

Conditions: Clear, wind gusty 8 mph

Figure 2.5 Typical Temperature Profiles

The spread in the Cape Kennedy Data is due largely to the presence of a large amount of vibration of the gantry where the target prism was mounted. This vibration was caused by both elevators and other machinery in the gantry itself, and external windloading. The amplitude of the noise generated by these vibrations was quite large, and was found to be larger than the atmospheric induced noise for the data taken in the evenings. The natural frequency of the gantry vibrations, which was calculated to be 9.6 cycles per second, causes the noise peak seen at 9.6 cycles in the power spectrum shown in Figure 3.9, calculated from data taken at Cape Kennedy. The fact that the gantry vibration noise shows up at a given frequency permits a calculation of the atmospheric induced noise from data containing both atmospheric noise and large amounts of gantry noise. The spread of data in Figure 2.2, which has been calculated by this method (outlined in Section 3.3), results from the approximate nature of this calculation.

2.6 EFFECT OF THE TIME OF DAY

The intimate connection between the value of the gross meterological parameters which cause turbulence (such as the net heat flux between the ground and the lower atmosphere), and the observed errors is indicated in Figure 2.6, which shows the variation of the observed seeing error during the period of sunrise. Also shown is the value of θ^*, which reflects the effect of the net heat flux between the ground and the lower atmosphere. During daylight hours, when there is a net heat flux upward into the atmosphere, due to solar heating of the surface, the temperature profile has a negative slope (lapse), as shown in Figure 2.3. The mechanism of heat transfer under these circumstances is convection, and it is the vertical motion of convection cells

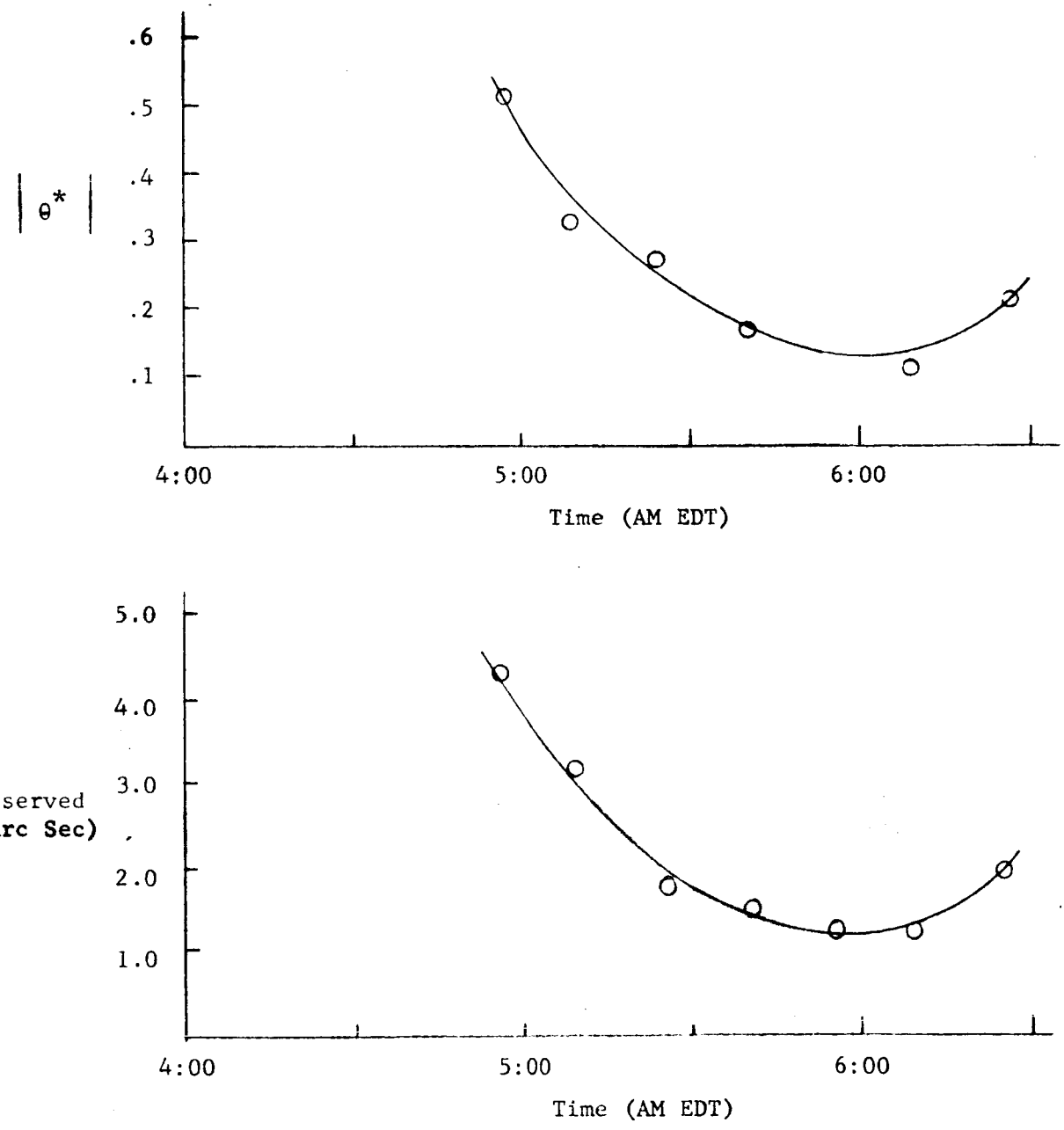

Figure 2.6 Atmosphere Seeing and Temperature Gradient at Sunrise

(turbulons) brought on by thermal buoyancy forces combined with the horizontal motion caused by wind that appears as turbulence.

As sunset approaches, solar heating of the surface decreases, causing the net heat flux up from the surface to decrease. Accompanying the resulting decrease in the temperature gradient is a decrease in the energy carried in the tubulons, which in turn results in a lowering of the strength of the seeing. At some time shortly after sunset, the net heat flux goes to zero, convection ceases, and temperature gradient goes to zero. When this condition occurs, conditions are at their best. Figure 2.7 illustrates this decrease in turbulence, for data taken at Cape Kennedy.

As night comes on, the temperature gradient becomes positive (inverted) as the earth's surface cools by radiating off into space the heat it absorbed during the day (Figure 2.4) Under these conditions, the turbulence of the atmospheric increases slightly from the minimum observed around sunset. Convection does not occur under these stable conditions and the strength of the seeing becomes a direct function of the transverse wind velocity.

When the sun comes up, the procedure reverses, and the observed seeing goes through a second minimum. Figure 2.6, which shows data taken at Wilton over a period of two hours including sunrise, shows the minimum that occurs shortly after sunrise.

For the data taken, there appears to be about a 5:1 ratio between mid-day seeing conditions and early morning seeing conditions. This fact suggests that the critical periods of pre-launch azimuth alignment should be arranged to coincide with either sunrise or sunset. The sunrise condition would

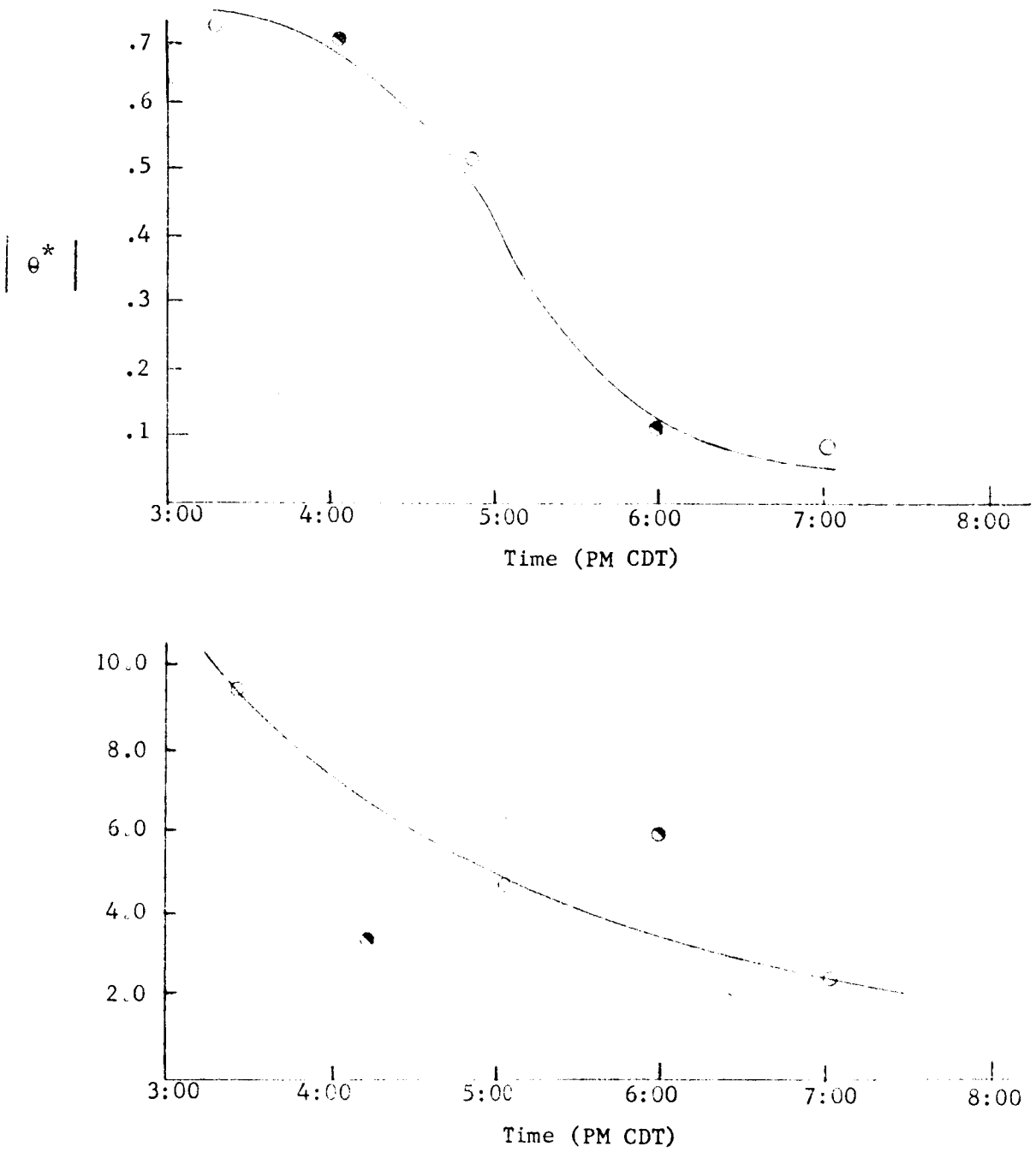

Figure 2.7 Atmospheric Seeing and Temperature Gradient Sunset

be more satisfactory, since atmospheric conditions are more stable, causing a more prolonged transition period between the lapse and inversion conditions.

2 7 SUMMARY

In summary, the theory appears to successfully precict the magnitude of the turbulence over a wide range of meteorological conditions for the path geometry at Wilton. The maximum error displayed by the spread of the points shown in Figure 2.1 appears to be a factor of two, which is not an inordinately large error considering the uncertainties involved in determining the temperature gradients. The presence of the large gantry vibrations prevent any definite conclusion on errors inherent in the theory when applied to the Cape Kennedy range. However, within the range of uncertainty shown in Figure 2.2, the theory does appear to hold.

SECTION III

POWER SPECTRUM OF ATMOSPHERIC SEEING

3.1 INTRODUCTION

Since the long range azimuth laying theodolites are designed to operate in a servo loop with a fixed time constant, an investigation of the power spectrum of the spurious error signals induced by atmospheric turbulence has been made.

This information is presented in three forms:

a) Graphs of the autocorrelation function of theodolite error signals.

b) Graphs of the noise power spectrum of atmospheric turbulence shown in units of arc seconds squared per cycle per second vs. frequency.

c) Discussion of the division of the noise power spectrum into two frequency regions; the low frequency noise being generated primarily by the phenamenon of image shift, and the high frequency noise being generated primarily by image blur.

A description of atmospheric turbulence in the frequency domain will make it possible to apply standard methods of electric network analysis to the real problem of reducing the effect of noise generated in a closed loop system with a characteristic time constant.

3.2 THEORETICAL FORM OF AUTOCORRELATION FUNCTION OF ATMOSPHERIC NOISE

For a theodolite using a roof prism as a target, it is sufficient to calculate the form of the power spectrum for a beam traversing a turbulent atmosphere in one direction since the statistics of the atmosphere penetrated on the second pass is identical to the statistics of the atmosphere penetrated on the first pass. The only effect of the second pass is to increase the amplitude of the atmospheric induced error.

The power spectrum is found by taking the Fourier Transform of the autocorrelation function and this paragraph is devoted to finding the latter.

The signal in one phase of the detector output of the theodolite is proportional to the shift in the center of gravity of the image of the portion of the filament of the source lamp falling on the corresponding side of the slit of the sensing prism. Consider the case of the formation of the image by the theodolite when it is illuminated by the deformed wavefront shown in Figure 3.1. Although the wavefront shown corresponds only to a particular point on the extended filament, the resultant deformation of the point image, and the shift of its center of gravity, also applies to every other point contained in the total extended image.

The center of gravity of the image, $\bar{y}$, is given by

$$\bar{y} = \int_0^D I(y)\, F\, \frac{d\varphi(y)}{dy}\, dy \qquad (3.1)$$

where

$I(y)$ = distribution of intensity

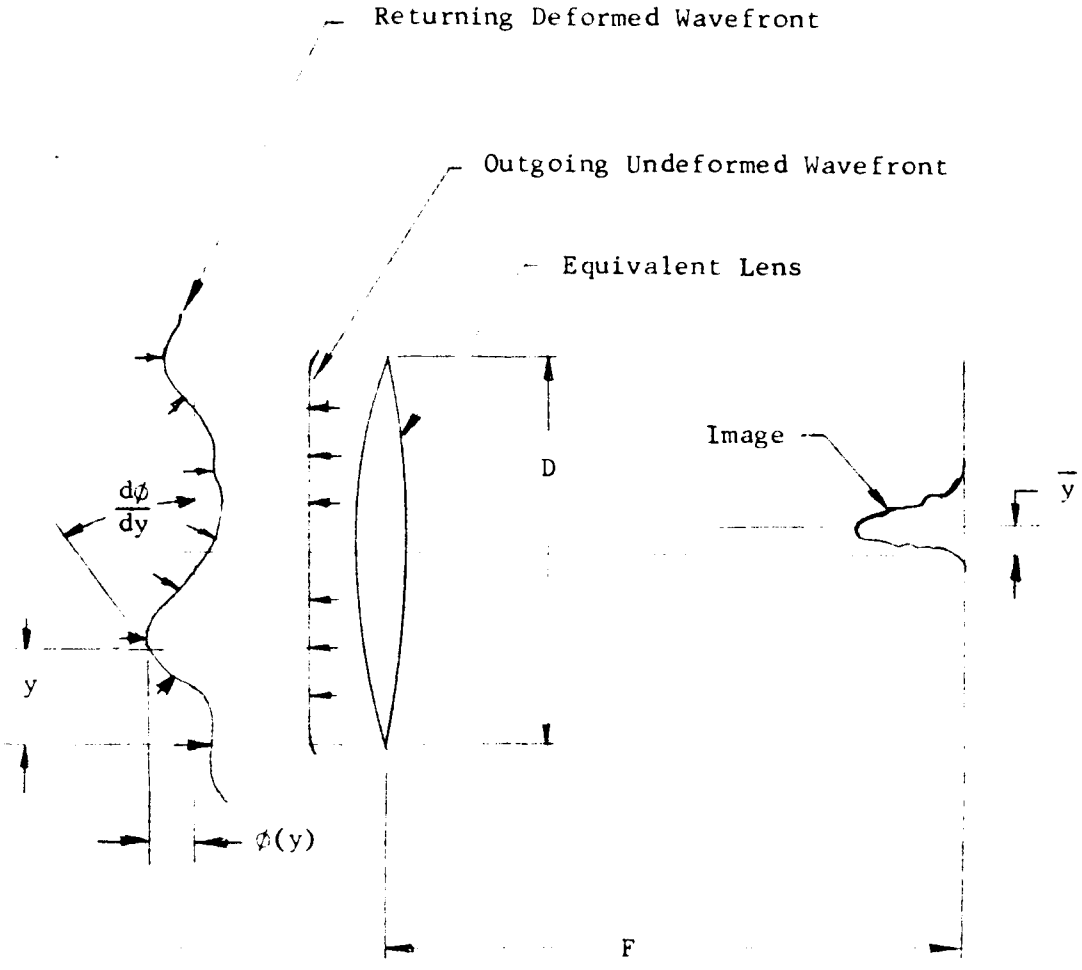

Figure 3.1. Notation for Analysis of Image Formation

F = focal length of system

$d\phi/dy$ = angle of arrival of wavefront

Let $I(y)$ be constant over the aperture, and equal to $1/FD$, then we can write

$$\bar{y} = \int_o^D \frac{1}{D} \frac{d\phi(y)}{dy} dy = \frac{\phi(D) - \phi(o)}{D} \tag{3.2}$$

The wavefront deviations will be a projection of the atmospheric refractive properties and will move laterally with the speed of the transverse component of the wind. Thus

$$\phi(y,t) = \phi(y-vt) \tag{3.3}$$

where v is the transverse wind component. Substitution of (3.3) into (3.2) yields

$$\bar{y}(t) = \left[\phi(D-vt)-\phi(-vt)\right]/D$$

The autocorrelation function of $\bar{y}$ for a temporal lag, τ, is given by

$$A(\tau) = \left\langle \bar{y}(t)\, \bar{y}(t+\tau) \right\rangle$$

$$= D^{-2} \left\langle \left[\phi(D) - \phi(o)\right] \left[\phi(D-v\tau)-\phi(-v\tau)\right] \right\rangle$$

This may be written as

$$A(\tau) = \frac{D^{-2}}{2} \left\langle \left[\phi(D)-\phi(-v\tau)\right]^2 \right\rangle + \frac{D^{-2}}{2} \left\langle \left[\phi(o)-\phi(D-v\tau)\right]^2 \right\rangle$$

$$- \frac{D^{-2}}{2} \left\langle \left[\phi(D)-\phi(D-v\tau)\right]^2 \right\rangle - \frac{D^{-2}}{2} \left\langle \left[\phi(o)-\phi(-v\tau)\right]^2 \right\rangle \tag{3.4}$$

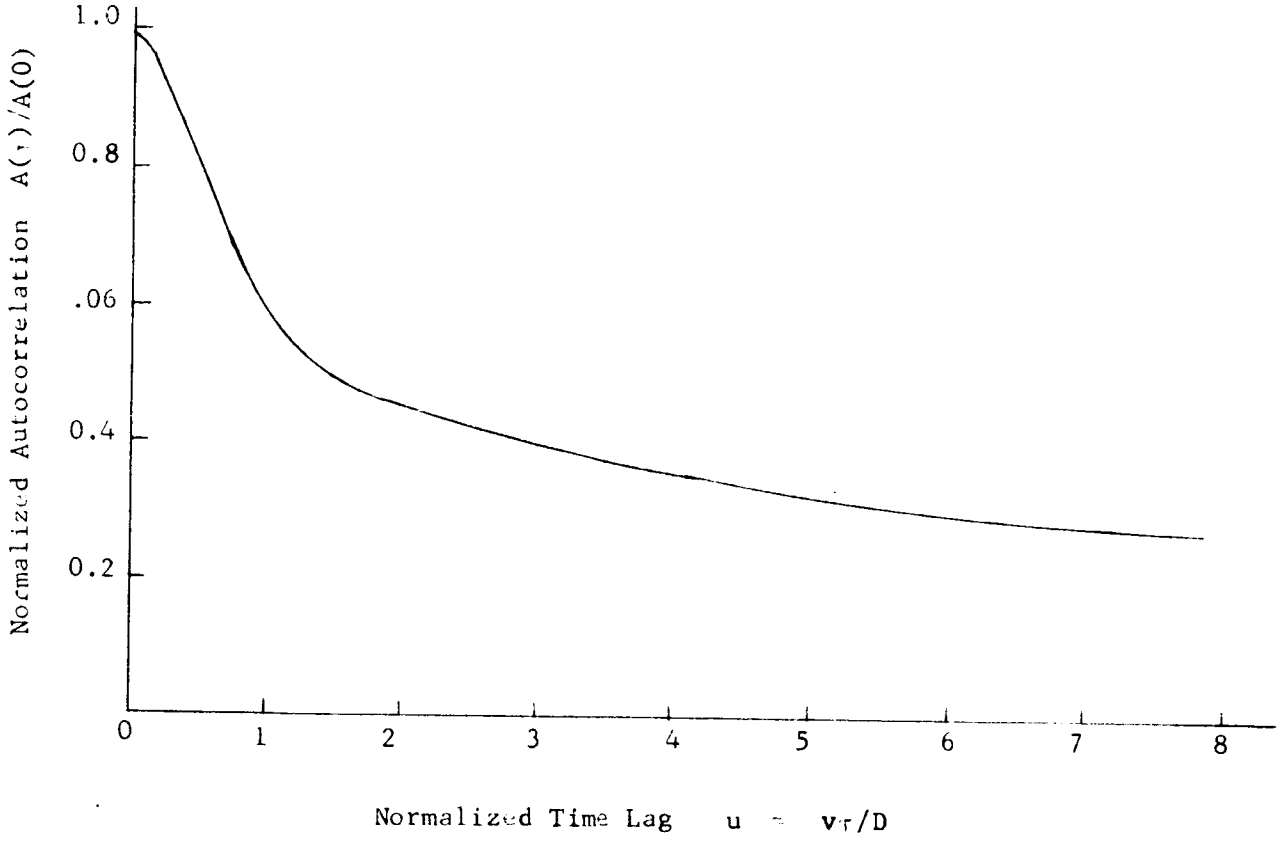

Figure 3.2 Theoretical Form of the Autocorrelation Function for Atmospheric Noise

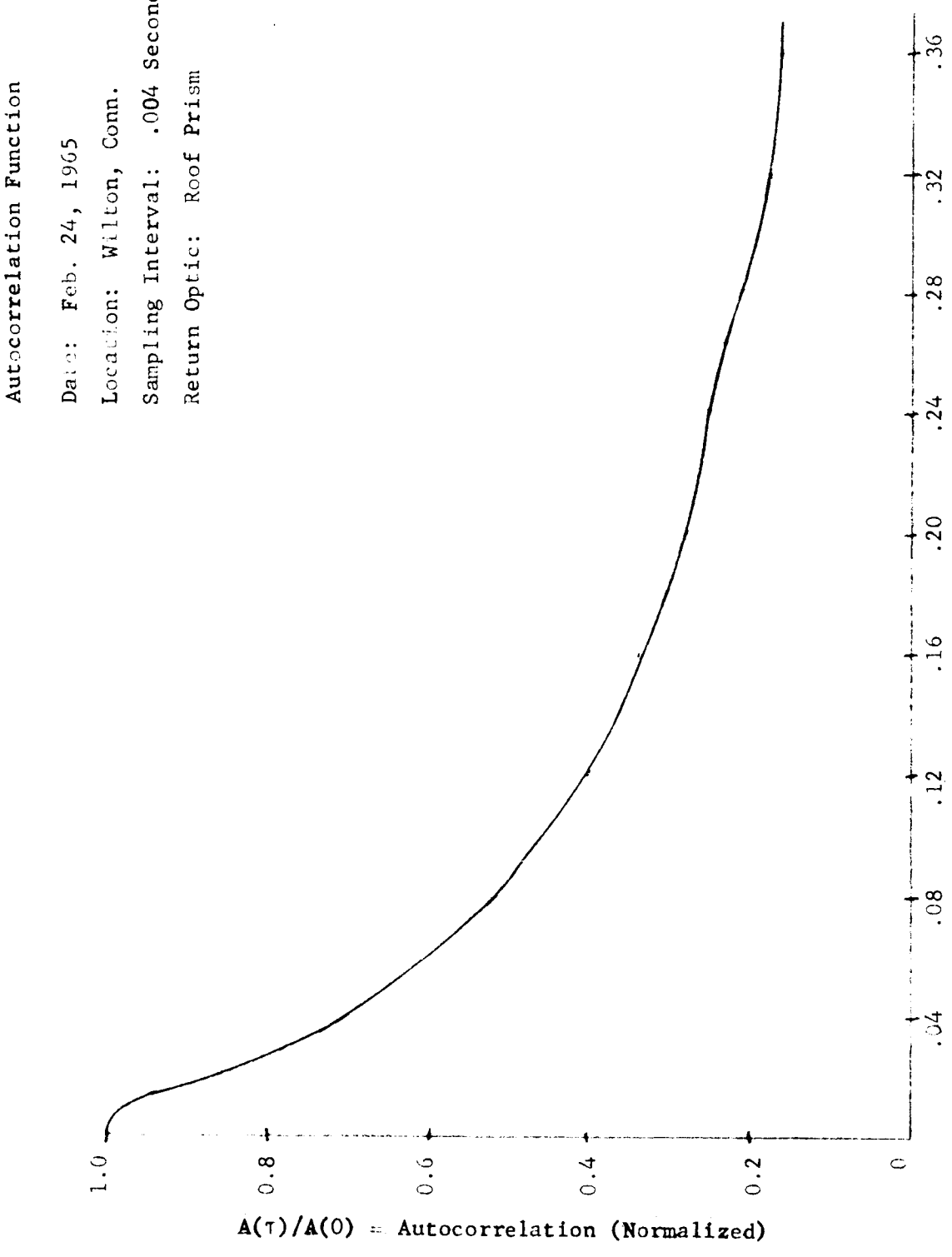

Figure 3.3 Autocorrelation Function for Atmospheric Noise

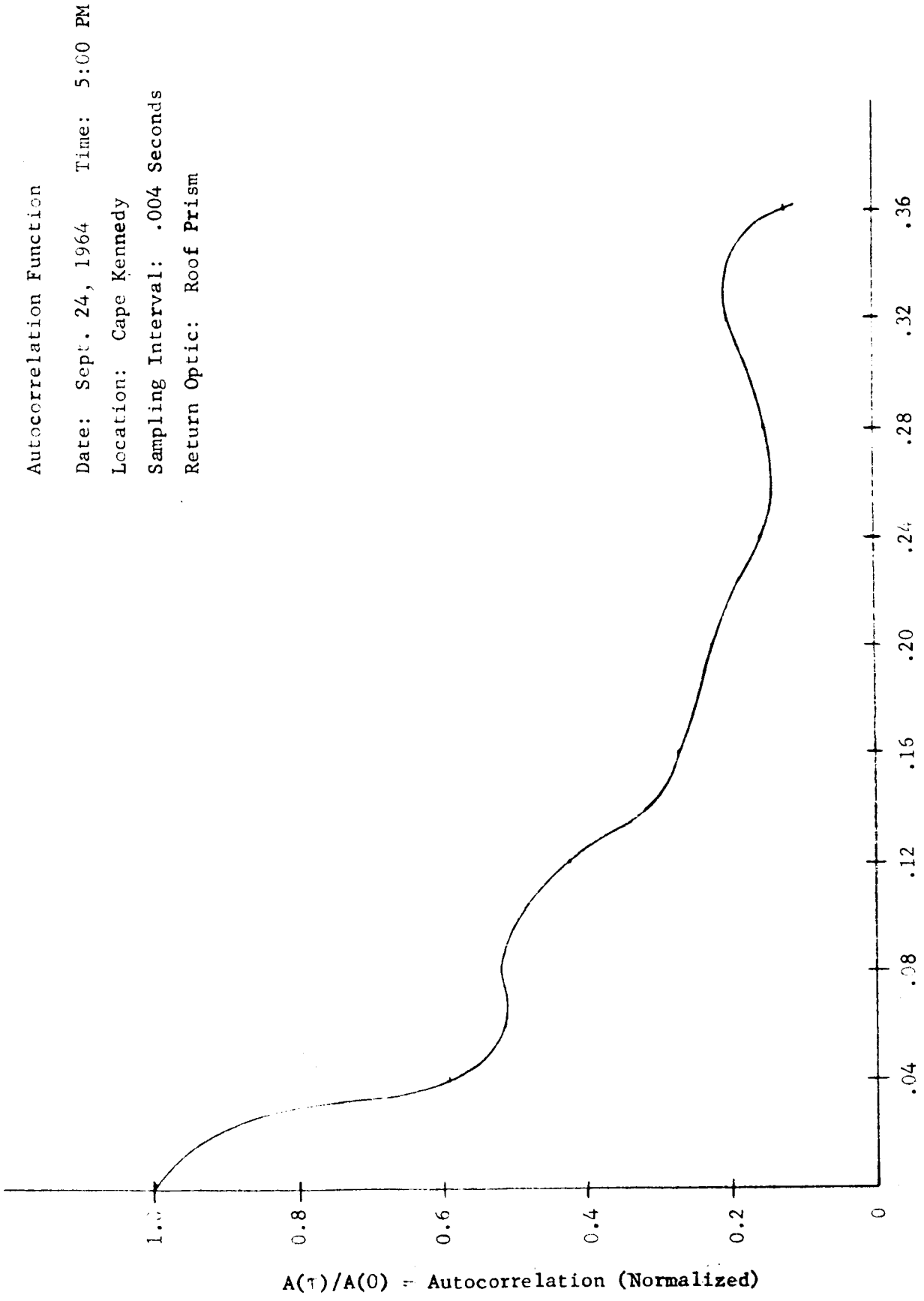

Figure 3.4 Autocorrelation Function for Atmospheric Noise

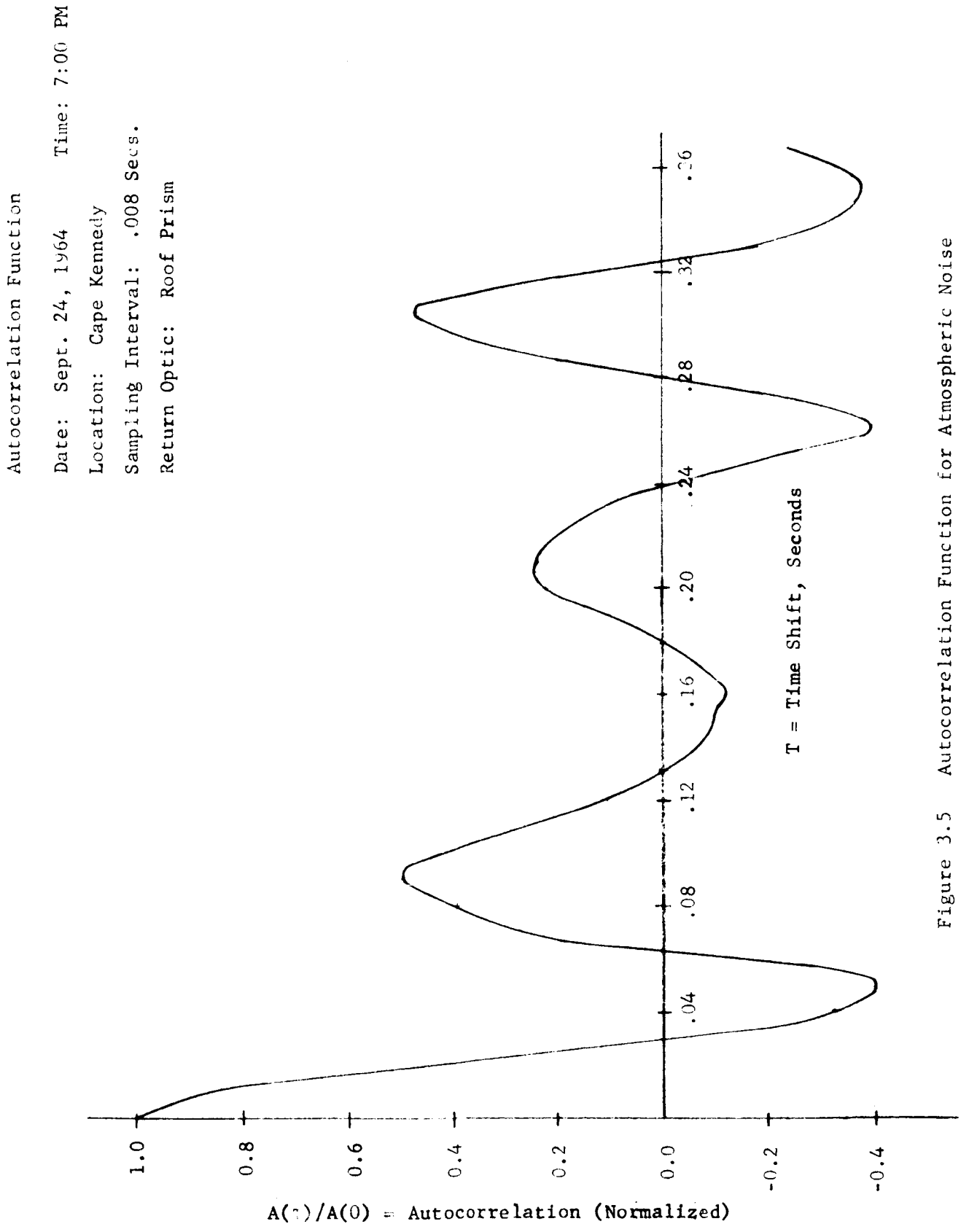

Figure 3.5 Autocorrelation Function for Atmospheric Noise

A result of the Kolmogoroff nature of atmospheric turbulence is that the quantity $\left\langle \left[\phi(x_1)-\phi(x_2)\right]^2 \right\rangle$ is proportional to $|x_1-x_2|^{5/3}$ and the above can be expressed as

$$A(\tau) = \frac{A(o)}{2}\left[\,|1+u|^{5/3} + |1-u|^{5/3} - 2u^{5/3}\,\right] \qquad (3.5)$$

where $u = v\tau/D$ is a normalized time tag and A(o) is the mean squared angular deviation, which is equation (6) evaluated for $\tau = 0$.

Figure 3.2 is a plot of $A(\tau)/A(o)$ vs. u. For large u the curve is asymptotic to $(5/9)\,u^{-1/3}$. This curve is valid only for a horizontal light path and for small vertical size of the limiting aperture.

Figures 3.3, 3.4, and 3.5 show autocorrelation functions calculated from data taken at Cape Kennedy and at Perkin-Elmer. Figure 3.3 shows the autocorrelation function calculated from data taken at Norwalk that contained no detectable extraneous error signals. Its shape is very nearly the same as the shape of the predicted theoretical curve shown in Figure 3.2.

Figure 3.4 shows an autocorrelation function of the data taken at Cape Kennedy with the target prism mounted on the Saturn Gantry. This data was taken at 4:30 P.M. on September 23, 1964 and the gantry motion introduced a spurious sinusoidal error signal. This spurious signal appears in the calculated autocorrelation function as a sinusoidal function added to the autocorrelation function of the atmospheric noise.

Figure 3.5 shows an autocorrelation function calculated from data taken at Cape Kennedy at 7:00 P.M. on September 24, 1964. By 7:00 P.M. the

atmospheric seeing conditions had improved, but the magnitude of the gantry vibrations had not diminished. The autocorrelation function shows a more pronounced sinusoidal characteristic than the curve calculated from data taken at 4:30 P.M., resulting from the relative increase in the magnitude of the gantry-induced error signal caused by the reduced magnitude of the atmospherically induced error signal.

3.3 SEEING ERROR DUE TO GANTRY VIBRATIONS

A rough measure of the fraction of energy contained in the gantry vibrations can be found as follows:

Let

$F(t)$ = random noise produced by atmospheric turbulence

$B \sin \omega t$ = signal produced by gantry vibration

Then the normalized autocorrelation function of the combined signal

$$S(t) = F(t) + B \sin \omega t,$$

is equal to

$$A(\tau) = \frac{\lim_{T \to \infty} \frac{1}{T} \int_{-T/2}^{T/2} S(t)\, S(t+\tau)\, dt}{\lim_{T \to \infty} \frac{1}{T} \int_{-T/2}^{T/2} S^2(t)\, dt}$$

Let us evaluate

$$\int_{-T/2}^{T/2} S^2(t)\,dt = \int_{-T/2}^{T/2} \left[F^2(t) + 2F(t)\ B\sin\omega t + B^2 \sin^2\omega t\right] dt$$

or

$$\int_{-T/2}^{T/2} S^2(t)\,dt = \int_{-T/2}^{T/2} F^2(t)\,dt + 2B \int_{-T/2}^{T/2} F(t)\ \sin\omega t\ dt + B^2 \int_{-T/2}^{T/2} \sin^2\omega t\ dt \tag{3.6}$$

where we have assumed B to be independent of t.

The second term is just the correlation of the two noise inputs evaluated for zero time shift. Since they are uncorrelated, this term is zero. Thus Equation (3.6) becomes

$$\int_{-T/2}^{T/2} S^2(t)\,dt = \int_{-T/2}^{T/2} F^2(t)\,dt + B^2 \int_{-T/2}^{T/2} \sin^2\omega t\ dt \tag{3.7}$$

Equation (3.7) represents the total energy contained in the two noise components. Now we can evaluate $A(\tau)$:

$$A(\tau) = \frac{\lim_{T\to\infty} \int_{-T/2}^{T/2} \left[F(t) + B\sin\omega t\right]\left[F(t+\tau) + B\sin\omega(t+\tau)\right] dt}{\lim_{T\to\infty} \left[\int_{-T/2}^{T/2} F^2(t)\,dt + B^2 \int_{-T/2}^{T/2} \sin^2\omega t\ dt\right]}$$

$$A(\tau) = \frac{\lim_{T\to\infty}\left\{\int_{-T/2}^{T/2} F(t)F(t+\tau)dt + B\int_{-T/2}^{T/2} F(t)\sin(t+\tau)\,dt + B\int_{-T/2}^{T/2} F(t+\tau)\sin\omega t\,dt + B^2\int_{-T/2}^{T/2}\sin\omega t\sin\omega(t+\tau)\,dt\right\}}{\lim_{T\to\infty}\left\{\int_{-T/2}^{T/2} F^2(t)dt + B^2\int_{-T/2}^{T/2}\sin^2\omega t\,dt\right\}} \qquad (3.8)$$

The first term of the numerator is just the un-normalized autocorrelation function of the random (atmospheric) noise.

The second and third integrals in the numerator are cross-correlation functions between the atmospheric and gantry noise. Since these two noise signals are independent, they are uncorrelated, and the two integrals go to zero.

The fourth term can be simplified by expanding $\sin\omega(t+\tau)$. It becomes

$$B^2\int_{-T/2}^{T/2}\sin\omega t\sin\omega(t+\tau)\,dt$$

$$= B^2\cos\omega\tau\int_{-T/2}^{T/2}\sin^2\omega t\,dt + B^2\sin\omega\tau\int_{-T/2}^{T/2}\sin\omega t\cos\omega t\,dt$$

But

$$\int_{-T/2}^{T/2}\sin\omega t\cos\omega t\,dt = 0$$

Hence, Equation (3.8) becomes

$$A(\tau) = \frac{\int_{-T/2}^{T/2} F(t)F(t+\tau)dt + B^2 \cos\omega\tau \int_{-T/2}^{T/2} \sin^2\omega t dt}{\int_{-T/2}^{T/2} F^2(t)dt + B^2 \int_{-T/2}^{T/2} \sin^2\omega t dt} \qquad (3.9)$$

If we re-introduce the complete notation of autocorrelation functions, we can write

$$\lim_{T\to\infty} \frac{1}{T} \int_{-T/2}^{T/2} F^2(t)dt = \sigma_a^2$$

and

$$\lim_{T\to\infty} \frac{1}{T} \int_{-T/2}^{T/2} \sin^2\omega t dt = \sigma_g^2$$

where σ_a^2 and σ_g^2 are the average rates of noise energy being produced by the atmosphere and the gantry, respectively.

We then define the ratios

α, β and $A_a(\tau)$ as

$$\alpha = \frac{\sigma_a^2}{\sigma_a^2 + \sigma_g^2} = \frac{\int_{-T/2}^{T/2} F^2(t)dt}{\int_{-T/2}^{T/2} F^2(t)dt + B^2 \int_{-T/2}^{T/2} \sin^2\omega t dt} \qquad (3.10)$$

$$\beta = \frac{\sigma_g^2}{\sigma_a^2 + \sigma_g^2} = \frac{B^2 \int_{-T/2}^{T/2} \sin^2 \omega t \, dt}{\int_{-T/2}^{T/2} F^2(t)\,dt + B^2 \int_{-T/2}^{T/2} \sin^2 \omega t \, dt} \tag{3.11}$$

and

$$a_a(\tau) = \frac{\lim_{T \to \infty} \frac{1}{T} \int_{-T/2}^{T/2} F(t)F(t+\tau)\,dt}{\lim_{T \to \infty} \frac{1}{T} \int_{-T/2}^{T/2} F^2(t)\,dt} \tag{3.12}$$

then Equation (3.9) becomes

$$A(\tau) = a_a(\tau) + \beta \cos \omega \tau \tag{3.13}$$

Now consider the effect of letting τ grow out of all bounds. The numerator of (3.12) vanishes and

$$\lim_{T \to \infty} A(\tau) = \beta \cos \omega \tau \tag{3.14}$$

The left hand side of this equation is known from our measurements so that we can now find β from the form of $A(\tau)$ for very large τ. Then we define σ_t = total rms seeing due to the atmosphere and the gantry together so that

$$\sigma_t^2 = \sigma_a^2 + \sigma_g^2$$

and find from Equations (3.10) and (3.11) that

$$\left.\begin{aligned} \sigma_a &= \sigma_t (1-\beta)^{1/2} \\ \text{and} \\ \sigma_g &= \sigma_t \beta^{1/2} \end{aligned}\right\} \tag{3.15}$$

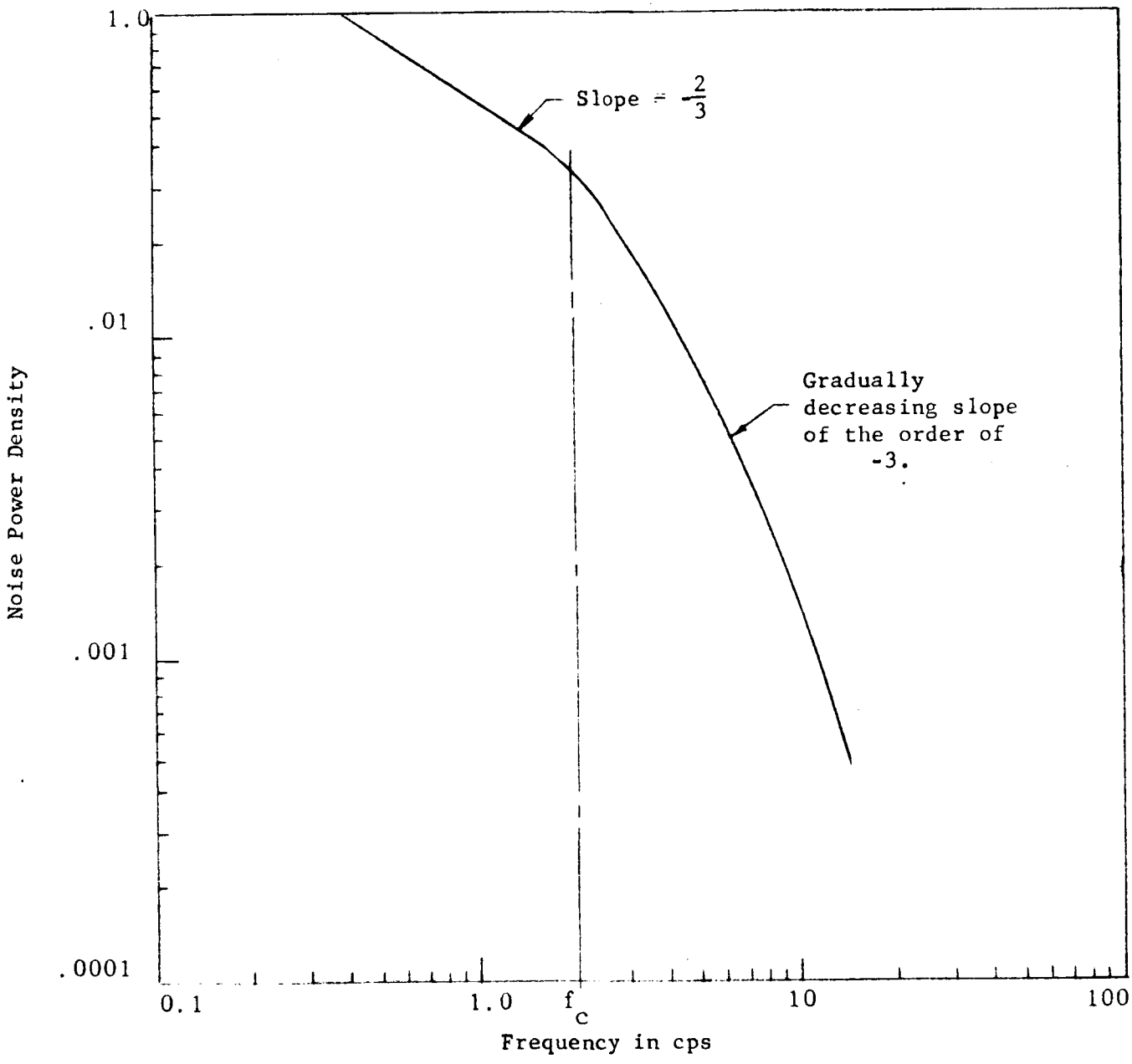

Figure 3.6
Theoretical Shape of Power Density Spectrum

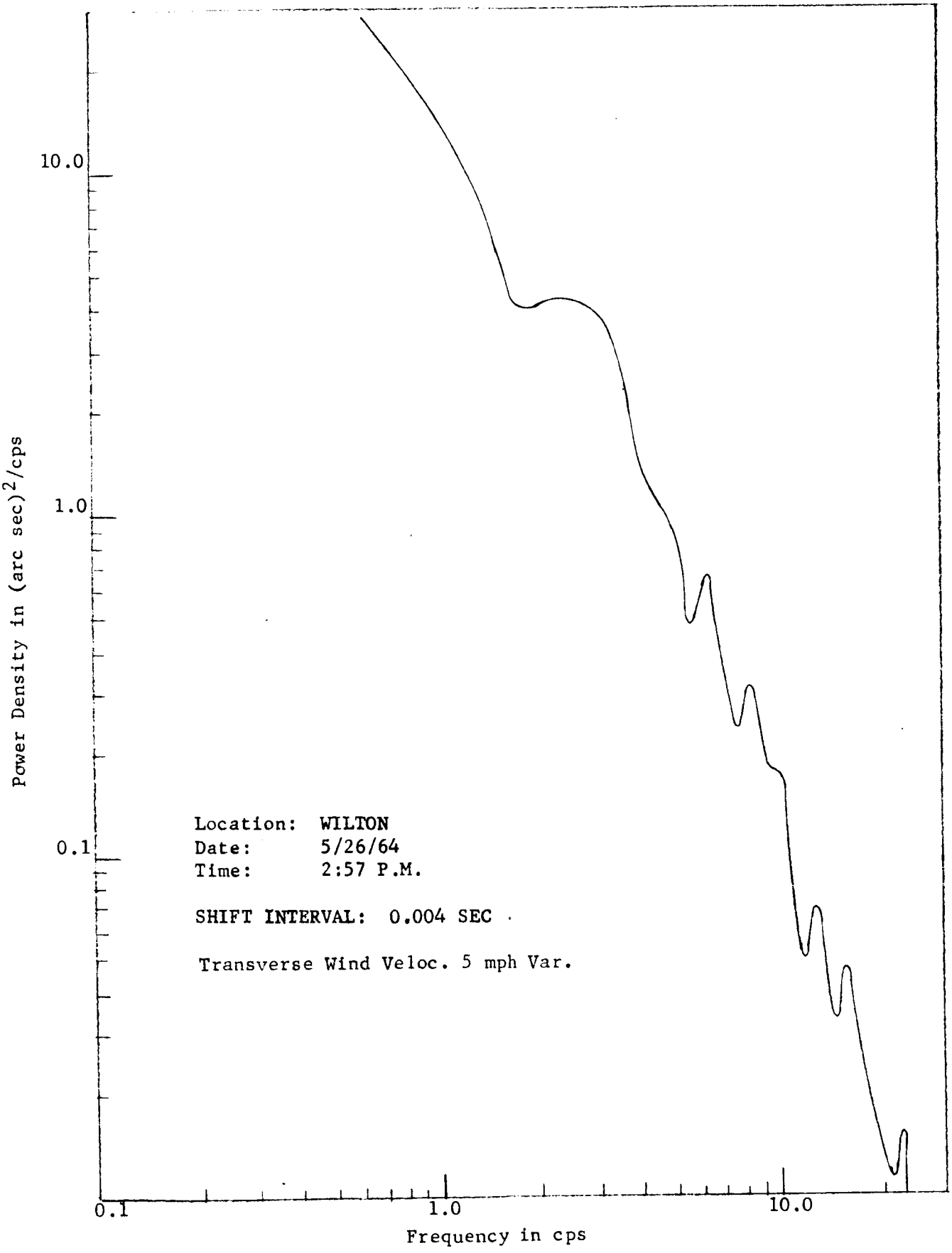

Figure 3.7 Power Spectrum of Data Taken at Wilton

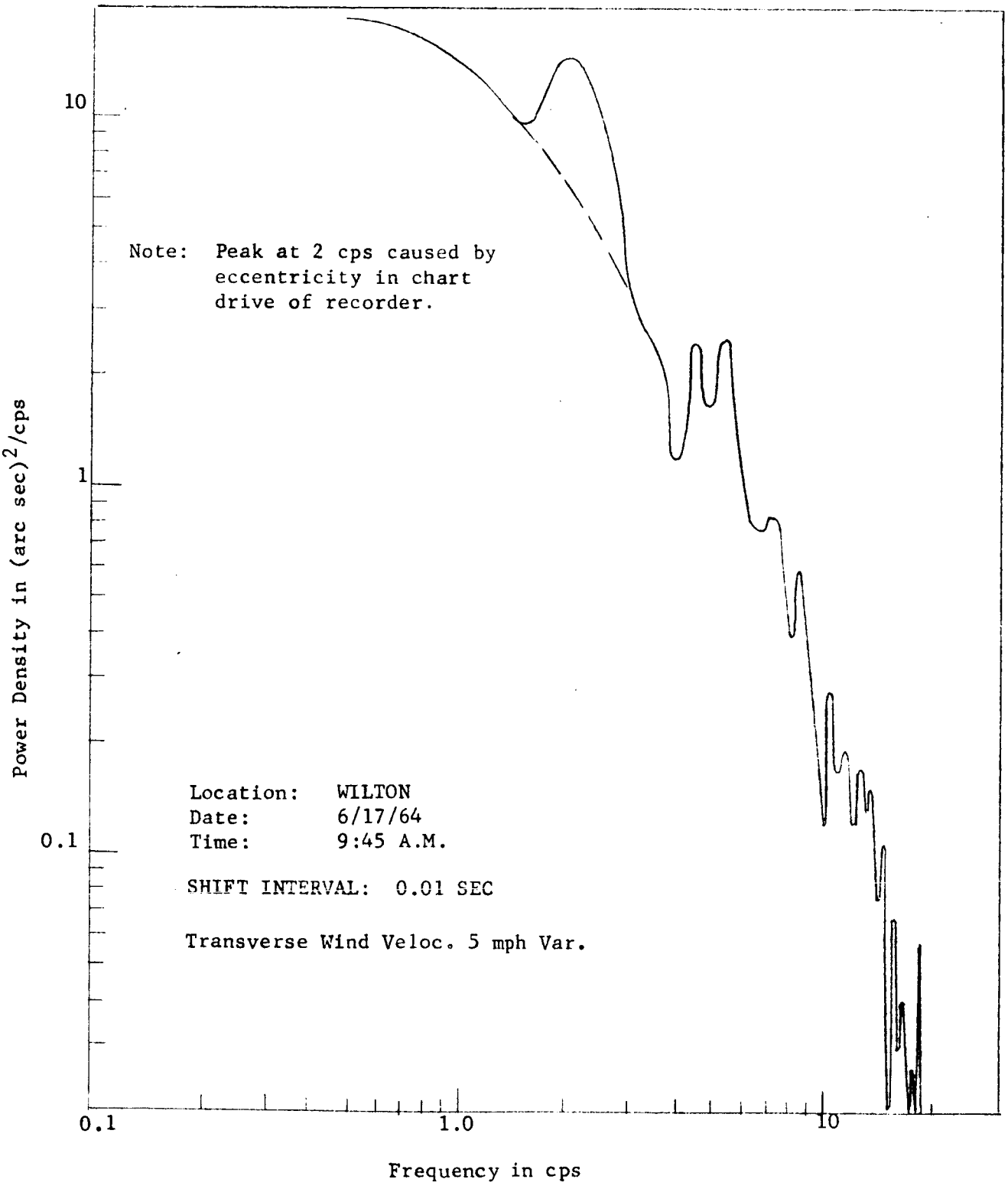

Figure 3.8 Power Density Spectrum of Wilton Data

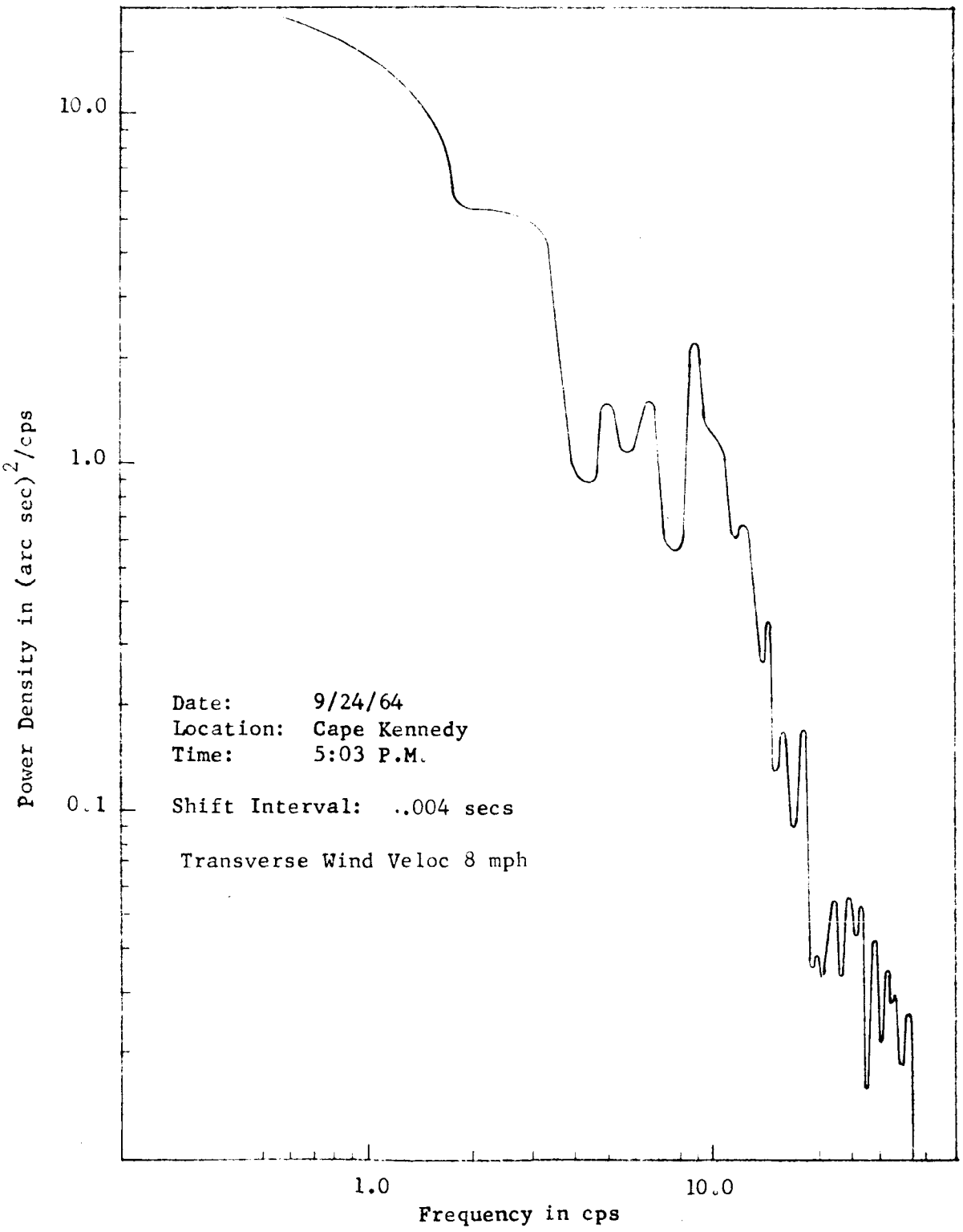

Figure 3.9
Power Density Spectrum of Data taken at Cape Kennedy

If we examine the plots of $A(\tau)$, for large τ, we find that the observed form only approximates the form predicted in Equation (3.14). This occurs because of the assumption that B is constant in Equation (3.6), while in reality it varies appreciably with time.

3.4 CALCULATION OF THE POWER SPECTRUM

The Wiener spectrum can now be found by taking the Fourier Transform of $A(\tau)$.

$$\phi(\omega) = 2 \int_0^\infty A(\tau) \cos\omega\tau \, d\tau$$

or in terms of the normalized time lag

$$\phi(\omega) = \frac{2D}{V} \int_0^\infty A(u) \cos\left(\frac{\omega D}{V}\right) du \qquad (3.16)$$

Evaluation of $\phi(\omega)$ yields*

$$\phi(\omega) = \frac{D\,A(o)}{V} \left\{ 0.75 \left(\frac{\omega D}{V}\right)^{-2/3} + \int_0^1 \left[(1+u)^{5/3} + (1-u)^{5/3} - 2u^{5/3} - \frac{10}{9} u^{-1/3} \right] \cos\frac{\omega D u}{V} \, du \right\}$$

For low frequencies, the first term is dominant, and the Weiner spectrum varies as the -2/3 power of the frequency. For larger values of the frequency the spectrum falls off more rapidly with increasing frequency, approaching an ω^{-3} dependency.

Figure 3.6 shows the predicted form of the power spectrum, and Figures 3.7, 3.8, and 3.9 show power spectra computed from data taken at Cape Kennedy

*See "Interim Technical Report" - Perkin-Elmer Engineering Report No. 7756.

Florida and at the Perkin-Elmer Seeing Range Facility at Wilton, Connecticut. Comparison of the three plots demonstrates the similarity of the shape of the power spectrum obtained from data taken under quite different meteorological and geometrical conditions.

The power density spectrum shown in Figure 6.7a, which was calculated for the frequency region below 5 cps, was calculated to verify the $f^{-2/3}$ dependence at low frequencies. The curve shown clearly follows very closely the $f^{-2/3}$ dependence.

3.5 IMAGE SHIFT AND IMAGE BLUR

The transition between the two slopes of the power spectrum occurs in the region $u = 1$, or $2\pi f = V/D$.

The dependence of the duration of the wavefront disturbance on the transverse wind velocity is given by

$$\tau \simeq \frac{L}{V} \qquad (3.17)$$

where

V = transverse wind velocity

L = size of a turbulent eddy of air (turbulon) being swept across the beam

τ = duration of the wavefront disturbance due to the turbulon.

In such a turbulent eddy, as shown in Figure 3.10a, the temperature and pressure of the air is different than that of the ambient atmosphere, causing the refractive index to vary as shown.

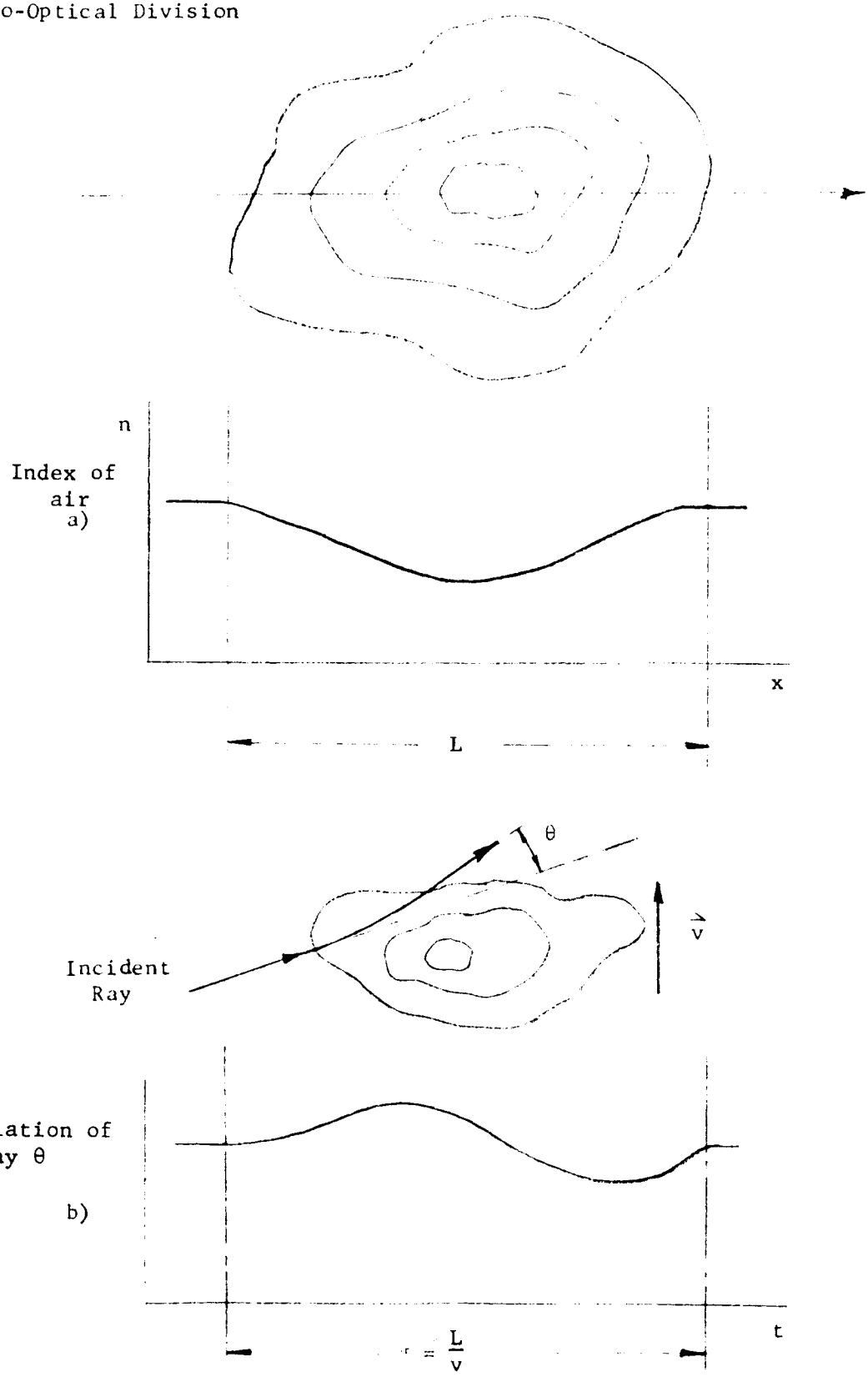

Figure 3.10
Typical Atmospheric Turbulon

The deviation of a ray caused by the turbulon shown sweeping across the line of sight is shown in Figure 3.10b.

If we let L = D, we then find the duration of the disturbance due to a turbulon whose physical size is approximately equal to that of the limiting aperture of a theodolite system, i.e.,

$$\tau \cong D/V$$

Now recall that we defined

$$u = V\tau/D,$$

where u is the normalized time lag of the autocorrelation performed in Equation 3.16. When u = 1, we are in the region where the shape of the power spectrum changes from a -2/3 power dependency to a -3 power dependency, and we find that

$$\tau = D/V \qquad (3.18)$$

Two conclusions can be drawn from this result. One, from Figure 3.6, we see that most of the energy of atmosphere turbulence is contained in the region where the $f^{-2/3}$ dependence predominates, i.e., for

$$u < 1, \tau < D/V \text{ and } L > D$$

From this it can be seen that the turbulons contributing noise energy in the region u < 1, of the power spectrum are larger than the limiting aperture of the theodolite system. If we now look at the physical case of a

turbulon whose dimensions are larger than the system aperture, we find that the fraction of the cross-section of the turbulon sampled (traversed) by the beam becomes a smaller fraction of the entire turbulon as its size increases, and the variations of index across the turbulon sample become small. But the variations of index relative to the ambient air remain large, with the result that the entire wavefront is tilted, while remaining approximately planar. When the tilted wavefront reaches the theodolite, it forms an image that is not deformed, but is displaced in the focal plane. This is the phenomenon of image shift.

If we similarly consider the region of the power spectrum where $u > 1$, we find that $L < D$.

Thus the main contribution of energy in the region of the power spectrum $u > 1$ comes from the motion of turbulons whose size is smaller than the aperture of the system. In this case, the variation of index across the sample of the turbulon penetrated by the beam (in this case equal to the whole turbulon) is quite high, causing a deformation of the wavefront. Since there is no component of the variation of index across the turbulon which remains constant, there is no image shift. Thus the only effect from turbulons for which $L < D$ is the phenomenon of image blur.

3.6 LOW AND HIGH FREQUENCY CUTOFFS

Since the predicted form of the power spectrum depends in part upon the size, or scale, of the turbulons, we would expect that the power spectrum will cut off both at some maximum frequency, corresponding to the transverse wind velocity and the size of the smallest turbulons present in

the atmosphere, and at some minimum frequency corresponding to the transverse wind velocity and the size of the largest turbulons.

An approximate value of the expected cutoff of the power spectrum at maximum frequency is given by

$$f = 1/$$

where $, = \ell_o/v$

and ℓ_o = inner scale factor

The inner scale factor is a measure of the size of the smallest turbulons. At ground level, $\ell_o \cdot 0.3$ cm, for a transverse wind velocity of 10 mph (or 500 cm/sec), the cut-off frequency is

$$f \quad \frac{v}{\ell} = 265 \text{ cps.}$$

Fried and Cloud* find that the outer scale length is given by

$$L_o = (bh)^{1/2}$$

where

$$b = 4 \text{ meters}$$

For an altitude of 2 meters we find that

$$= \frac{L_o}{v} = \frac{8}{5} = 0.56 \text{ second}$$

and f cps.

*"The Phase Structure Function for an Atmospherically Distorted Wave Front", D.L. Fried and J.D. Cloud, Technical Memorandum No. 192, North American Aviation Inc.

The fact that the power spectrum extends to frequencies more than two orders of magnitude below the predicted low frequency cutoff indicates that the statistical nature of the atmosphere is not stationary and isotropic. Long term fluctuations (on the order of several seconds and more) of the meteorological parameters measured, (wind velocity, wind direction and temperature), also indicates this non-stationarity of the atmosphere. It probably results from the surrounding terrain, which includes a row of hills 1/4 mile to the west, a stand of shrubs and small trees 100 feet away and paralleling about 1/3 of the path, several 2 story buildings within a radius of 1/4 mile and from the characteristic turbulence of weather near the shoreline.

SECTION IV

MODULATION TRANSFER FUNCTION OF THE ATMOSPHERE

4.1 INTRODUCTION

Of the many methods that have been developed for the appraisal of the performance of optical systems, that which appears to offer the best combination of theory and easily interpreted physical measurements is the application of the theory of the modulation transfer function. This transfer function is a mathematical description of the properties of a system which alters the information being carried through the system.

The assumption that the modification of the information being conveyed through the system is related to a describable property of the system itself, and not to any property of the information, is what makes system appraisal by modulation transfer function so universal. Once the transfer function is known, the relation between input information and output information can be easily found regardless of the nature of the information itself.

A second useful property of the modulation transfer function is the ease with which the joint effect of several system elements can be found by simply "cascading", or multiplying the transfer functions of each element to obtain an overall system transfer function.*

---

*This is not always true. For example, the transfer function of a single lens composed of several elements is quite different from the transfer function obtained by cascading the separate transfer functions of the separate elements. However, for the discussion here, this statement is valid.

It is this characteristic which allows us to calculate the overall system performance of a theodolite immersed in a turbulent atmosphere by considering the theodolite itself and the atmosphere as separate system elements.

The modulation transfer function, often called the sine wave response, of an image forming optical system can be written as

$$M(k) = \frac{I_{max} - I_{min}}{I_{max} + I_{min}} \tag{4.1}$$

where M(k) is the modulation of the image of a sinusoidal target of wavelength 1/k at the image plane, and

I_{max} = maximum intensity of image

I_{min} = minimum intensity of image.

Any object can be broken down into its spatial frequency components by taking the two dimensional fourier transform of the object's distribution of intensity, $U_o(x,y)$.

$$U_{OT}(k_x, k_y) = F[\, U_o(x,y) \,] \tag{4.2}$$

where $U_{OT}(k_x,k_y)$ gives the distribution of the spatial frequency components of the object.

When the information contained in the object is passed through a system element the information is modified by the physical characteristics of that element. This modification is described by the modulation transfer function, and results in a two dimensional output distribution of spatial frequency components given by

$$U_{IT}(k_x, k_y) = M(k_x, k_y)\, U_{OT}(k_x, k_y) \tag{4.3}$$

If the system element described in 4.3 by $M(k_x, k_y)$ is an image forming element, then $U_{IT}(k_x, k_y)$ describes the spatial frequency distribution of the object due to the image forming element. Rewriting 4.3 we obtain

$$M(k_x, k_y) = \frac{I(k_x, k_y)}{U_{OT}(k_x, k_y)} \tag{4.4}$$

which is equivalent to 4.1 for the case of a sinusoidal target.

For the case of information passing through n system elements, we may write

$$U_{IT}(k_x,k_y) = M_1(k_x,k_y)\, M_2(k_x,k_y) \ldots M_n(k_x,k_y)\, U_o(k_x,k_y) \tag{4.5}$$

Then the inverse fourier transform of $U_{IT}(k_x,k_y)$ will give us the image

$$U_I(d,y) = F^{-1}[U_{IT}(k_x, k_y)] \tag{4.6}$$

of the object $U_o(x,y)$ formed by the system of n elements.

For the practical case of a theodolite operating in a turbulent atmosphere, there are two system elements to consider; the atmosphere and the image forming optics of the theodolite. We will consider the latter element first.

4.2 TRANSFER FUNCTION OF OPTICS

The modulation transfer function (sometimes called the optical transfer function or frequency response function) of an aberration-free image forming system with incoherent illumination is given by*

*Born & Wolfe, "Principle of Optics", Macmillan, 1959, page 484.

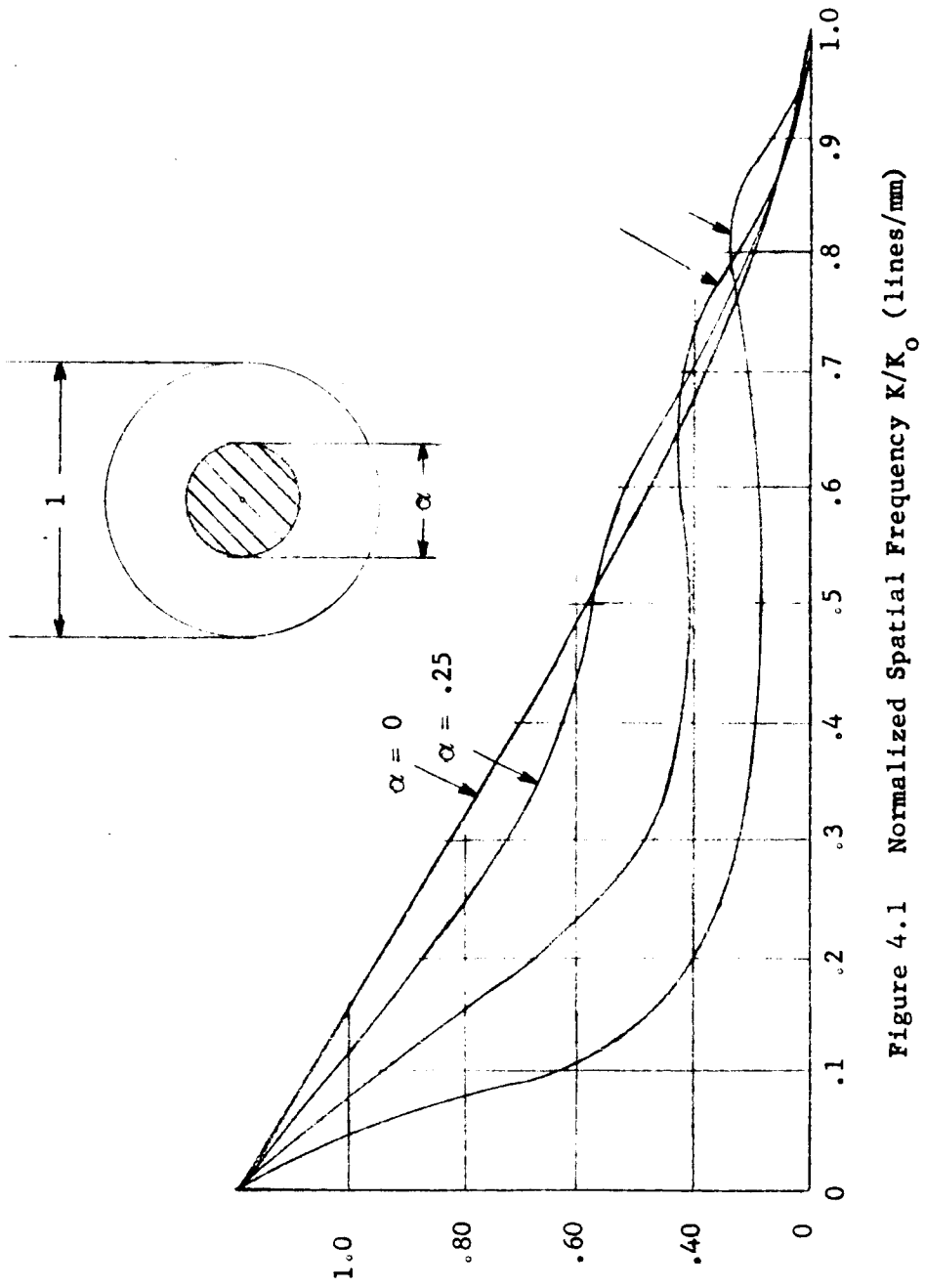
1
α
α = 0
α = .25
0
.1
.2
.3
.4
.5
.6
.7
.8
.9
1.0
Normalized Spatial Frequency K/K$_o$ (lines/mm)
1.0
.80
.60
.40
0
Modulation Transfer Function

Figure 4.1

$$M\left(\frac{x}{\lambda R}, \frac{y}{\lambda R}\right) = \frac{1}{(\lambda R)^2}\int_{-\infty}^{\infty}\int_{-\infty}^{\infty} G(x'+x,y'+y)\, G^*(x,y)\, d_x', d_y' \quad (4.7)$$

where $x/\lambda R = k_x$, $y/\lambda R = k_y$ (4.8)

and G = Pupil function of image forming system

R = focal length of image forming system

λ = wavelength of light

The pupil function G(x', y') gives the relative phase at any point (x',y') of the exit pupil of the image forming system. The assumption of an aberration-free system implies

$$G(x',y') = 1,$$

and 4.7 becomes the auto-correlation function of the aperture of the image forming system. Figure 4.1 shows the transfer function for image forming system apertures with varying amounts of central obscuration.*

From the definition of the autocorrelation function, we see that the modulation transfer function shown in Figure 4.1 is equal to

$$M(k) = M\left(\frac{x}{\lambda R}, 0\right) = \frac{A_s}{A} \quad (4.9)$$

The abscissa of the plot of M(k) in Figure 4.1 is in units of ak;

$$ak = k/k_o \quad (4.10)$$

where k_o is the spatial frequency at which $M(k_o) = 0$. Thus, from 4.9,

$$k_o = D/\lambda R \quad (4.11)$$

* "Optical Design and Modulation Transfer Functions", Abe Offner

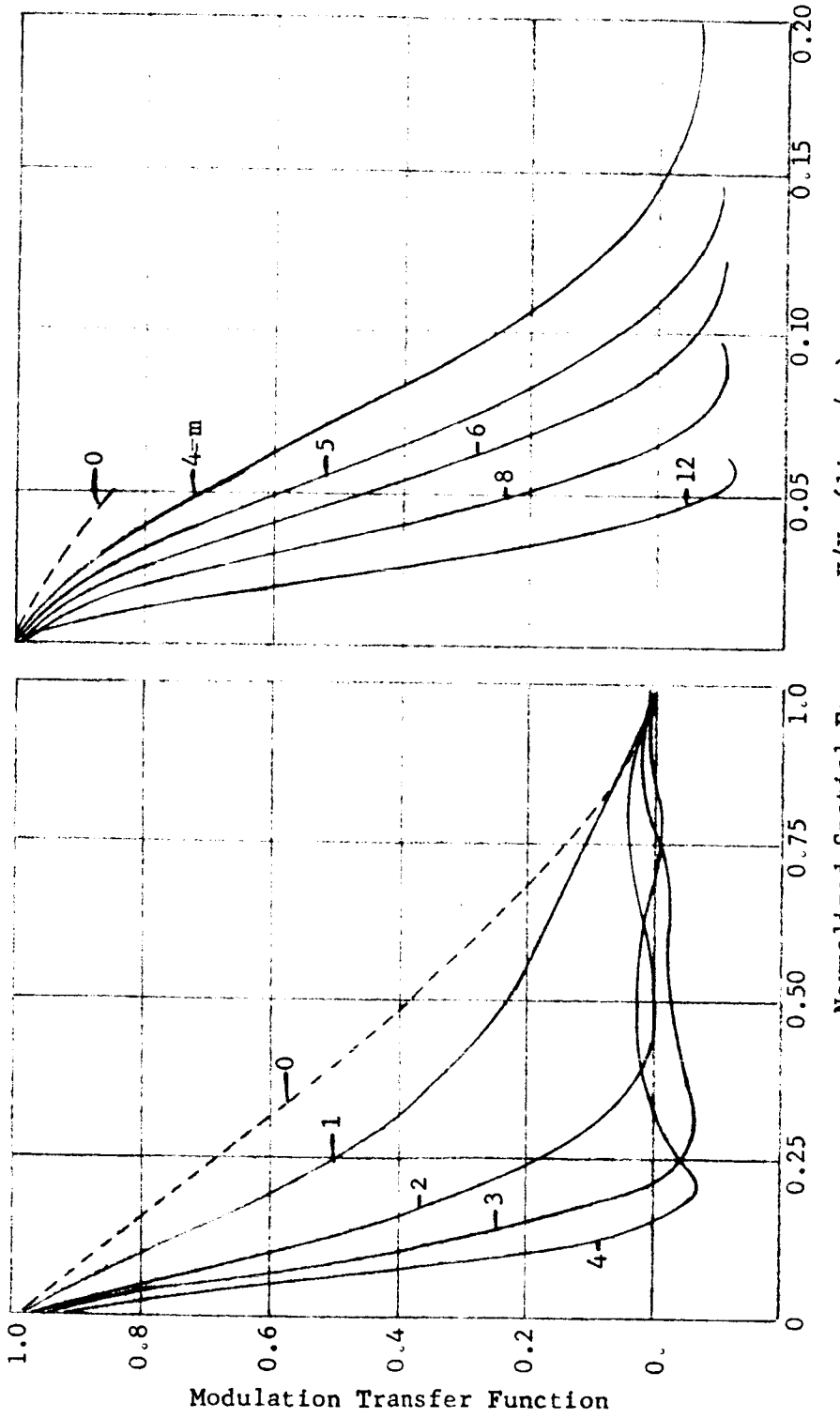

Figure 4.2 Modulation Transfer function for an Optical System Suffering from a Defect in Focus given by $Z = m \frac{2}{\pi} (f/\#)^2 \lambda$

Recalling that the f-number of an optical system may be defined as

$$f/No. = R/D \tag{4.12}$$

equation 4.11 becomes

$$k_o = 1/\lambda(f/No.) \tag{4.13}$$

Thus the resolution of an aberration-free system, expressed in cycles per unit length, is a function of the f-number of the system.

If we divide both sides of equation 4.11 by R, we can find the system angular resolution, given by

$$\beta = k_o/R = D/\lambda \tag{4.14}$$

Thus, from Equation 4.14 we see that the ability of a system to resolve objects of small angular extent is a function only of the diameter of the system aperture, and not a function of the focal length.

The effect of aberrations on an image forming system, for both aberrations intrinsic in the structure of the lens and aberrations arising from a defect in the focus, are rather strong. As an example, Figure 4.2 compares the transfer function for a system suffering from defect of focus with the transfer function of an aberration-free system.*

The importance of the focal length in an image forming system enters when one considers the mode of information recovery. If film is used, consideration must be made of the transfer function of the film used to assure that the film spatial frequency cut-off is higher than that of the image forming system.

---

* Born and Wolfe, "Principles of Optics", 2nd edition, pg. 486

In the practical case of the theodolite, as we shall see below, the high frequency cut-off of the optics is much greater than the high frequency cut-off resulting from atmospheric turbulence.

4.3 MODULATION TRANSFER FUNCTION OF THE ATMOSPHERE

The alteration, or modification, of information being transmitted through the atmosphere in the form of wavefronts occurs when the inhomogenities of the turbulence caused wavefront deformations. The mathematical description of the effect of these wavefront deformations, the modulation transfer function, is given in terms of a statistical quantity describing the turbulence, known as the phase structure function $D_s(P)$. This phase structure function describes the magnitude of the square of the difference of the wavefront deviations between two points as a function of the distance, P, between the two points.

The modulation transfer function of the atmosphere is given, in terms of this phase structure function,* as

$$M_a(k) = e^{-1/2\, D_s(\lambda R k)} \tag{4.15}$$

where λ = wavelength of light

R = radius of reference spherical surface with respect to which the wavefront deviations are measured

k = spatial frequency

---

*D. L. Fried and J. D. Cloud, "The Phase Structure Function for an Atmospherically Distorted Wavefront," T.M. No. 192, Space and Information Systems Division, North American Aviation, Inc.

The phase structure function can be expressed in terms of the auto-correlation function of the wavefront deformation given by

$$C(x', y') = < \Delta (x,y) \Delta (x + x', y + y') > \qquad (4.16)$$

where $< >$ indicates an average value

and $\Delta (x,y)$ is the wavefront deformation.

Equation 4.15 then becomes

$$M_a (k) = e^{-\frac{4\pi^2}{\lambda^2} [C(o,o) - C(\lambda R k_x, \lambda R k_y)]} \qquad (4.17)$$

The random fluctuations in the index of the atmosphere that cause the wavefront deformations exhibits what is called a Kolmogoroff spectrum. This means that $C(x', y')$ is of the form

$$C(x', y') = C(o,o) - \alpha (x'^2 + y'^2)^{5/6} \qquad (4.18)$$

where α is a function of the light path geometry and local meteorological conditions.

Thus equation 4.17 becomes

$$M_a(k) = e^{-\frac{4\pi^2}{\lambda^2} \sigma (k_x^2 + k_y^2)^{5/6}} \qquad (4.19)$$

where σ is a seeing strength factor, equal to the rms angular motion of the center of gravity of a point image measured in radians*.

---

* Hufnagel & Stanley, "Modulation Transfer Function Associated with Image Transmission thru Turbulent Media" JOSA, Vol. 54, No. 1, Jan. 1964

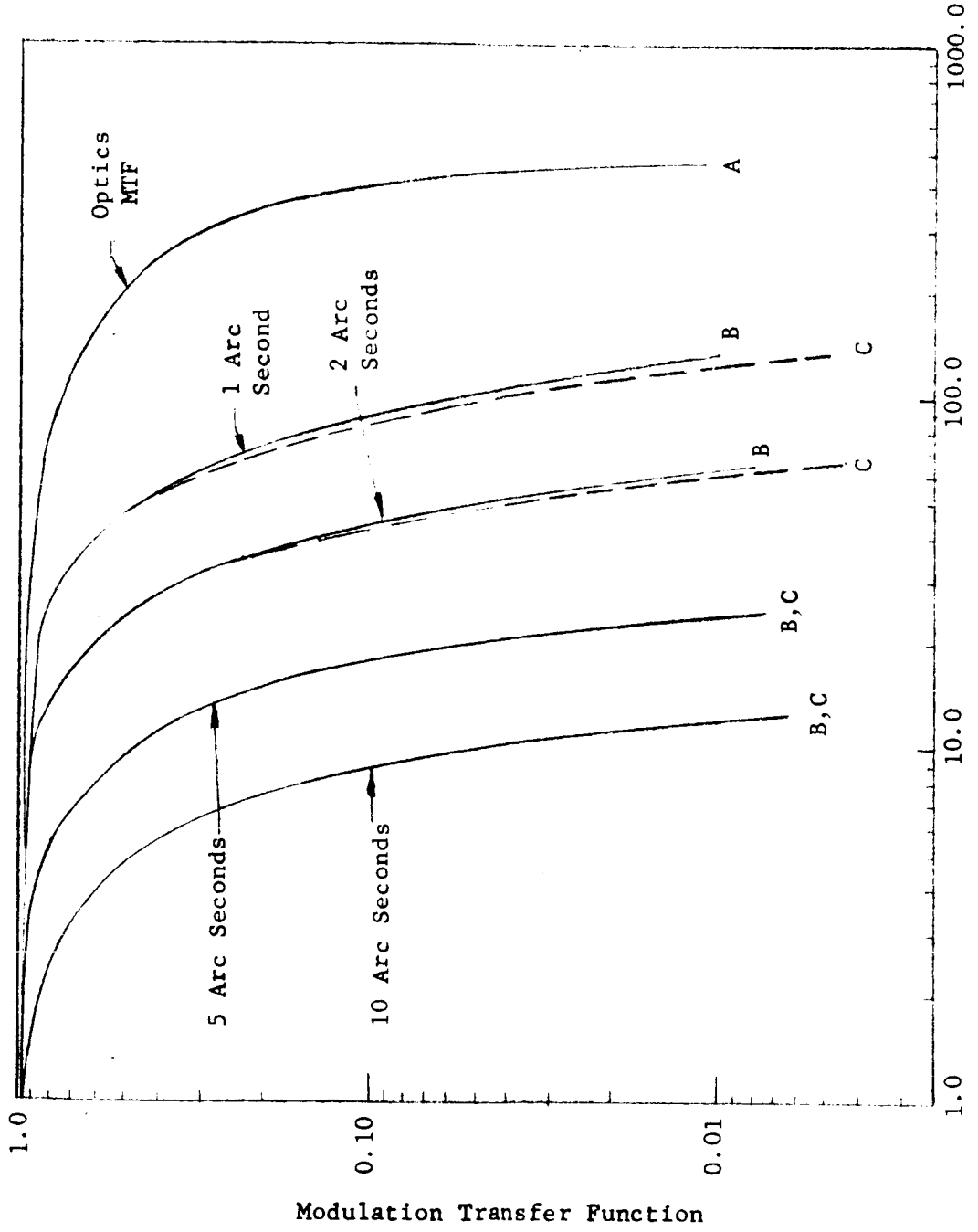

Figure 4.3 Modulation Transfer Function of LR2A/GS Theodolite With Various Atmospheric Seeing Conditions

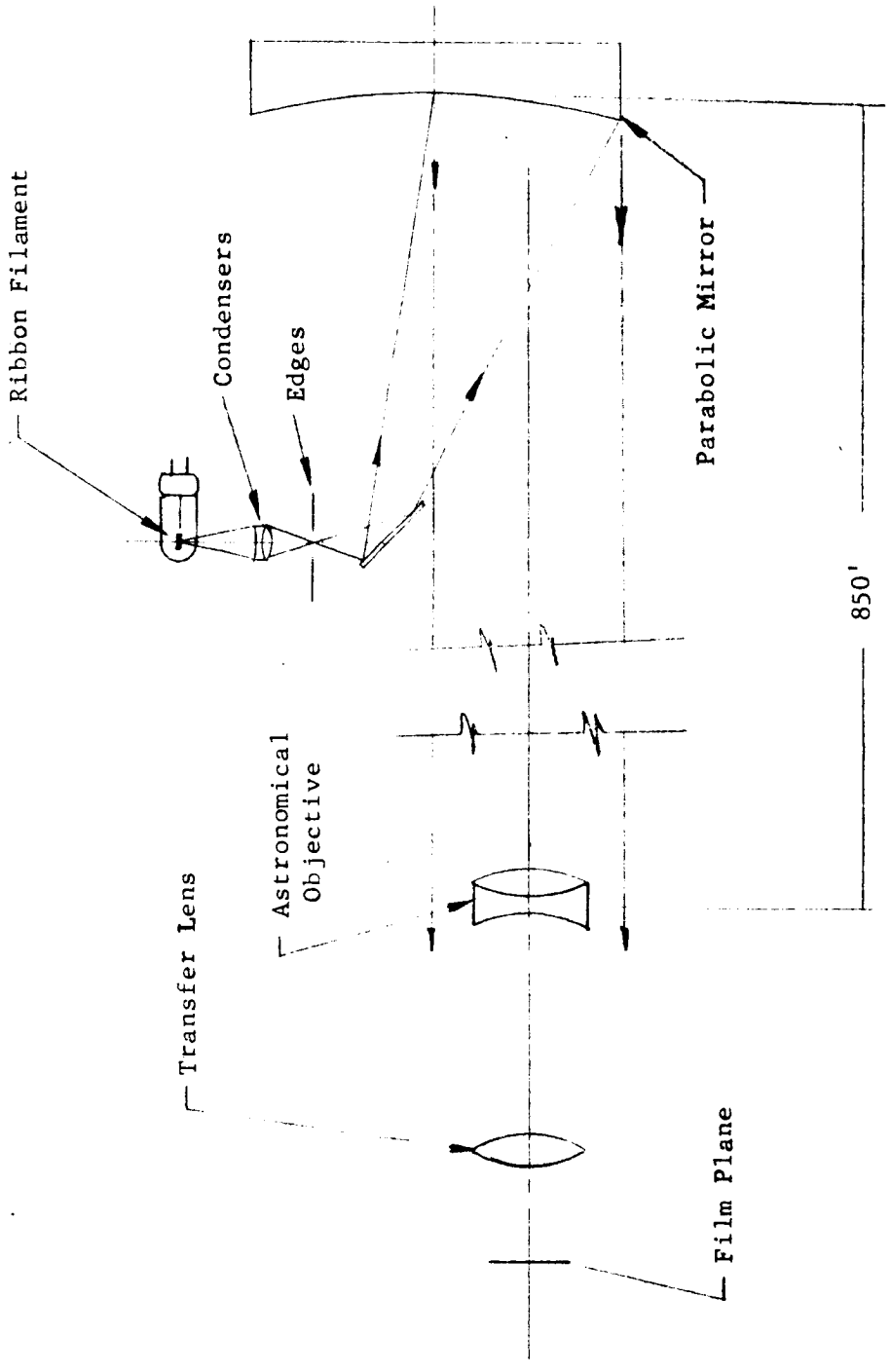

Figure 4.4 Arrangement of Equipment for Measuring Modulation Transfer Functions

The atmospheric transfer function given in Equation 4.20 and the optical transfer function given in Section 4.2, for the specific case of an f/3.5 theodolite (30" focal length) operating under atmospheric conditions typical of Cape Kennedy, is shown in Figure 4.3. The family of curves labeled C represent the total system transfer function and are the product of curve A and the family of atmospheric transfer functions labeled B.

The obvious dominance of the degrading effect of the turbulent atmosphere is clearly demonstrated in Figure 4.3. The optical transfer function is so much higher that the overall system transfer function is effectively determined by the atmosphere alone. This relationship may permit the designer of a theodolite to relax the design of the optics (and thereby reduce its cost) to the point where the transfer function begins to appreciably effect the system transform.

4.4 EXPERIMENTAL DETERMINATION OF MODULATION TRANSFER FUNCTION OF ATMOSPHERE

In order to determine experimentally the modulation transfer function of the atmosphere, the following experiment was performed, as shown in Figure 4.4. A tungsten ribbon filament was imaged on to a square, formed by four sharp edges, placed at the focal plane of a 90" focal length, f/7.5 parabola. Half the parabola was used as an off axis parabola to eliminate any central obscuration that would have changed the shape of the optical modulation transfer function. The collimated beam formed by the illuminated square was then sent through 850 feet of turbulent atmosphere (along a path parallel to the beam from the LR2A theodolite), where a lens assembly collected part of the beam and formed an image on the film plane of a 35 mm camera body.

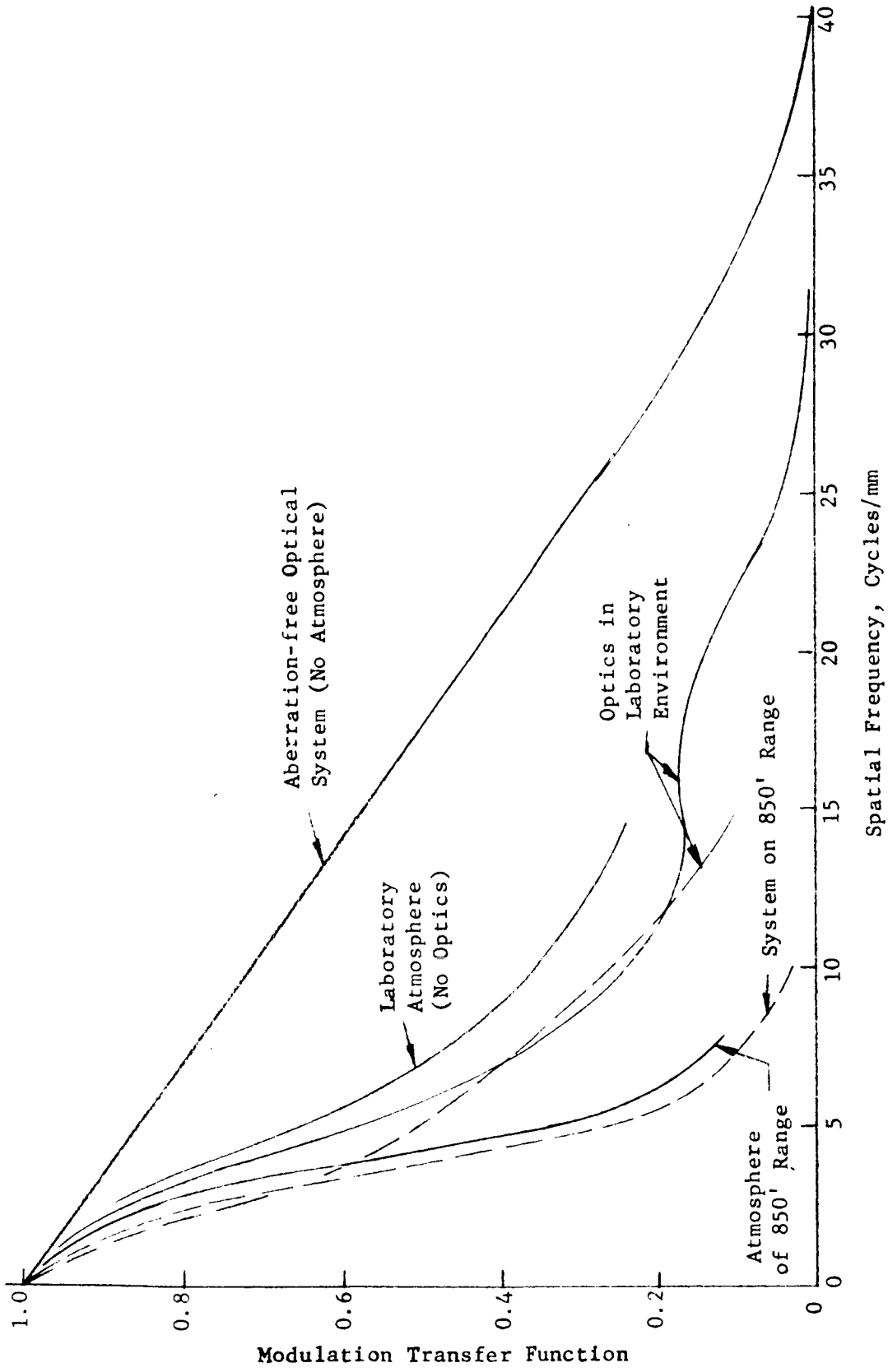

Figure 4.5 Modulation Transfer Functions of Various Systems

To obtain the atmosphere transfer function from the image of the square formed on the film, the image is scanned with a microdensitometer and a plot of film density vs. displacement is obtained. By calculation, (see Appendix C) the non-linearity of the film is removed, and a plot of intensity vs. displacement is obtained. The fourier transform of this plot can be computed to obtain the spatial frequency distributions of the image. This transform is often called the square wave response of the atmosphere-camera-film-microdensitometer combination.

A method for computing the sine-wave response, or modulation transfer function, from the square-wave response has been developed (see Appendix C) by Perkin-Elmer, and permits computation of the transfer function of the atmosphere-camera-film-microdensitometer combination. Use of equation 4.5 then permits us to obtain the transfer function of the atmosphere by dividing out the presumably known transfer functions of the three other elements. With the focal length of the camera chosen as 2900 mm, the transfer function of the microdensitometer is essentially unity throughout the frequency region of interest. In addition, the long focal length combined with the use of high resolution aerial photography film led to a transfer function of the film essentially unity throughout the frequency region of interest.

Figure 4.5 illustrates the transfer function of the camera used, assuming no aberrations. In addition, several experimental curves obtained with the method described above are shown.

The edge photographs taken in a lab environment correspond to atmospheric seeing of 1.1 arc second, while the edge photograph taken on the seeing range corresponds to atmospheric seeing of 3.0 arc seconds.

SECTION V

THE EFFECT OF TIME INTEGRATION UPON THEODOLITE ANGULAR ERRORS CAUSED BY ATMOSPHERIC SEEING DISTURBANCES

5.1 THEORETICAL DISCUSSION

5.1.1 Introduction

For the treatment of the problem in hand we will consider the theodolite station to be located at or near the ground surface at a range of 850 feet from the roof prism carried on the missile's gyro gimbal structure. The line of sight is upward at an elevation angle of 25°. The theodolite measures the gyro azimuth angle and provides an error signal for correcting this to a fixed reference value. The present major limitation upon the accuracy with which this correction can be made arises from the variations in the index of refraction of the air in the line of sight. The object of this memorandum is to get an approximate value for the rms angular error which will be caused by the atmospheric "seeing" irregularities and to indicate possible means of reducing this error particularly by the use of time integration.

The anticipated angular motion of the beam is of the order of a few seconds of arc, consequently it will be adequate for our treatment to neglect any beam translation effects and merely to calculate the optical wavefront deflections which result from the random fluctuations in air density and index of refraction. As we understand, the maximum present gyro system frequency response is one cycle per second, so that it is necessary to consider

only those effects which occur in times of the order of seconds. Since a two knot wind component will translate the atmospheric inhomogeneity pattern a distance of 3 1/3 feet in one second, we are concerned with atmospheric irregularities occurring in a distance scale of a few feet.

The analytical approach which we will use will be to determine the fluctuation in the angle of arrival (at the theodolite station receiver) of a beam which has been generated by radiance at a single point in the theodolite source plane. Then we will observe the averaging effects which result from integrating over the whole source plane and also from integrating over the volume of space through which the theodolite looks in a typical measurement interval. This volume is that part of the atmosphere swept through the light transmitted to and returned by the reflecting optic (the roof prism) during the observation time interval and is shown in Figure 5.5. We will assume that the atmospheric density disturbances are isotropic in a small region of space and that they vary only with the elevation of the region above the ground level.

5.1.2 Geometrical Details

The optical system which we consider consists of a source-detector assembly located in the focal plane of a collimator, and a roof prism reflector located at a range R from the collimator. The assembly is shown schematically in Figure 5.1. It consists of a glass "slit prism" with two reflecting surfaces. Images of the illuminating filament are formed on these reflecting surfaces by the two spherical transfer mirrors. The images fall in the collimator focal plane and are the source of optical transmission from the theodolite.

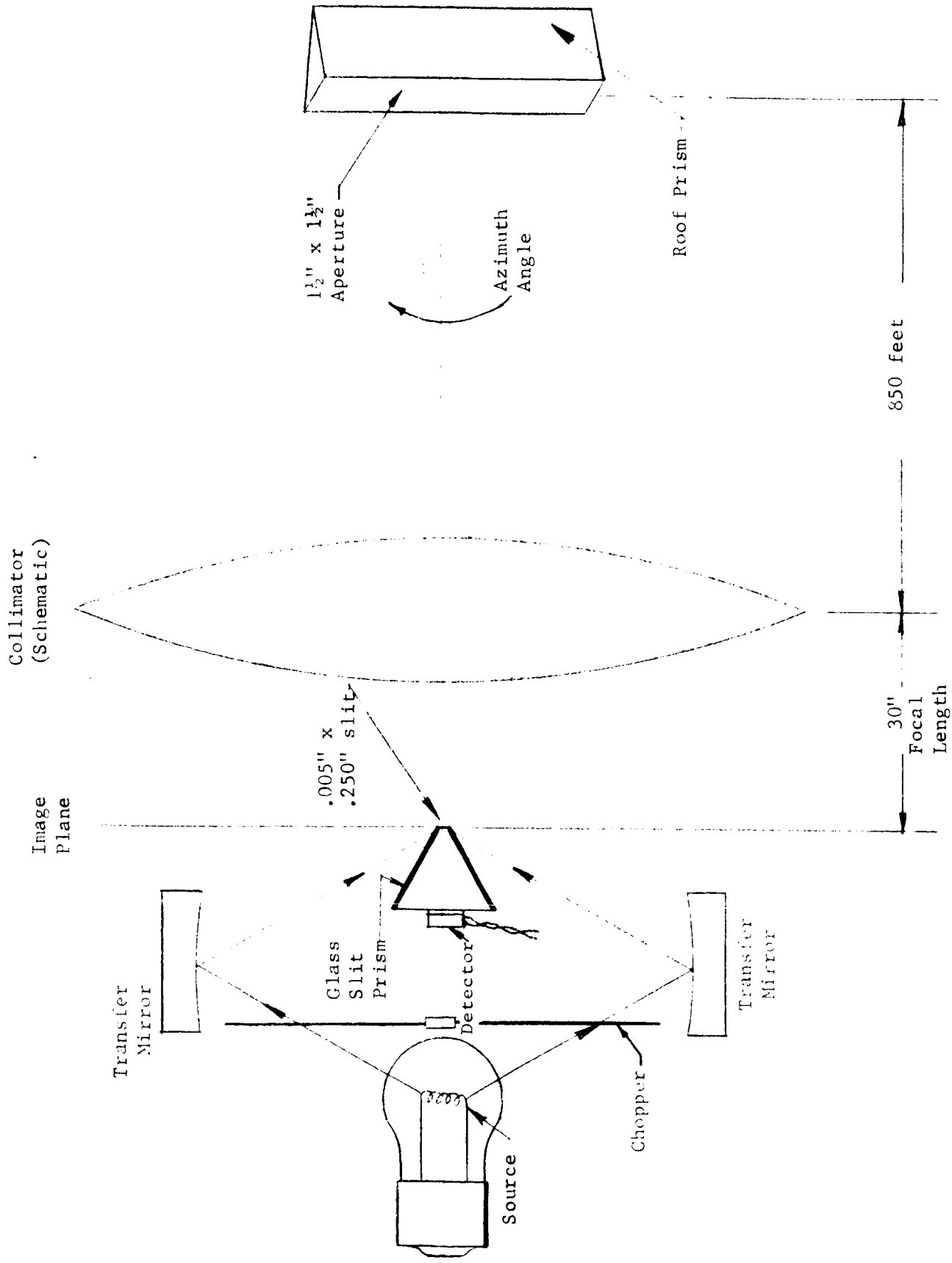

Figure 5.1 Schematic of Optical System of Theodolite

After the light from a primary image has been transmitted, reflected, and received, it forms a reversed secondary image on the opposite portion of the focal plane. A small azimuth rotation of the roof prism, or an equivalent atmospheric angular deviation due to the "seeing" effect, serves to move the secondary image from its ideal position. Since in the actual theodolite transmitter two primary images are used, one on either side of the prism slit, an angular motion of the beam or of the optical wavefront in the beam will cause one or the other of the images to spill over the edge of the slit prism and thus to pass light to the detector located behind the prism. In order to identify which image has moved over the edge, and thus to determine the direction of the angular motion, the primary images are turned on and off alternately by means of a chopper, and the time at which the spilled over light is detected is used as an indication of the direction of the image motion. The amplitude of the detector output difference signal is nearly proportional to the angular amplitude of image motion.

The balance of the optical system may be described sufficiently well by the plan and elevation views of the system shown in Figures 5.2 and 5.3. These show how rays from a point in the source plane pass to the corners of the roof prism and back to the corresponding point in the image plane. One observes that since the aperture of the roof prism is less than the aperture of the collimator, that the collimator aperture itself is not filled. Indeed, since the critical edge of the source is 0.0025 inches off axis, the minimum source field angle is this distance divided by the 30-inch focal length or 83×10^{-6} radians. Thus, the center of the return beam produced by a point on the source edge is displaced $83 \times 10^{-6} \times 850 \times 12 = 0.85$ inches from the center of

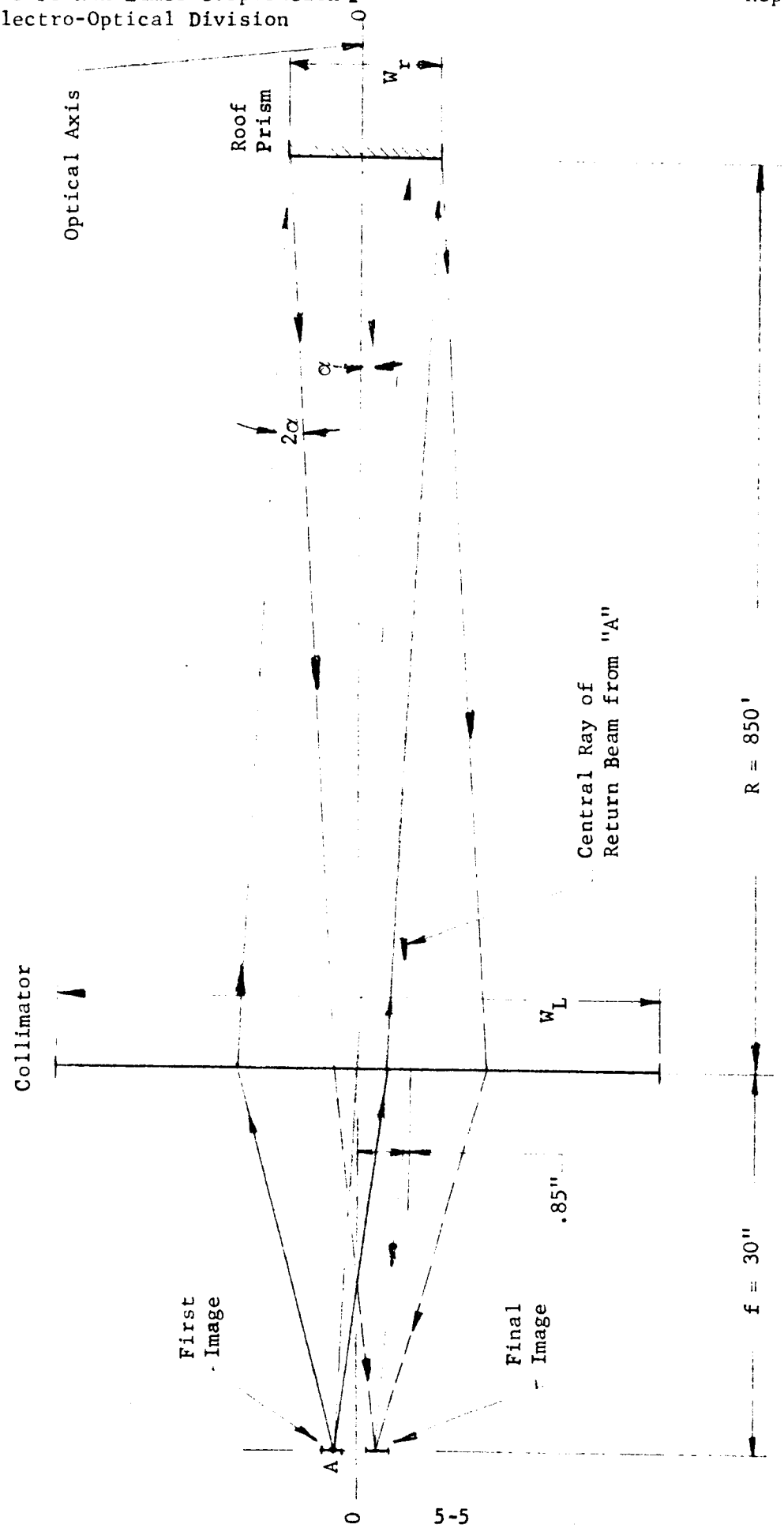

Figure 5.2 Plan View of Outgoing and Return Rays

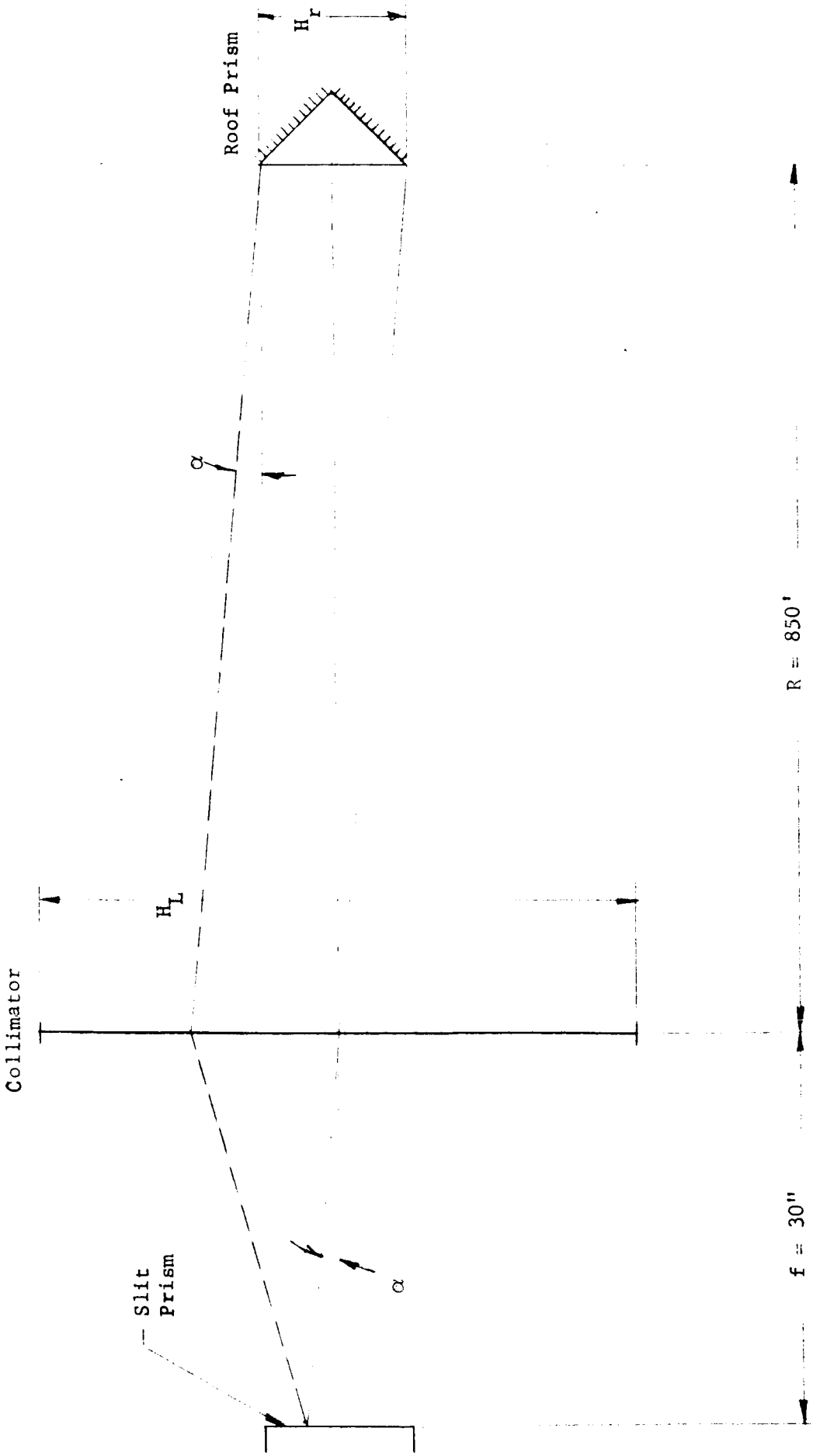

Figure 5.3 Elevation View of Outgoing and Return Rays

the collimator. Source points which are farther away from the edge produce illumination beams passing through regions farther from the center of the collimator. One observes that the collimator aperture is the field stop of the system. Figure 5.4 illustrates the illumination pattern in the collimator aperture.*

Although a resolution element in the primary image when returned, illuminates only a limited zone in the collimator aperture, we may assume that the radiances of all source resolution elements are equal and that the light received in the final image from these adds incoherently. Thus, so far as overall image position is concerned, the effects in the aperture are additive, and we may choose for the aperture dimensions, the x and y distances between the points of half illumination in a beam;** namely, x = 2.8" and y = 5" (see Figure 5.4). The center-to-center distance of the two (transmitted and received) beams then varies from 1.7 inches at the theodolite station to 0 inches at the roof prism. Since we are concerned with beam deflection measurements averaged over seconds of time and since the normal translation of the atmospheric irregularities by horizontal winds in such a period of time amounts to several feet of distance, we may neglect the fine structure of the aperture illumination and assume that we have a single beam 5 inches square at the theodolite station and 1 1/2 inches square at the roof prism station.

---

*The aperture is vignetted at top and bottom by the dimensions of the transfer mirrors.

**The half illumination points can be determined approximately from the "beam weighting function" shown in Figure 4.

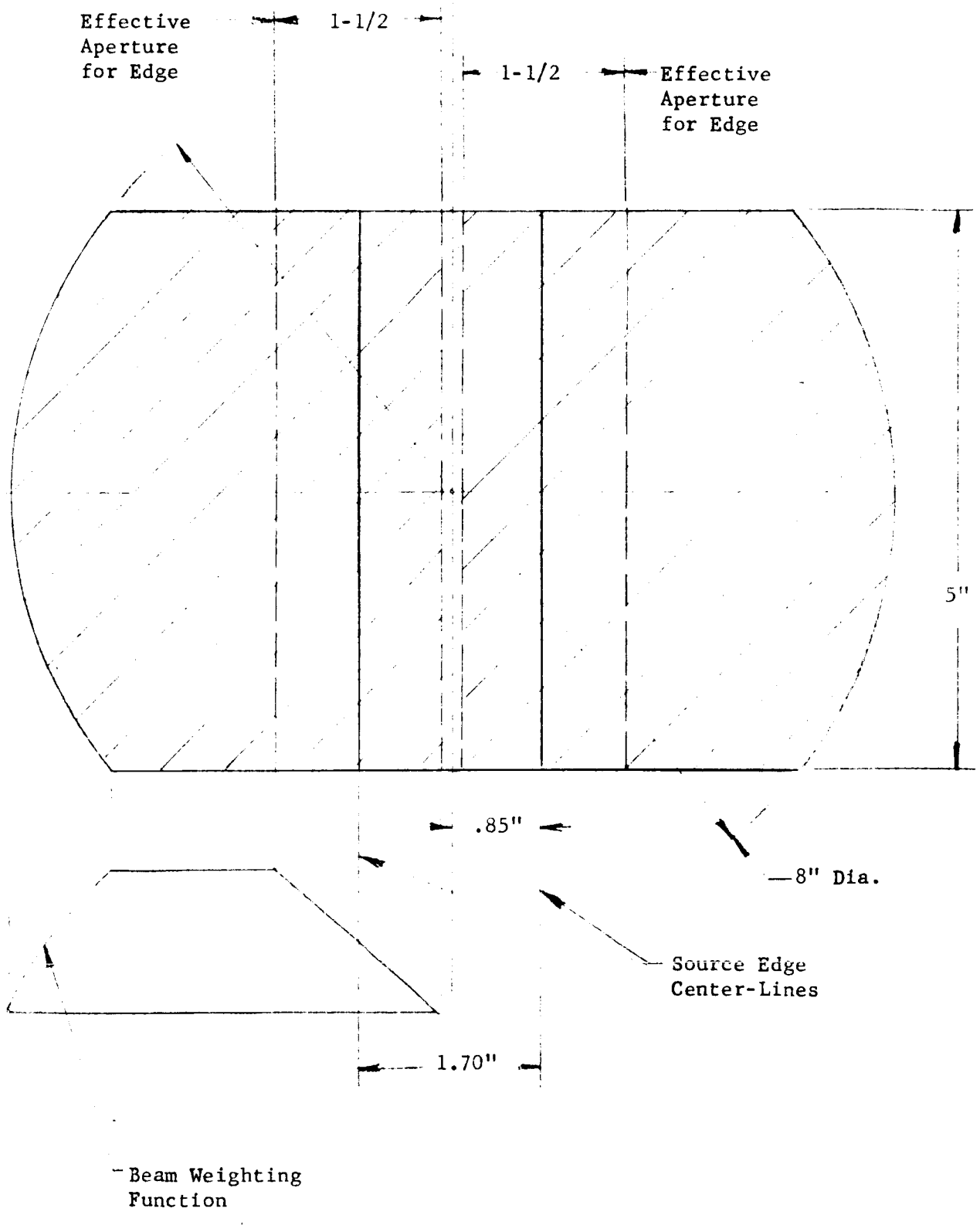

Figure 5.4 Illumination Pattern in Collimator Aperture

If the theodolite system averages angles over a time interval Δt, and if the component of the horizontal wind velocity in the direction normal to the line of sight is V, the region in space whose transmission characteristics are averaged in the time Δt, consists of a truncated pyramid 850 feet with minor thickness varying from 5 to 1 1/2 inches and with major thickness given by the product $V\Delta t$ as shown in Figure 5.5.

5.1.3 Calculation of Angular Errors Resulting from Seeing Effects

Because of its construction, the theodolite measures the displacement (in a direction normal to the primary image edge) of the center of gravity of the image received after transmission through the atmosphere. Under conditions of low atmospheric scintillation or of short path length, as is true here, the displacement of the image in the image plane (measured normal to the primary image edge) is very nearly equal to the product of the focal length by the integral over the theodolite aperture of the angular gradient of the wavefront determined in the direction normal to the primary image edge. Since the integral of the angular gradient between points* A, and B is equal to the difference of the wavefront displacements at points A and B divided by the distance from A to B, we may say that the instantaneous theodolite output reading is a determination of this ratio in the x direction. The effect of extension of the aperture in the y direction is merely to provide a larger aperture area (or corresponding volume of space) over which the described gradient is averaged.

Since the change in the long (spatial) period portions of the atmospheric density disturbance pattern caused by generation and decay of the elements will be small in a time interval, Δt, of a few seconds, the effect of a wind velocity V normal to the line of sight translating the spatial pattern

*c.f., Figures 5.4 and 5.5

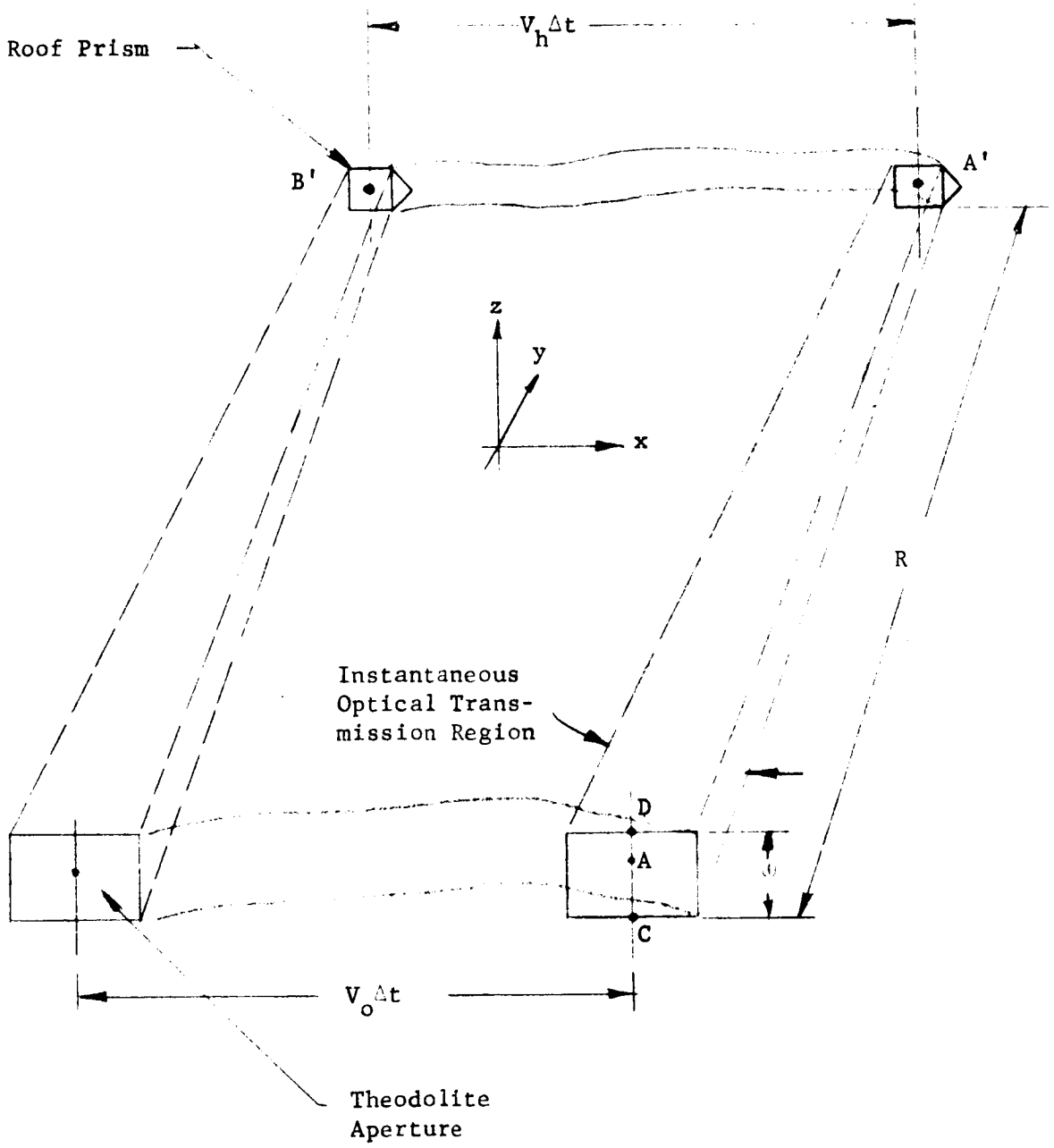

Figure 5.5 Volume of Atmosphere Averaged By Theodolite in a Time ΔT

for a time Δt is to extend the effective aperture of the instrument in the direction of the wind motion to a distance $V\Delta t$. Since the theodolite measures the average gradient of the wavefront over the area of this extended aperture and since we assume that the atmospheric disturbances are isotropic, the statistical properties of the signal provided by the theodolite will be independent of the direction of wind. For convenience, we will assume that the pattern translation by the wind is in the x direction.

To obtain an expression for the rms value of the theodolite output under the previously mentioned conditions, we will first find the mean square value of the optical path difference between the paths BB' and AA'. This will lead us to an expression for the square of the average wavefront gradient along the line $\overline{AB}$. Then, to obtain a value for the average over the whole area $\overline{AB}$ X w , we will find the expected average phase along a line $\overline{CD}$ (See Figure 5.5) based on a given particular value of the phase at a point on that line. Then the average over the whole area $\overline{AB}$ x w is the rms phase difference between points A and B divided by the distance $V\Delta t$ and multiplied by the reduced function obtained by averaging along the line CD.

Tatarski* gives a formula for the average square optical phase difference $D_s(p)$ between two points separated by a distance p as,

$$D_s(p) = 2.91\, k^2\, p^{5/3} \int_0^R C_n^2\ (\vec{r})\ dz \qquad (5.1)$$

where:

$$k = \frac{2\pi}{\lambda} \quad (cm^{-1})$$

*V.I. Tatarski, "Wave Propagation in a Turbulent Medium", translated by R.A. Silverman, McGraw-Hill Book Co., 1061, Equation 8.22, p. 170, Eq. (8.21).

P = distance between two points (cm)

C_n = structure constant of index of refraction ($cm^{-1/3}$)

z = distance along line of sight (cm)

In a horizontally stratified atmosphere near the earth's surface with local isotropy of the atmospheric disturbances we can substitute $C_n(h)$ for $C_n(\vec{r})$, where h is distance from the earth's surface. Then if the light path is from a theodolite at an elevation h_o to a roof prism at a range R and elevation angle α and return, equation (5.1) can be modified to yield the value of D_s measured at the theodolite station. Its value at the aperture is

$$D_s(p_o) = 2 \times 2.91\, k^2 \int_{h_o}^{R\sin\alpha} \csc\alpha \left[p(h) \right]^{5/3} \cdot C_n^2(h)\, dh \qquad (5.2)$$

where we have explicitly included the variation of p with height. Sutton* gives for the relationship between the average wind speed, $\bar{V}$, and height above the earth's surface, h, under nearly stable temperature conditions

$$\bar{V} = \frac{V^*}{K} \log_e \left[\frac{h + h_1}{h_1} \right] \qquad (5.3)$$

where $\frac{V^*}{K}$ is a constant, C, for a particular meteorological condition and h_1 is a function of the surface roughness. Typical values of h_1 for very smooth and for thick grass surfaces would be .001 and 2.5 cm respectively. Then letting $p = \bar{V}t$ we get

*O. G. Sutton, "Micrometeorology", McGraw-Hill Book Co., N.Y., 1953, pp. 232-233.

$$P \quad C \Delta t \log_e \left[\frac{h + h_1}{h_1} \right]$$

and dividing $D_s\ (p_o)$ by

p^2k^2 to obtain the mean square angular deviation β^2 between points A and B gives

$$\beta_{AB}^2 = 5.8 \csc\alpha \int_{h_o}^{R\sin\alpha} \left[C \Delta t \log_e \left(\frac{h + h_1}{h_1} \right) \right]^{-1/3} \cdot C_n^2\ (h)\ dh \qquad (5.4)$$

For a path (over grass) whose height varies from 300 cm to 10,000 cm, equation (5.3) predicts a velocity variation of 1.75:1. In view of this relatively small change in velocity and the strong weighting given in the integral to smaller h values (C_n^2 is proportional to $h^{-2/3}$), it will be sufficiently accurate to assume the wind speed constant at the value at h_o, viz., V_o. Thus we let,

$$\beta^2_{AB} \approx \frac{5.8 \csc\alpha}{\left[V_o \Delta t \right]^{1/3}} \int_{h_o}^{R\sin\alpha} C_n^2\ (h)\ dh \qquad (5.5)$$

Hufnagel and Stanley* give typical daytime values of $C_n(h)$ as,

$$C_n(h) \approx 3.0 \times 10^{-7}\ h^{-1/3}$$

when h is in cm, substituting this into equation (5.5), integrating, and extracting the square root gives:

$$\beta_{AB\ rms} = \frac{12.6 \times 10^{-7}}{\left[V_o \Delta t \right]^{1/6}} \left\{ \csc\alpha \left[(R\sin\alpha)^{1/3} - h_o^{1/3} \right] \right\}^{1/2} \qquad (5.6)$$

*R.E. Hufnagel and N.R. Stanley, "Modulation Transfer Function Associated with Image Transmission Through Turbulent Media", J.O.S.A. 54, No. 1, Fig. 6, p. 59, (Jan 1964).

Letting $\alpha = 25°$, R = 25,500 cm, and $h_o = 300$ cm gives,

$$\beta_{AB\ rms} = \frac{7.52 \times 10^{-6}}{\left[V_o\ \Delta t\right]^{1/6}} \text{ radians} \tag{5.7}$$

We proceed to ascertain the effect of aperture width, W, normal to the resultant wind velocity in the plane of the aperture. Now in Figure 5.5 consider any two points w_1 and w_2 on a line in the direction CD and sample the phase at w_1 and w_2 at many locations in space, the phase at each of these points fluctuates in a random fashion about an (ensemble) mean value. However, because of the proximity of w_1 and w_2, the fluctuations are partially correlated. Under these circumstances, the probability of a set of two phase disturbances, ϕ_1 and ϕ_2 may be described by the joint probability distribution,

$$P\ (\phi_1,\ \phi_2) = \frac{1}{2\pi\ \sigma^2 \sqrt{1 - \psi^2}} \exp \left[\frac{-(\phi_1^2 - 2\psi\phi_1\phi_2 + \phi_2^2)}{2\sigma^2\ (1 - \psi^2)} \right] \tag{5.8}$$

where:

σ is the rms value of a disturbance at each point ψ

$\psi(p)$ is the normalized phase correlation coefficient for 2 points a distance p apart and in an isotropic region is given by

$$\psi(p) = \frac{\langle \phi_1\ \phi_2 \rangle}{\langle \phi^2 \rangle}$$

Then for a given ϕ_1, the average value of ϕ_2 is given by,

$$\overline{\phi}_2 = \frac{\int_{-\infty}^{\infty} \phi_2\ P\ (\phi_1,\ \phi_2)\ d\phi_2}{\int_{-\infty}^{\infty} P\ (\phi_1,\ \phi_2)\ d\phi_2}$$

$$\bar{\phi}_2 = \frac{\int_{-\infty}^{\infty} \phi_2 \exp\left[\frac{2\psi\,\phi_1\,\phi_2 - \phi_2^2}{2\sigma^2\,(1-\psi^2)}\right] d\phi_2}{\int_{-\infty}^{\infty} \exp\left[\frac{2\psi\,\phi_1\,\phi_2 - \phi_2^2}{2\sigma^2\,(1-\psi^2)}\right] d\phi_2} \qquad (5.9)$$

This may be integrated by completing the square and using a substitution of variable. Let

$$-\left[\phi_2^2 - 2\psi\,\phi_1\phi_2\right] = -(\phi_2 - \psi\phi_1)^2 + \psi^2\phi_1^2 = -u^2 + v^2 \qquad (5.10)$$

where

$$\phi_2 = u + \psi\phi_1,$$

and, therefore,

$$d\phi_2 = du.$$

Substituting in equation (5.9) and cancelling gives,

$$\bar{\phi}_2 = \frac{\int_{-\infty}^{\infty} (u + \psi\phi_1) \exp\left[\frac{-u^2}{2\sigma^2\,(1-\psi^2)}\right] du}{\int_{-\infty}^{\infty} \exp\left[\frac{-u^2}{2\sigma^2\,(1-\psi^2)}\right] du} = p\phi_1 \qquad (5.11)$$

Then, if (for convenience), ϕ_1 is taken at a fixed location, w_1, at the center of AD the average over w is

$$\bar{\phi}_w = \int_{-w/2}^{w/2} \frac{\phi_1 \cdot \cdot (p)\, dp}{w} \qquad (5.12)$$

$$\bar{\phi}_w = \frac{2\phi_1}{w} \int_0^{w/2} \psi(p)\, dp. \qquad (5.12)$$

Fried and Cloud* provide values of the phase structure function D and correlation function C for slant paths near the ground permitting us to calculate $\psi(p)$, viz.,

$$C(0) \approx 2 \times 10^{-13} k^2 \csc\alpha \left\{ h_{max}^{3/2} - h_o^{3/2} \right\} \qquad (5.13)$$

and

$$D(p) \approx 1.8 \times 10^{-13} k^2 p^{5/3} \csc\alpha \left\{ h_{max}^{2/3} - h_o^{2/3} \right\}. \qquad (5.14)$$

By definition,

$$C(p) = \langle \phi_1 \phi_2 \rangle$$

and

$$D(p) = \langle (\phi_1 - \phi_2)^2 \rangle$$

where

$$\phi_1 = \phi(x)$$

and

$$\phi_2 = \phi(x + p)$$

Expanding the expression for D(p), we get,

$$D(p) = \langle \phi_1^2 + \phi_2^2 - 2\phi_1\phi_2 \rangle$$

$$= 2\langle \phi_1^2 \rangle - 2\langle \phi_1 \phi_2 \rangle$$

---

*D.L. Fried and J.D. Cloud, "The Phase Structure Function for an Atmospherically Distorted Wave Front", T.M. No. 192, Space and Information Systems Div. North Amer. Aviation, Inc., Equations 5.8 and 5.9.

and since we have

$$C(0) = \langle \phi_1^2 \rangle$$

$$D(p) = 2 \left[C(0) - C(p) \right]$$

and, from equation (5.11):

$$\psi(p) = \frac{C(p)}{C(0)} = 1 - \frac{D(p)}{2C(0)}$$

Substituting for D(p) and C(0) and assuming that $h_{max} \gg h_o$ gives for $\psi(p)$

$$\left.\begin{aligned} \psi(p) &\approx 1 - 0.45\, p^{5/3}\, (h_{max})^{-5/6} \quad \text{(p and h in meters)} \\ \text{or} \quad \psi(p) &\approx 1 - 10^{-2} p^{5/3}\, (h_{max})^{-5/6} \quad \text{(p and h in cm)} \end{aligned}\right\} \quad (5.15)$$

In our particular case, $h_{max} = 10^4$ cm and

$$p_{max} = 6 \text{ cm}$$

So that

$$p_{min} = 1 - 10^{-4} \approx 1.0. \quad (5.16)$$

We conclude that there is no significant phase or optical path averaging due to the width (w) of the theodolite aperture, and that a typical value of the rms theodolite angular seeing error β is as given by Equation (5.7), viz.,

$$\beta_{rms} \approx \frac{7.52 \times 10^{-6}}{\left[V_o \, \Delta t \right]^{1/6}} \text{ radians}$$

where

$V_o \, \Delta t$ is in cm. Note that in a dead calm ($V_o \, \Delta t$) becomes equal to the aperture diameter, 12 cm.

5.1.4 Conclusions

We conclude that for theodolite systems which average angle readings for a period of one second or more, in nearly all wind conditions the achievable accuracy should increase as the sixth root of the instrument integration time, for example by a factor of 2 as a result of increasing the integration time from one to 64 seconds. Increasing the aperture diameter should have a negligible effect. To achieve the effect of time integration of the atmospheric inhomogeneities it is necessary to locate the theodolite aperture a sufficient distance above the terrain to have a good horizontal wind component. A minimum height might be three feet. Shortening the base line optical path will improve the accuracy as the square root of the sine of the angle of elevation of the line of sight.

The conclusion drawn above concerning the increase in the accuracy of a theodolite system achievable by increasing the instrument integration time is verified by inspection of the shape of the noise power spectrum calculated from data taken with a roof prism used as the target. The slope of the power spectrum within the region defined by

$$f \propto \frac{Vo}{D} \tag{5.18}$$

where

f = frequency (cycles per second)

Vo = transverse wind velocity

D = system aperture

is shown in figures 3.7, 3.8 and 3.9 to be -2/3. Thus we can express the power spectrum to be

$$P = cf^{-2/3}$$

where

P = power density in arc sec^2/cps

c = constant

If we define R as the ratio of squared noise energy contained in the band $o < f < fc$ to the total squared noise energy σ^2, then

$$R = \frac{1}{\sigma^2}\int_o^f P df = \frac{c}{\sigma^2}\int_o^f f^{-2/3}\, df \qquad (5.19)$$

$$R = \frac{c' f^{1/3}}{\sigma^2}$$

where c' is a constant.

We can now define r as the ratio of the noise energy contained in the frequency range of $0 < f < f_c$ to the total noise energy σ. Then

$$r = \sqrt{R} = \frac{c'' f^{1/6}}{\sigma} \qquad (5.20)$$

If we recall that the cut-off frequency is inversely proportional to the integrating time, Δt, of the instrument, then 5.20 becomes

$$r = c''/\sigma(\Delta t)^{1/6}$$

which agrees with the conclusion drawn above.

SECTION VI

COMPARISON OF A ROOF PRISM WITH A TRIHEDRAL

6.1 INTRODUCTION

Much interest has been centered on the use of trihedrals for various functions in azimuth laying systems. Since the effect of a turbulent atmosphere on a theodolite-trihedral system has proven to be extremely difficult to describe analytically, a series of experiments has been performed for the purpose of accumulating empirical knowledge about the effect of a turbulent atmosphere on such a system. The experiment described below has been designed to provide a direct comparison between the various properties (power spectrum, rms error, etc.) of a theodolite system using a trihedral and a roof prism. This will enable a comparison of the theory as outlined in previous chapters with the characteristics of the trihedral.

Experimental data was taken on the Perkin-Elmer 850' Seeing Range at Wilton, Connecticut, using a Long Range Theodolite with a prism array consisting of a roof prism, a trihedral, and a dichroic beamsplitter used in place of a single prism as the theodolite target, (see figure 6.1).

The dichroic beamsplitter was designed to pass all radiation between 0.7 μ and 1.3 μ and reflect all radiation between 1.3 μ and 2.7 μ. Since the two error channels of the theodolite operate in these regions, all energy seen by one channel represents energy transmitted through the beamsplitter to the roof prism, and all the energy seen by the second channel

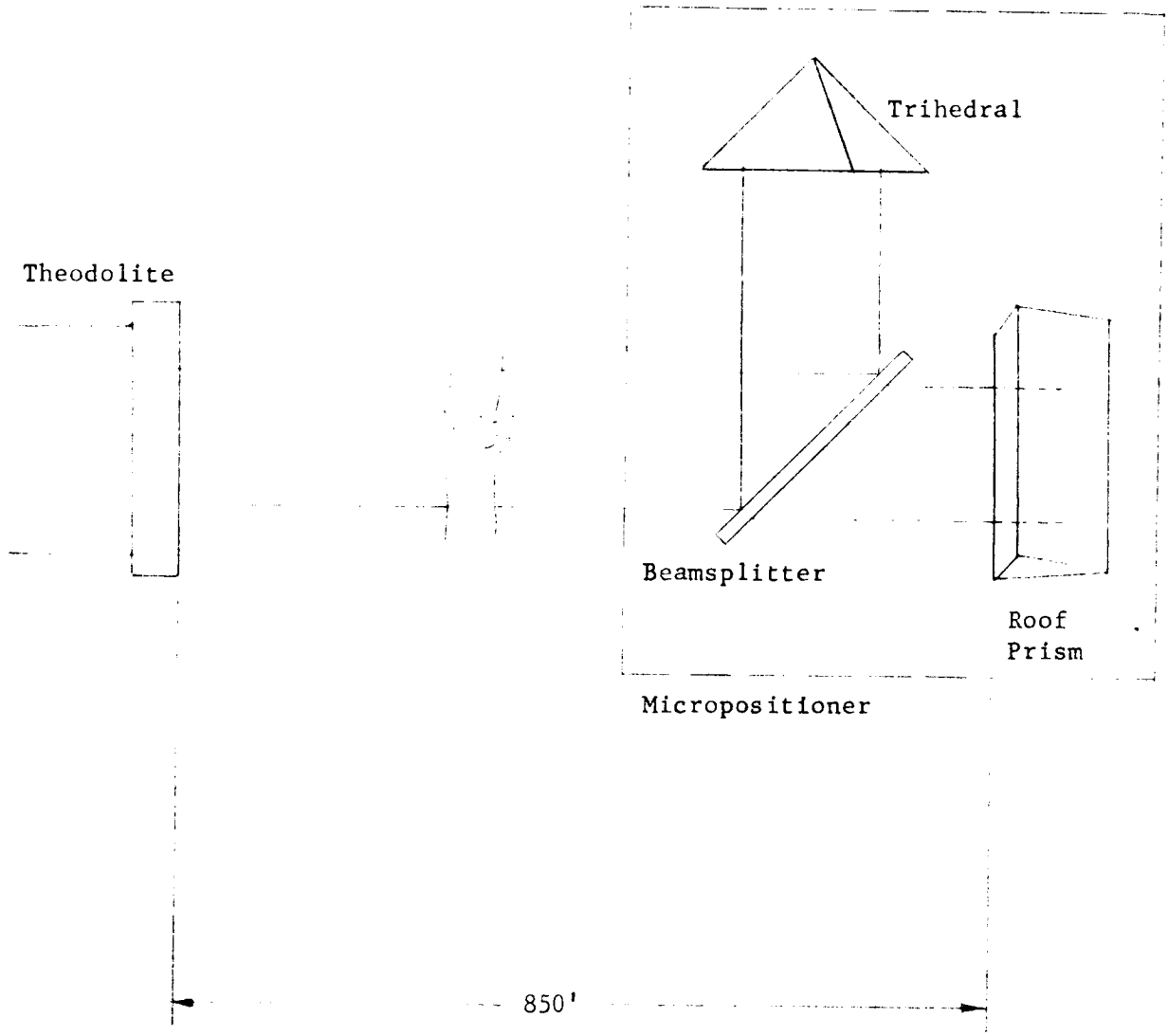

Figure 6.1

Experimental Arrangement for Comparison of a
Roof Prism with a Trihedral

represents only energy reflected by the beamsplitter to the trihedral. The apertures of the two prisms were imaged on one another. Thus the two error channels produce two simultaneous error signals, one from a roof prism and one from a trihedral, obtained from two physically coincident beams traversing the same volume of air. The use of this beamsplitter arrangement has the fundamental advantage of permitting an instantaneous comparison of the error signals obtained with the two types of return optics. Such a comparison is necessary if conclusions are to be drawn about the possibility of atmospheric turbulence compensation through real-time combination of error signals in shimmer subtraction networks. The arrangement also has the advantage of eliminating unknown effects of slowly varying meteorological parameters, which can have unpredictable effects on the comparison of the statistical properties of the two prisms calculated from raw data taken several minutes apart. The data taken is presented in three forms: power spectrum plots, auto-correlation and cross-correlation plots, and rms angular seeing deviations data.

6.2 CALCULATION OF POWER SPECTRUM

In the calculation of the power spectrum of the theodolite error signal obtained with a roof prism as the target, the statement was made that the path reversal did not affect the statistics of the error signal. However, with the use of a trihedral in place of a roof prism, the path reversal does result in a fundamental change in the statistics of the error signal.

This change stems from the different geometrical properties of the two types of prisms. In azimuth, the roof prism acts like a flat mirror, and

any error of an incoming wavefront* (defined as the angle between the wavefront and the prism axis) is preserved in the reflected wavefront.

The geometrical characteristics of the trihedral, on the other hand, cause all incoming wavefronts to be reflected back parallel to the direction of propagation of the incident beam. Thus, from a beam traveling through a non-homogenous medium to a trihedral and being reflecting back through the same medium, the net angular deviation of the reflected beam relative to the incident beam will be the difference between the deviations undergone by the beam in the medium on the two passes. Recall that for the roof prism, the net deviation is the sum of the two separate deviations.

Now let us consider separately the low and high frequency regions of the power spectrum that were discussed in Sections 3.4 and 3.5.

We define the low frequency region as that in which $u < 1$. For the roof prism, Section 3.5 showed that most of the energy contained in the frequency components of the atmospheric induced noise power spectrum in the region $u < 1$ is contained in the phenomenon of image shift. Since the phenomenon of image shift results from a constant deviation across the entire effective wavefront of the beam, and since the net deviation of a beam element passing through a turbulent atmosphere to a trihedral and reflected back to the theodolite is equal to the difference between the magnitude of the deviations seen on each traverse of

---

* In this analysis we assume that the result of turbulence is to induce a random variation in angle of arrival but to leave the wavefront plane.

the atmosphere, the net deviation of the theodolite beam reflected back by a trihedral is zero. Thus, there is no noise energy contribution to the error signal due to image shift. In the real physical case of turbulons larger than the aperture being swept across the beam, there is some image blur that occurs because of "fine structure" of the index variations across the turbulon. Thus, there is some residual noise energy in this region $u < 1$, but we would expect the total noise energy in this region to be much less than the total noise in the corresponding region in the power spectrum of a roof prism.

We define the high frequency region as that where $u > 1$. Since the noise energy in this region comes from turbulons whose size is smaller than the limiting aperture of the system, the wavefront deviations seen by the incident and reflected beams will be largely uncorrelated, and will not cancel. Thus, we would expect the high frequency content of the power spectrum of the trihedral to be of the same order of magnitude as the high frequency content of the power spectrum of the roof prism.

Examination of Figure 6.2, which shows a typical plot of the power spectra of trihedral and roof prisms calculated from data taken simultaneously over the same volume of air, shows less energy density at low frequencies in the noise from a trihedral than in the power spectrum of a roof prism. In addition, it is worth noting that the power spectrum of the trihedral does not exhibit a corner frequency, but exhibits a constant frequency dependence throughout the entire frequency range of interest. In Section 3.6, the change in slope of the power spectrum of the roof prism was shown to occur in the region in which the noise phenomenon was changing from image blur to image motion.

Since the trihedral is fundamentally insensitive to image motion, this change in slope is not observed in the power spectrum of the trihedral.

An approximate form for the power spectrum of the trihedral can be given by

$$P_t(f) \quad K(f)\, P_r(f) \tag{6.1}$$

where

$f = \omega/2\pi$

$P_t(f)$ = power spectrum of trihedral

$P_r(f)$ = power spectrum of roof

and

$K(f)$ = trihedral power spectrum weighting function.

$K(f)$, the trihedral power spectrum weighting function, takes into account the trihedral's insensitivity to the insertion of a fixed wedge into the beam (which produces image shift in a roof prism) as well as the averaging effect that occurs over the aperture of the trihedral.

This averaging effect arises from the fact that rays passing through a turbulon and entering near the center of the front face of the trihedral are not deviated as much as rays entering near the edges, since the incident and reflected paths are closer for light incident on the center of the trihedral's aperture, than for light incident near the edge.

The derivation of $K(f)$ will be performed in two steps - the first being the formulation of a trihedral power spectrum weighting function $K(f)$, defined by

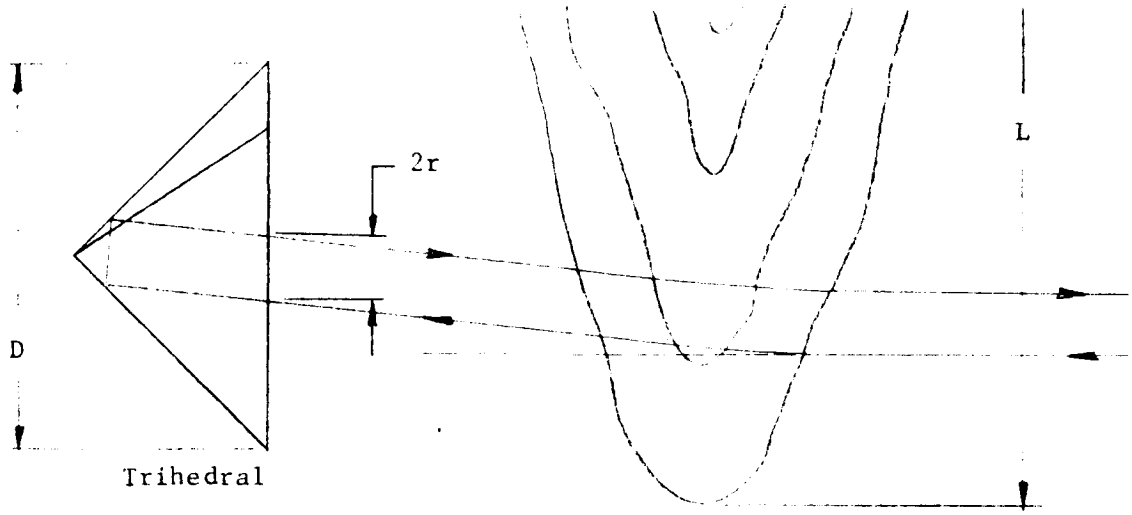

Case 1: $\frac{L}{r} > 6$

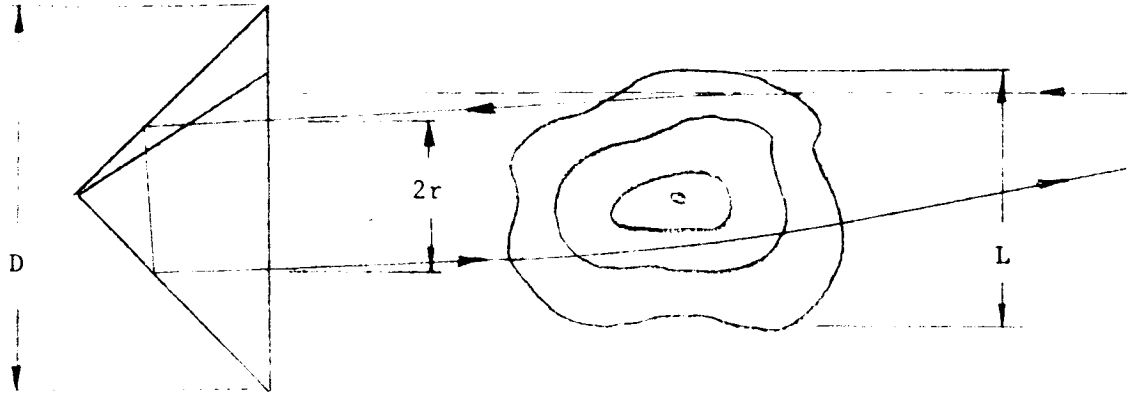

Case 2: $\frac{L}{r}$ 2

Figure 6.3. Notation for Comparison of Trihedral With Roof Prism

$$p_t(f) = k(f)\, p_r(f) \qquad (6.2)$$

where these symbols have similar definitions to the corresponding ones in Equation 6.1 except that they all refer to a thin annulus of radius r. The second step will be to integrate this thin annulus across the entire face of the trihedral, thus taking into account the averaging effect mentioned above.

Previously, we showed that a turbulon of size L translating across a theodolite beam at some transverse velocity v will cause a wavefront disturbance of duration $\tau = L/v$. Since as an approximation, we can say

$$f = \frac{1}{\tau} = v/L$$

we can write k(f) as k(v/L, r).

Let $k(\frac{v}{L}, r)$ be defined as follows:

1) $k(\frac{v}{L}, r) = 0$ For frequencies leading to the phenomenon of image shift in roof prisms. This occurs for turbulons whose physical size, L, is greater than about three times the diameter of the annulus, i.e., $L/r > 6$.

2) $k(\frac{v}{L}, r) = 1$ For frequencies leading to the phenomenon of image blur. This is caused by turbulons whose physical size, L, is smaller than the diameter of the annulus, i.e. $L/r < 2$

3) $k(\frac{v}{L}, r)$ Varies linearly with L/r within the region $2 \leq L/r \leq 6$ i.e., for frequencies leading to both the phenomena image shift and image blur.

Thus

$$k(\frac{v}{L}, r) = \begin{cases} 1 \text{ for } L/r \leq 2 \\ \frac{3}{2} - \frac{L}{4r} \text{ for } 2 \leq \frac{L}{r} \leq 6 \\ 0 \text{ for } L/r > 6 \end{cases} \tag{6.4}$$

We can now find the value of $K(f)$ $K(\frac{v}{L})$ by integrating over the aperture and normalizing.

$$K(\frac{v}{L}, D) = \frac{\int_0^{D/2} k(\frac{v}{L}, r)\, 2\pi r\, dr}{\int_0^{D/2} 2\pi r\, dr} = \frac{8}{D^2} \int_0^{D/2} k(\frac{v}{L}, r)\, r\, dr \tag{6.5}$$

Evaluation of 6.5 involves three separate calculations corresponding to three ranges of L/D.

Case 1: $L/D \leq 1$

$$K_1(\frac{v}{L}, D) = \frac{8}{D^2} \int_{L/6}^{L/2} \left(\frac{3}{2} - \frac{L}{4r}\right) r\, dr + \frac{8}{D^2} \int_{L/2}^{D/2} r\, dr \tag{6.6}$$

Case 2: $1 \leq \frac{L}{D} \leq 3$

$$K_2(\frac{v}{L}, D) = \frac{3}{2} - \frac{L}{D} + \frac{1}{6}(\frac{L}{D})^2 \tag{6.7}$$

Case 3: $L/D \geq 3$

$$K_3(\frac{v}{L}, D) = 0 \tag{6.8}$$

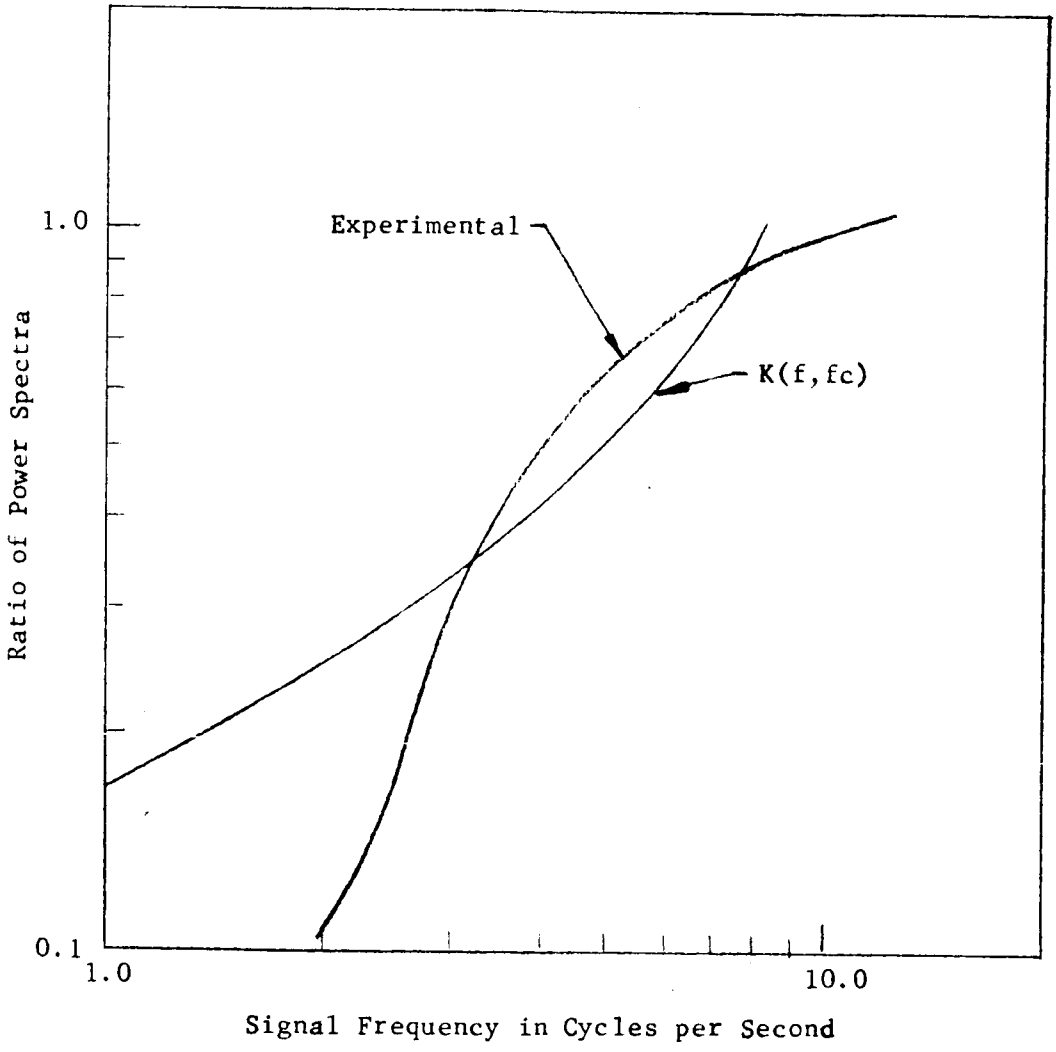

Figure 6.4 Comparison of Calculation with Measured Ratio of Trihedral to Roof Prism Power Spectrum

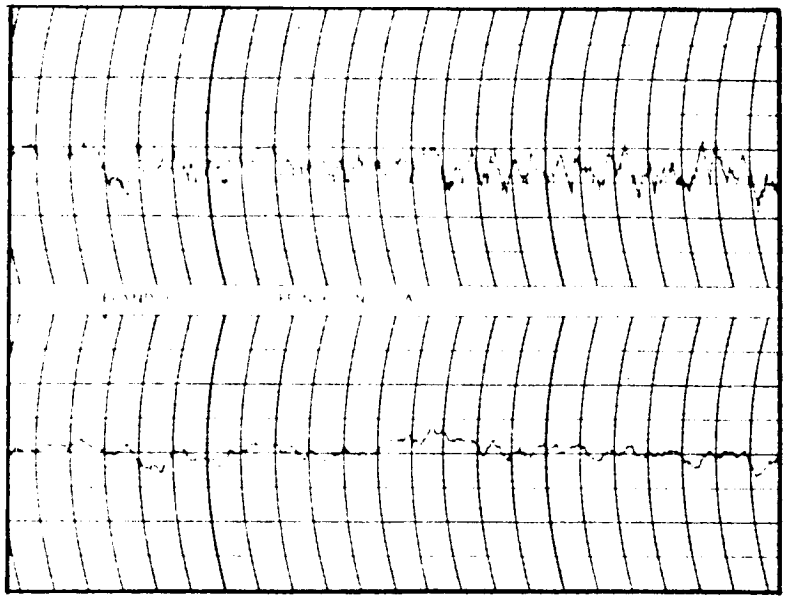

Upper Trace: Trihedral Return Scale: 0.4 volts full scale

Lower Trace: Roof Prism Return Scale: 2.0 volts full scale

Figure 6.5 Comparison of Simultaneous Raw Error Signals From Trihedral and Roof Prisms Over Physically Coincident Beams Through 850 Feet of Atmosphere

We have previously defined the critical frequency as

$$f_c \quad D/v$$

Substituting into Equation 6.3 we get

$$L/D = \frac{L}{v} \cdot \frac{v}{D} = \frac{L}{vf_c} = f/f_c \tag{6.9}$$

Hence $K(\frac{v}{L}, D)$ can be written as

$$K(f,f_c) = \begin{cases} 1 - \frac{1}{3}(f/f_c)^2 & \text{for } f < f_c \\ \frac{3}{2} - f/f_c + \frac{1}{6}(f/f_c)^2 & \text{for } f_c < f < 3f_c \\ 0 & \text{for } f > 3f_c \end{cases} \tag{6.10}$$

Figure 6.4 shows the form of K(f,fc), along with the value of the ratio

$$P_t(f) \; / \; P_r(f)$$

obtained experimentally.

6.3 RMS SEEING DEVIATIONS

As noted in Section 6.2, when the trihedral is used as a target prism it is fundamentally insensitive to image motion. Thus, the rms seeing deviations, calculated from the raw strip chart trihedral data, a sample of which is shown in Figure 6.5, is composed of energy contained in the phenomenon of image blur.

Since the error signal derived from the use of a roof prism contains both image shift and image blur, the ratio of these two quantities will

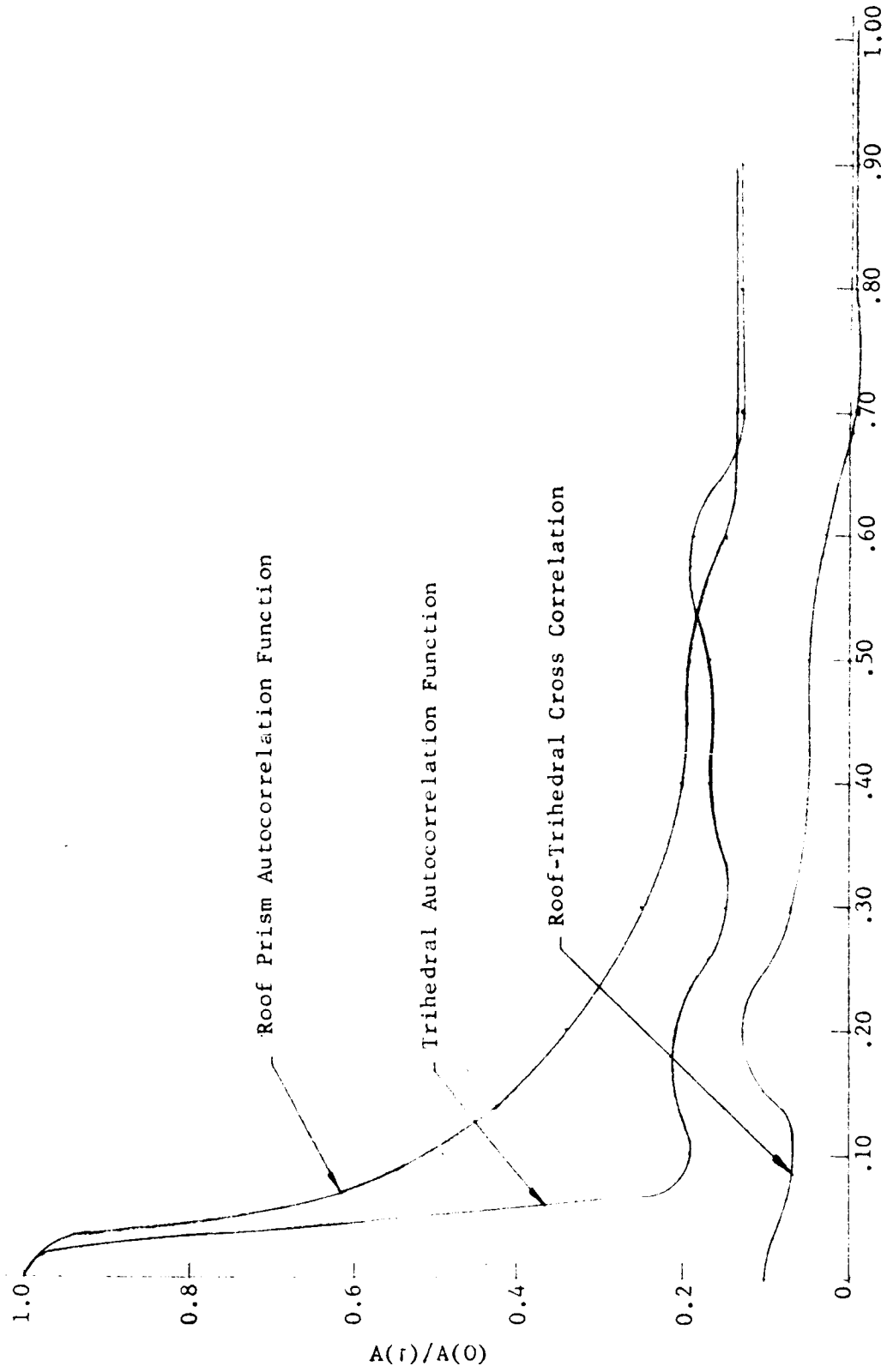

Figure 6.6. Correlation Functions of Trihedral and Roof Prism

give a rough measure of the ratio of energy contained in the two phenomena. Data taken yields ratios about .14 for trihedral error to roof error, indicating that approximately 86% of the error signal due to atmospheric turbulence is contained in image shift.

6.4 COMPARISON OF INSTANTANEOUS TRIHEDRAL AND ROOF ERROR SIGNALS

The suggestion has often been made that it is possible to use the error signal obtained from a trihedral in a "shimmer subtraction network" to remove the effect of atmospheric turbulence on the error signal obtained with a roof prism. The test set-up, as described in section 6.1, was used to investigate this hypothesis by permitting the comparison of simultaneous error signals obtained from two physically coincident beams, one beam illuminating a roof prism and the other beam illuminating a trihedral..

The two raw error signals (as shown in Figure 6.5) were digitized, and the following data computed and illustrated in Figures 6.6 and 6.7:

(1) Auto-correlation function and power density spectrum for each error signal.

(2) Cross-correlation function and cross power density spectrum of the two error signals.

The data was calculated to yield the low frequency portion of the power spectras within the bandpass of the theodolite, since any shimmer subtraction network must operate on only that portion of the atmospheric noise signal within the bandwidth of the theodolite system. The power spectrum calculated for the roof shows the -2/3 power law characteristic of the low frequency region, while

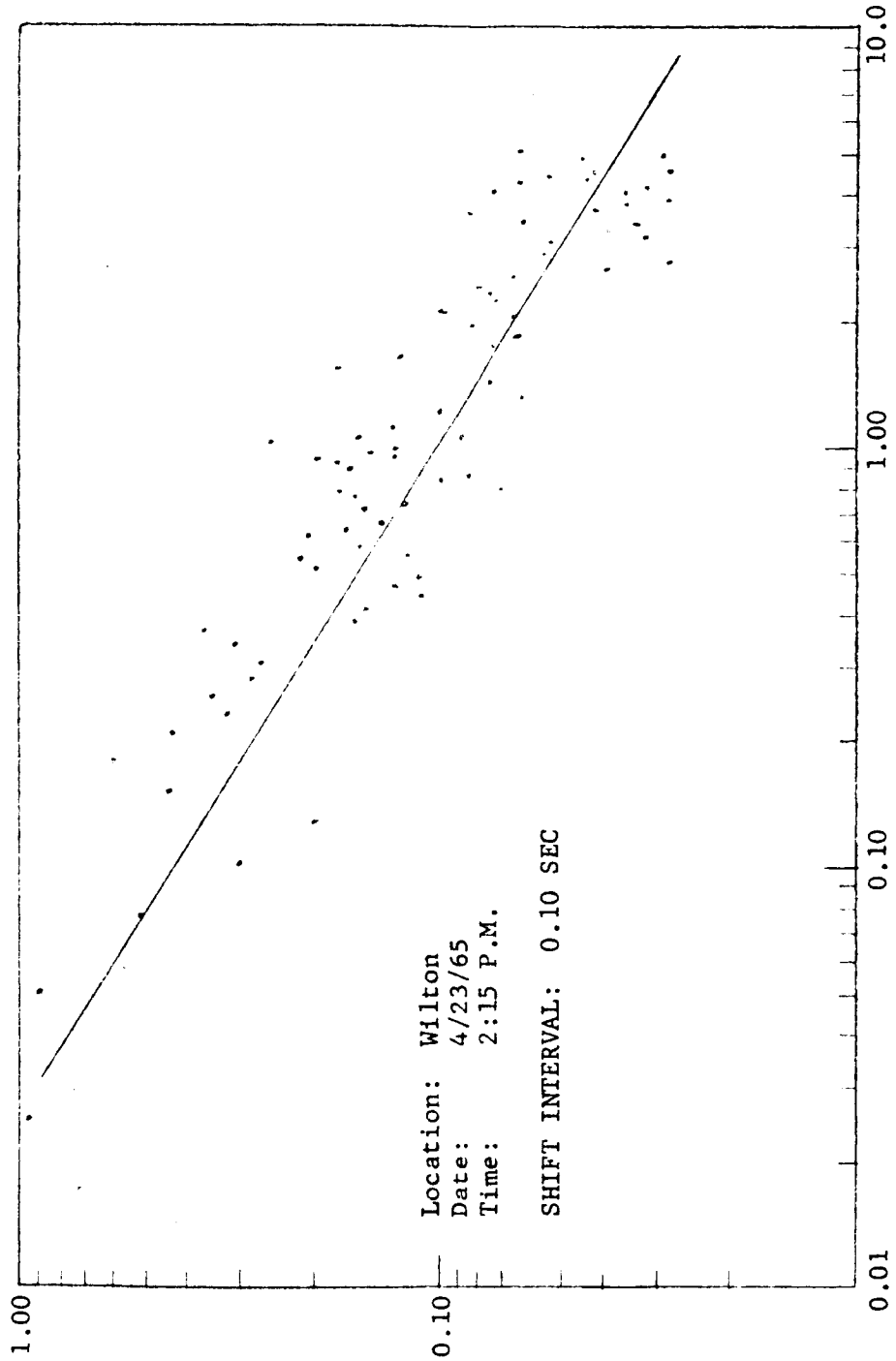

Figure 6.7a Power Spectrum of Trihedral Return

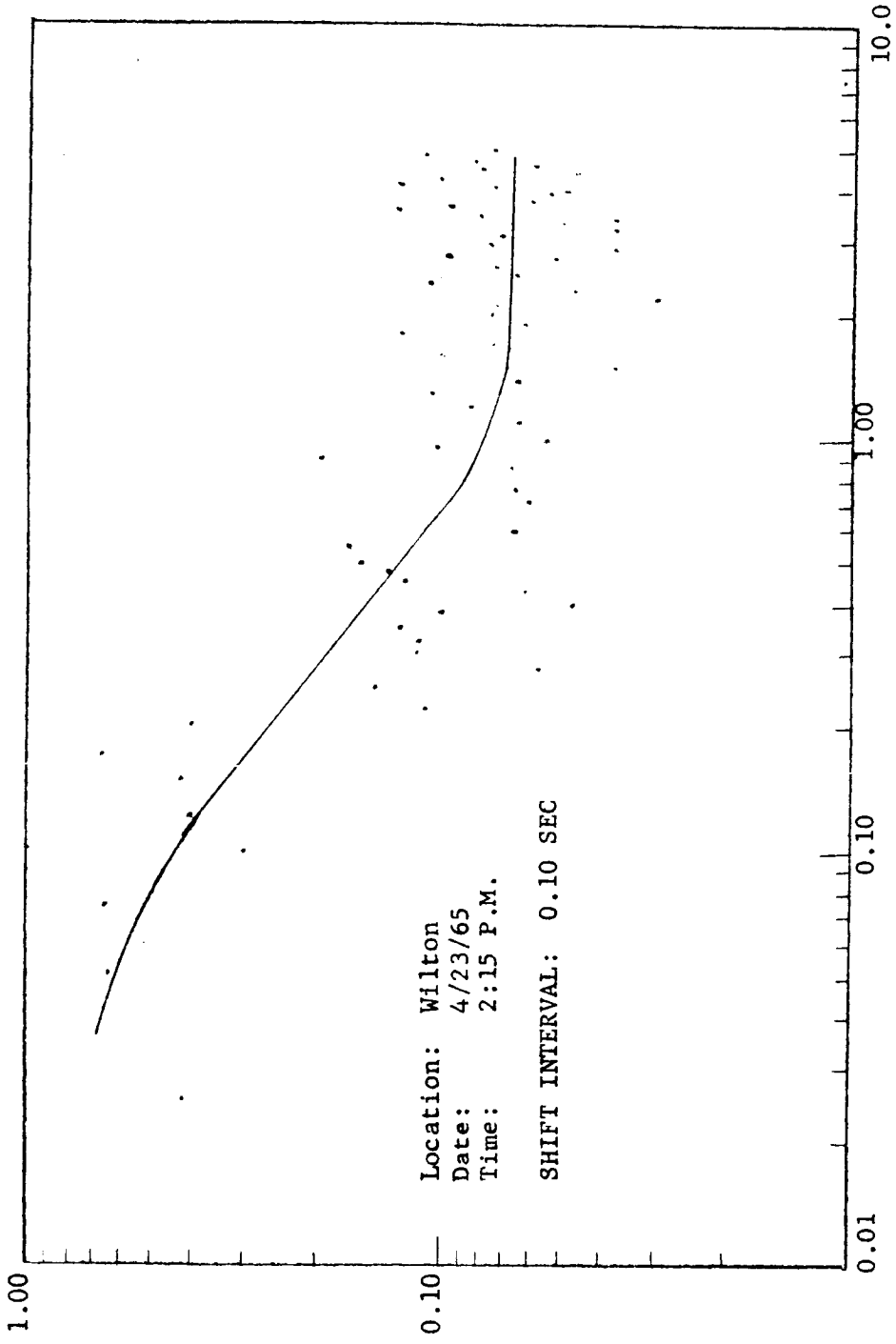

Figure 6.7b Power Spectrum of Roof Prism Return

the power spectrum calculated for the retro exhibits an apparent leveling off in the region around 5 cps. This leveling is probably due to computational errors arising from the small amount of noise energy contained in the region.

The cross power density spectrum, which is a measure of the error signal energy common to the error signals obtained from the roof and trihedral, was calculated and found to contain both positive and negative values throughout the frequency region. Physically, the cross power spectrum is essentially zero, with the calculated positive and negative values arising from the approximate nature of the computer program.

Because the cross power spectrum appears to be essentially zero, there is little or no atmosphere noise component common to both the roof and the trihedral error signals, precluding the possibility of combining the two in a filter network. This conclusion is borne out by examination of the cross-correlation function, shown in Figure 6.6, which shows a low cross-correlation between the two signals.

The conclusions drawn here are based on only two sets of data; a more detailed examination based on a larger body of experimental data should be made, including an investigation of the high frequency portions of the power spectrum, to firm up the conclusions drawn above.

SECTION VII

CONCLUSION

7.1 SUMMARY OF EXPERIMENTS

In response to the objectives of this study a model LR2A/GS Alignment Theodolite was set up on a range of 850 foot length at the Perkin-Elmer Corporation in Wilton, Connecticut, together with suitable return optics. In addition, instruments for measurement of temperature and wind velocity were disposed along this 850 foot path and readings of these meteorological parameters were taken while the deviations of the return beam to the theodolite were recorded on a strip chart recorder.

The return optics used were a roof prism and a trihedral, the latter being used for a study of possible methods of compensation for errors due to atmospheric turbulence.

In a separate series of experiments, a square aperture was illuminated and the resulting object collimated and projected down the 850 foot range to a small telescope and a camera. The resulting photographs were processed and subjected to analysis by a microdensitometer whose output record was used to compute the modulation transfer function of the system and hence the modulation transfer function of the atmosphere.

The results of these experiments were used to compare predictions of the atmospheric seeing with actual measurements.

7.2 COMPARISON OF RMS SEEING WITH PREDICTIONS FROM TEMPERATURE MEASUREMENTS

Figures 2.1 and 2.2 gives an indication of the agreement of our observations with the predictions of the current theory. Although there is a spread of the points about the average line in that graph, when the difficulties of measurement and the non-uniformity of the path are considered, there is surprising agreement.

There were errors due to the macroscopic nature of the measurements made. Temperature gradients were measured using laboratory type thermometers shielded from direct sunlight. More accurate results might have been obtained using thermometers specifically designed for measuring the temperature of air in motion and if such instruments were designed and constructed to have fast response times and could have their output recorded so that temperature gradients could be recorded as a function of time. The instrumentation required for such an arrangement would have led to expenditures outside the scope and funding of this study and hence it was carried out with the standard instruments available.

Another extension of these experiments would involve the construction of a range with no features in the adjacent area which could perturb the air flow and thermal pattern. After our instruments were assembled and readings had been started it was found that the path used was indeed subject to perturbing influences of significance. Obviously, the construction of such an ideal facility could only be undertaken with specific authorization. Also, the results of experiments taken on the existing range certainly justified its use.

We conclude that the theoretical model of the turbulent atmosphere in the latest formulation by R. E. Hufnagel and N. R. Stanley can be used to predict a value for the rms angular error introduced by the atmosphere and detected by a theodolite.

7.3 POWER SPECTRUM OF ATMOSPHERIC SEEING

The data taken, when converted to Power Density Spectra, did indeed conform to the predictions of the theory. In addition, it was possible to explain several anomalies by use of this technique. Specifically, the error introduced into the data by vibration of the gantry at Cape Kennedy is immediately apparent as mentioned in the discussion of Figures 3.4 and 3.5 in Section III. Also an eccentricity in the drive mechanism of the strip chart recorder is shown clearly in Figure 3.8.

Some deviations from the theory are discussed at the conclusion of Section III and they fall into the pattern of limitations of the current theory and also limitations imposed by the equipment and site authorized for this study.

7.4 MODULATION TRANSFER FUNCTION OF THE ATMOSPHERE

The major results of this portion of the study have been the actual determination of the atmospheric modulation transfer function. The dominance of the atmosphere in determining the limitation on the resolution of the alignment theodolite is clear from Figure 4.3 and the associated discussion. The effects of this on the design of future systems is certainly a subject worth some consideration. As indicated in the text, "trade-offs" between cost and small percentage changes in resolution are involved. Such considerations must depend on the particular design being evaluated and hence do not belong in this study.

7.5 TIME INTEGRATION

The results of Section V give some clues to the effect of varying system parameters on accuracy. The implications extend beyond the immediate system of theodolite and return prism and consequently additional analysis is required. This would involve a study of the inertial platform performance and also the sources of non-atmospheric disturbances (such as motion of the vehicle on the pad) on the performance of the larger system.

7.6 COMPARISON OF THE ERROR SIGNAL CHARACTERISTIC ROOF PRISMS AND TRIHEDRALS

The experiments conducted to compare noise in the return signal from a roof prism with that from a trihedral led to the conclusion that there was essentially no correlation between the two signals in the portion of the spectrum within the passband of the theodolite. It is conceivable that in the higher frequency region of the noise spectra some correlation exists, but the low fraction of the total noise power contained in higher frequency regions, coupled with the one cycle per second cut-off of the theodolite, makes the possibility of such appreciable correlation of academic interest only, with no practical application to the specific problem at hand.

7.7 SUMMARY

In general we may conclude that the magnitude of the effect of atmospheric turbulence on present Alignment Theodolites is fairly well described by present theory and there appears to be no straightforward way of obtaining a significant improvement in the performance of the present system. The methods of optimizing the present system discussed in the body of the report lead only to small gains and a study of their advisability in the light of economic and larger system considerations should be made.

APPENDIX A

ATMOSPHERIC ATTENUATION IN THE VISIBLE AND NEAR-INFRARED SPECTRUM

By R. W. Austin
Scripps Oceanographic Inst.

1.0 ASSUMPTIONS

1.1 It is understood that the space vehicles which are being aligned will be located in a marine atmospheric environment.

1.2 The optical path (one way) between the alignment equipment and the space vehicle will be between 1000 and 3000 feet.

1.3 The optical path of the alignment equipment may be between 0° and 30° elevation. (It is, however, assumed that the maximum height of the optical path will not exceed 300 feet under any conditions.)

1.4 The wave length regions being considered will lie between 0.4 and 2.0 microns.

2.0 GENERAL CONSIDERATIONS

2.1 ATTENUATION EFFECTS WITH WAVELENGTH

A definite reduction in atmospheric attenuation may be realized by using the near-infrared region of the spectrum in lieu of the visible spectrum. This is not, of course, a panacea to problems engendered by poor atmospheric visibility situations. It is doubtful that this improvement will be of any great significance unless the alignment system is already operating with a low signal-to-noise ratio under clear weather conditions. We have found, for example, that the Perkin-Elmer Model 523-0005 long-range azimuth theodolite, using visible radiation, would operate satisfactorily over a distance of 100 feet under conditions when the one-way atmospheric transmittance was down to 12 to 14%.

It is instructive to relate these findings to the problem under consideration. For example, if the even longer-range system under consideration were to have similar performance capabilities, limiting operation at 14% transmittance for the 3000-foot optical path would occur when the atmospheric transmittance was 2% per nautical mile. This corresponds to a meteorological range of 1 nautical mile. For the 1000-foot path, the same situation would occur when the meteorological range is 1/3 nautical mile. Under these circumstances of low atmospheric transmittance we can expect a large amount of large-particle scattering and large amounts of precipitable water in the path. The presence of large-particle scattering reduces the benefit which accrues through the use of the near-infrared as particles whose diameter is large compared with the wavelength tend to be non-selective in their scattering. The presence of precipitable water means attenuation of portions of the infrared spectrum under consideration, i.e., strong water vapor absorption bands exist at 0.9, 1.1, 1.3-1.4, 1.8-1.9 microns. See Larmore (1956) and Passman and Larmore (1956).

The work of Knestrick, Cosden, and Curcio (1961) shows that under moderately hazy conditions some improvement can be obtained (if one neglects absorption and considers only scattering) by shifting the wavelength of operation from the visible to the near-infrared. Their minimum meteorological range was, however, 3 nautical miles, and the data showed a general trend toward a reduction in the improvement which might be expected as the meteorological range approached this value. Their work was done in the Chesapeake Bay area which meets the general requirements for a marine atmosphere.

Kernick, Zitter and Williams (1959) in a report containing considerable information which is germane to the problem under consideration show by their analysis that the scattering coefficient (which they inaccurately refer to as an absorption coefficient) can be expected to vary with wavelength raised to a negative power between -1 and zero. Their experimental results, which were obtained by measurements in infrared "windows" under various adverse atmospheric conditions, agree generally with this finding. It should be pointed out, however, that no spectral preference was noted when actual precipitation occurred - only when foggy conditions prevailed. They reasonably attribute this to the fact that the droplet size (greater than 50 microns for precipitation) was large compared to the wavelengths used in their tests, i.e., 1.7 to 12 microns. Similarly, we may expect for the wavelengths between 0.4 and 2.0 microns which we are considering that definitely less increase in transmittance with increasing wavelength will be observed in fogs than they found in the spectral region which they investigated because of the many particles present in fogs with sizes larger than 2.0 microns.

Hulburt (1949) tabulated attenuation coefficients for wavelengths from 0.25 to 1.0 microns for conditions varying from very clear to hazy. His compilation also demonstrates that the change in attenuation with wavelength becomes less pronounced as the "visual range" (or "meteorological range" in Duntley's terminology) becomes smaller. Unfortunately Hulburt's tables do not extend beyond 1 micron and do not cover the shorter meteorological range in which we are particularly interested. (See attached reprint.)

It was our experience in the tests which we ran on the Model 523-0005 that the ultimate limitation under severe atmospheric attenuation conditions was the fluctuation in received signal caused by variations in path transmittance and in back-scattered flux. Our observations, of course, were made with a system using a much shorter path and therefore were typical of the moment-to-moment variations in transmission which occur in extremely dense fogs. An indication of the variability which may be expected for the meteorological ranges critical or limiting for the longer optical paths under consideration could be obtained by observation of the fluctuations in Douglas transmissometer records. These could be obtained from some local air field which is equipped with one of these instruments. One would expect that the transmission situation would become more stable as the transmission increases and the limitation which was noted for the relatively short path may be less important. Furthermore, the noise caused by scintillation effects will become larger for the longer path lengths of 1000 to 3000 feet. This may markedly reduce clear weather signal-to-noise ratio and change the conclusions based on the Visibility Laboratory's study of the Model 523-0005. The changes would be in magnitude, however, and not in concept.

Many of the studies reviewed were for overwater or marine environments and no significant change would be expected for any specific maritime location.

In conclusion, we can summarize the wavelength effects on attenuation by stating that for an inherently high performance system with a moderately large signal-to-noise performance margin in the clear-weather situation,

the effects of atmospheric transmission probably will not become significant until a light fog or dense haze situation exists. Under these conditions the benefits which will accrue through the use of near-infrared as opposed to visible radiation will be markedly less than would be found for the more usual atmospheric clarities. The decision of wavelength region may well be determined by other considerations.

2.2 SLANT PATHS

For the lower layers of the atmosphere (0 to 300 feet) we know of no work which has been reported which bears specifically on the problem of slant path transmission as a function of wavelength. However, we would expect no significant difference to exist over that which occurs for horizontal paths of sight. There have been studies of slant visibility and of the stratification of the lower atmosphere in the visible region. Many of these studies were performed by measuring the light scattered from searchlights at night. Hulburt (1937) and Stewart et al (1949 at NRL and Beggs and Waldram in England have reported work of this type. They have not dealt with the lower few hundred feet in sufficient detail for our purposes. (See Middleton "Vision Through the Atmosphere," Chapter 7 for additional specific references.)

It is not felt that any significant generalizations can be made about this lower layer, especially over water, as there are so many variables involved. For example, fog may exist in a layer from the surface to 100 feet or from 100 feet to, say, 200 feet with perhaps equal frequency in many areas, depending upon local meteorological conditions. If a temperature inversion

exists in the area a dense and rather well mixed haze or smog may exist to altitudes of several hundred feet, and little vertical change in transmission would be found. In order to make any significant remarks about the effects of slant paths a study would have to be based on a knowledge of the local characteristics of the specific sites under consideration. (It is assumed that the phrase "over open sea" means over water but near a coastal land mass which could have a major effect on the local meteorology.) One small generalization can be made relative to over-water paths. This is that the first ten to twenty feet above the water frequently, following a period of high wind, will contain large quantities of salt nuclei which with high humidity will form a haze of significantly low transmission. This would indicate that any path, whether slant or horizontal, should not be close to the surface. It would be assumed that the practical problem of keeping the optics clean would dictate that the path would be above these heights.

2.3 SCATTERING

With the exception of the specific mention which was made of the near-infrared absorption bands in Section 2.1, all other attenuation effects in Section 2.1 and 2.2 are due to scattering, and the information included in these sections is responsive to the request for information ...."directly applicable to .... (3) Scattering of radiation for conditions in (1) and (2)."

Anticipating that other information such as scattering functions for natural aerosols would be of interest, reports by Deirmendjian (1962), Fenn (1962) who used a polar nephelometer built for him by Perkin-Elmer

for his measurements, and Pritchard and Blackwell (1957) are included in the bibliography. In addition, some of the reports which were listed because of their coverage of the general attenuation problem also cover scattering functions specifically.

2.4 HUMIDITY AND PARTICLE DENSITY GRADIENTS

The remarks under Section 2.2 regarding a requirement for more specific knowledge of the local meteorology in the area of the launch site apply here also. No information is included which covers the humidity gradient situation directly. A number of references are given which contain droplet size distributions for various conditions. The work of Woodcock (1953), (1952), (1949) and Moore (1954), (1952) provides data on salt nuclei size distributions over water and some information relative to gradients. Wright (1940) discusses "atmospheric opacity" and its relation to relative humidity.

2.5 FOG DISSIPATION AND PENETRATION

In the event that there is interest in the removal of fog by various methods, four reports are included which cover this general area in a rather complete manner. These are: Downie and Smith (1958), Junge (1958), Arthur D. Little, Inc. (1956), and the classic paper by Houghton and Radford (1938). After considerably study of the various methods that have been suggested, it seemed to us that none of the methods offered a really satisfactory solution to the problem of complete removal of the offending fog. This is even more likely to be the situation with the longer paths which are involved in the current study. The methods which seem to offer the most

promise in other respects involve the addition of heat to the general area which includes the optical path. This, of course, carries with it the very real possibility of introducing additional atmospheric turbulence or shimmer, which for the long path and high angular accuracy being sought may make the cure worse than the disease.

The report by Nathan (1957) suggests an interesting possibility of being able to optically penetrate the fog by means of polarization techniques. Such methods were investigated by the Visibility Laboratory for application to the long-range theodolite 523-0005. This method was not found to effect any appreciable improvement for the reasons given in Section 2.1 However, with the longer-range system and the possibility of a smaller amount of fluctuation in transmission and back-scatter occurring at the limiting value of transmission, it may be possible to realize an improvement in the operation of the system through the use of these techniques.

3.0 BIBLIOGRAPHY

The papers and reports listed below have been reviewed and contain information which is pertinent to the current study. In most cases they have been referred to in Section 2 above; however, in all instances the title is indicative of the area of application.

Deirmendjian, D. (July 1962) "Scattering and Polarization Properties of of Polydispersed Suspensions with Partial Absorption," The RAND Corporation, Memorandum RM-3228-PR.

Downie, C.S., and Smith, R.B. (1958) "Thermal Techniques for Dissipating Fog from Aircraft Runways," Air Force Surveys in Geophysics No. 106, AFCRC-TN-58-477.

Driving, A.J., Mironov, A.V., Morozov, V.M. and Khvostikov, I.A., (1949) "The Study of Optical and Physical Properties of Natural Fogs," Technical Translation No. IS-2, National Research Council of Canada, Division of Information Services.

East, T.W.R. and Marshall, J.S. (1954) "Turbulence in Clouds as a Factor of Precipitation," Quart. J. Roy. Meteor. Soc. 80 pp 26-37 and 47.

Fenn, R.W., (1962) "Light Scattering Measurements and the Analysis of Natural Aerosol Size Distributions," U.S. Army Signal Research and Development Laboratory, Ft. Monmouth, N.J., USASRDL Technical Report 2247.

Houghton, H.G. and Radford, W.H. (1938) "On the Local Dissipation of Natural Fog," Papers in Physical Ocean. and Meteor. VI, No. 3

Houghton, H.G. and Radford, W.H. (1939) "On the Measurement of Drop Size and Liquid Water Content in Fogs and Clouds," Papers in Physical Ocean. and Meteor. VI, No. 4.

Hulburt, E.O. (1949), "Atmospheric Attenuation for Wavelengths 2,500 to 10,000 Angstroms," Minutes and Proceedings of the Armed Forces - NRC Vision Committee, 24th Meeting, pp 45-46.

Hulburt, E.O. (1935), "Attenuation of Light in the Lower Atmosphere," J.Opt.Soc.Am. 25, No. 5 pp 125-130.

Hulburt, E.O. (1937), "Observations of a Searchlight Beam to an Altitude of 28 Kilometers," J.Opt.Soc.Am. 27 pp 377-382.

Junge, Christian (1955) "The Size Distribution and Aging of Natural Aerosols as Determined from Electrical and Optical Data on the Atmosphere." J.Meteor. 12 pp 13-25.

Junge, Christian (1958) "Methods of Artificial Fog Dispersal and their Evaluation," Air Force Surveys in Geophysics No. 105, AFCRC-TN-58-476.

Keith, C.H. and Arons, A.B. (1954) "The Growth of Sea-Salt Particles by Condensation of the Atmospheric Water Vapor," J.Meteor. 11 pp 173-184.

Knestrick, H.L., Cosden, T.H., and Curcio, J.A. (1961) "Atmospheric Attenuation Coefficients in the Visible and Infrared Regions," NRL Report 5648, Radiometry Branch Optics Division, U.S. Naval Research Laboratory, Washington, D.C.

Kurnick, S.Q., Zitter, R.N. and Williams, D.B. (1959) "Atmospheric Transmission in the Infrared during Severe Weather Conditions," CML-TN-P 145-3, The University of Chicago Laboratories for Applied Sciences.

Larmore, L. (1956) "Transmission of Infrared Radiation Through the Atmosphere," Proceedings of Infrared Information Symposium 1, No. 1 pp 14-23.

Arthur D. Little, Inc. (1956) "Warm Fog and Stratus Cloud Dissipation."

Moore, D.J. (1952) "Measurements of Condensation Nuclei over the North Atlantic," Quart.J.r.meteor.Soc., 78, 596-602.

Moore, D.J. and Mason, B.J. (1954) "The Concentration, Size Distribution and Production Rate of Large Salt Nuclei Over the Oceans," Quart.J.r. meteor.Soc. 80 p 583-590.

Nathan, A.M. (1957) "A Polarization Technique for Seeing Through Fogs with Active Optical Systems," Technical Report 362.01, N.Y. University, College of Engineering Research Division.

Passman, S. and Larmore, L. (1956) "Correction to Atmospheric Transmission Tables," Proceedings of Infrared Information Symposia, Vol. 1, No. 2, pp 15-17.

Pritchard, B.S. and Blackwell, H.R. (1957) "Preliminary Studies of Visibility on the Highway in Fog." Report 2557-2-F, University of Mich. Vision Research Laboratories.

Stewart, H.S., Drummeter, L.F. and Pearson, C.A. (1949) "The Measurement of Slant Visibility" U.S. Naval Res.Lab.Rep. 3484, Washington.

Webb, W.L. (1956) "Particulate Counts in Natural Clouds and Fogs," J.Meteor. 13 pp 203-206.

Woodcock, A.H. (1952) "Atmospheric Salt Particles and Raindrops," J.Meteor. 9 pp 200-212.

Woodcock, A.H. (1953) "Salt Nuclei in Marine Air as a Function of Altitude and Wind Force," J.Meteor. 10 pp 362-371.

Woodcock, A.H. and Gifford, M.M. (1949) "Sampling Atmospheric Sea Salt," J.marine res. 8 pp 177-197.

Wright, H.L. (1940) "Atmospheric Opacity at Valentia," Quart.J.Roy.Meteor. Soc. 80 pp 66-77.

ATMOSPHERIC ATTENUATION FOR WAVELENGTHS

2,500 to 10,000 ANGSTROMS

E.O. Hulburt
Naval Research Laboratory

Synopsis

A tabulation of the attenuation coefficients for wavelengths 2,500 to 10,000 A for air varying from hazy to very clear was made by piecing together the data of four investigations:

(1) Smithsonian Physical Tables, eighth Revised Edition, 1933, Table 767, columns 2 and 5; wavelengths 4,000 to 10,000 A.

(2) A. Vassy, Theses, University of Paris (1941); wavelengths 4,265 to 2,200 A.

(3) Optics Division, Naval Research Laboratory, now in progress; wavelengths in visible and ultraviolet.

(4) W. E. K. Middleton, "Visibility in Meterology," Chapter 2, Second Edition, University of Toronto Press (1941); visible wavelengths.

The piecing together was fairly satisfactory because of two circumstances: (1) the Smithsonian and Vassy data agreed in absolute value over a small spectral region in which they overlapped, (2) Middleton's equation,

established by him experimentally for 4,600 to 6,400 A, when extrapolated to 10,000 A, agreed with Smithsonian data but to 10,000 A.

The preliminary results are listed in Table 1 in which V is the daylight visual range and σ is the atmospheric attenuation coefficient defined by $i = i_o e^{-\sigma\lambda}$ where i_o and i are the intensities of a collimated beam of light in the wavelength interval $\alpha\,\lambda$ entering and emerging from a column of the atmosphere λ km in length. The values of σ for ultraviolet wavelengths below 3000 A in Table 1 are preliminary and may be changed to some extent when an investigation now in progress in completed. But the other values of σ will probably remain as given in Table 1.

A more complete report will eventually be published.

E.O. Hulburt, "Atmospheric Attenuation for Wavelengths 2500 to 10,000 Angstroms," Minutes and Proceedings of the Armed Forces, NRC Vision Committee, 24th Meeting 14-15 November 1949.

TABLE 1. Atmospheric Attenuation Coefficients.

	V = 10	15	20	30	40	50	60	70	80	90	100	120	km
	5.4	8.11	10.8	16.2	21.6	27.0	32.4	37.8	43.2	48.5	54.0	65.0	sea mile
λ	σ	σ	σ	σ	σ	σ	σ	σ	σ	σ	σ	σ	
2500 A	3.31	2.50	2.25	2.00	1.85	1.76	1.68	1.64	1.60	1.55	1.53	1.50	
2700	2.20	1.67	1.30	1.18	1.05	1.00	.95	.91	.88	.85	.83	.80	
3000	1.45	1.00	.76	.53	.441	.376	.336	.310	.284	.266	.245	.219	
3300	1.08	.72	.56	.39	.31	.26	.226	.203	.185	.171	.155	.135	
3500	.92	.62	.48	.330	.261	.218	.186	.167	.150	.136	.125	.108	
3700	.79	.54	.41	.278	.219	.180	.155	.137	.123	.113	.103	.082	
4000	.66	.445	.342	.230	.175	.142	.122	.107	.097	.089	.082	.072	
4300	.55	.382	.292	.195	.145	.118	.100	.088	.079	.073	.066	.058	
4500	.50	.352	.285	.175	.133	.107	.090	.080	.072	.065	.059	.051	
4700	.47	.326	.250	.164	.125	.100	.084	.074	.066	.060	.054	.046	
5000	.44	.296	.228	.148	.144	.090	.077	.066	.059	.053	.047	.040	
5300	.41	.274	.210	.137	.104	.083	.069	.059	.053	.047	.042	.036	
5500	.395	.262	.198	.129	.098	.078	.065	.056	.050	.044	.040	.033	
5700	.381	.251	.190	.123	.092	.073	.061	.052	.047	.041	.037	.031	
6000	.370	.238	.178	.114	.085	.067	.056	.048	.043	.0375	.0335	.028	
6300	.355	.225	.168	.107	.079	.062	.052	.044	.039	.034	.030	.0252	
6500	.347	.218	.162	.102	.076	.060	.049	.042	.037	.032	.029	.0236	
6700	.340	.210	.156	.099	.073	.057	.047	.040	.035	.030	.027	.0222	
7000	.330	.200	.148	.095	.069	.054	.043	.037	.032	.028	.025	.020	
7300	.320	.193	.141	.090	.066	.051	.041	.035	.030	.026	.023	.019	
7500	.315	.188	.137	.087	.064	.049	.044	.034	.029	.025	.022	.018	
7700	.310	.183	.133	.084	.062	.048	.043	.033	.028	.024	.021	.017	
8000	.300	.177	.127	.080	.059	.045	.036	.031	.026	.023	.020	.016	
8500	.296	.167	.120	.074	.054	.041	.033	.028	.024	.021	.018	.014	
9000	.274	.158	.113	.068	.050	.038	.031	.026	.022	.019	.016	.012	
9500	.260	.148	.105	.063	.046	.030	.028	.024	.020	.017	.014	.011	
10000	.250	.140	.097	.058	.042	.0320	.026	.022	.0180	.015	.013	.010	

E.O. Hulburt, "Atmospheric Attenuation for Wavelengths 2500 to 10,000 Angstroms," Minutes and Proceedings of the Armed Forces - NRC Vision Committee, 24th Meeting, 14-15 November 1949

APPENDIX B

COMPUTATION OF POWER SPECTRUM

APPENDIX B

COMPUTATION OF POWER SPECTRUM

The power spectrum of the raw seeing error data was calculated, using discrete digital techniques, in four steps:

(1) Step 1 - digitization of the raw strip chart record the theodolite error signal.

(2) Step 2 - calculation of the autocorrelation function of the input.

(3) Step 3 - calculation of the raw power spectral density by taking the cosine fourier transform of the autocovariance function calculated in Step 2.

(4) Step 4 - calculation of a refined (smoothed) power spectral density with an appropriate frequency weighting function. This step reduces the effect of dealing with a truncated (finite) input signal.

The spectral density g(f) of a signal of infinite length, I(t), is given by

$$g(f) = \int_0^\infty C(t) \cos 2\pi ft \, dt \qquad \text{(B-1)}$$

where

$$C(t) = \lim_{T \to \infty} \int_{-T}^{T} I(\tau)\, I(t+\tau)\, d\tau \qquad \text{(B-2)}$$

and $I(t)$ has been adjusted to a zero mean.

The experimentally determined $I(t)$, which we will call $I_e(t)$, has a finite length. Thus $C_e(t)$, the autocorrelation function for $I_e(t)$, is truncated, which effectively is the same as multiplication by a unit pulse $S(t)$,

$$S(t) = \begin{cases} 1 & 0 < t < T \\ 0 & t > T \end{cases} \qquad \text{(B-3)}$$

So that

$$C_e(t) \quad C(t)S(t) \qquad \text{(B-4)}$$

The spectral density of the input signal of finite length is therefore

$$g_e(f) = \int_{0}^{\infty} C_e(t) \cos 2\pi ft\, dt \qquad \text{(B-5)}$$

or

$$g_e(f) = \int_{0}^{\infty} C(t)S(t) \cos 2\pi ft\, dt \qquad \text{(B-6)}$$

The convolution property of fourier transforms states that if

$$C_e(t) = C(t)S(t)$$

then

$$g_e(f) = \int_{-\infty}^{\infty} g(f-f')s(f')\, df' \qquad \text{(B-7)}$$

where

$$s(f) = F\left[S(t) \right] = \frac{\sin f}{f} \qquad \text{(B-8)}$$

and F is the fourier integral operator.

Thus the experimental spectral density, $g_e(f)$, is the desired spectral density convoluted with a function of the form sin f/f. To obtain a closer approximation of the desired function, g(f), the computed function, $g_e(f)$, is convoluted with a function called a hamming weighting function* to smooth out the effect of the truncation of the autocorrelation function.

For discrete data points and a finite record length, Equation B-2 has the form

$$C_p = \frac{1}{n-p} \sum_{q=0}^{n-p} F_q F_{q+p} \qquad p = 0,1,2, \text{---}, m \qquad \text{(B-9)}$$

where
- n = total number of data points 1000
- m = maximum number of correlation shifts = 200
- F = experimental value of the signal
- p = index of shift interval

The combination of a finite sampling interval, r, and a finite total sample length, T, used in converting the raw theodolite error signal on the strip chart to digital data points acts as a frequency filter of the form **

$$R(f) = \left[1 - \frac{\sin^2 \pi fT}{(\pi ft)^2} \right] \left[\frac{\sin^2 \pi fr}{(\pi fr)^2} \right] \qquad \text{(B-10)}$$

*The Measurement of Power Spectra, Blackman & Tukey, Dover 1958
**Ogura and Kahn, J-Meteorol, 14, 1, p. 176.

where

$R(f)$ - response of equivalent frequency filter

T - total sample length

r - finite sampling interval

The low and high frequency cutoffs, for which $R(f) = 0.5$, are, for the cases considered here,

$$f_{high} = \frac{0.44}{r} = \frac{0.44n}{T}$$

$$f_{low} = \frac{0.44}{T} \qquad \text{(B-11)}$$

To avoid inaccuracies due to the filtering effect of the sampling technique, the spectral density has been computed only for frequencies that lie within the range defined in Equation (B-11). In terms of the sample spacing, r, which is equal to the shift interval used to compute the autocorrelation function, the computer program calculated the power density spectrum between

$$f_{min} = \frac{1}{2r},$$

and

$$f_{max} = \frac{m}{2r}.$$

These are inside the limits given by Equation B-11.

APPENDIX C

THE USE OF EDGE GRADIENTS IN DETERMINING MODULATION-TRANSFER FUNCTIONS

PHOTOGRAPHIC SCIENCE AND ENGINEERING
Volume 7, Number 6, November-December 1963

The Use of Edge Gradients in Determining Modulation-Transfer Functions

FRANK SCOTT, RODERIC M. SCOTT, AND ROLAND V. SHACK,
The Perkin-Elmer Corporation, Norwalk, Conn.

A method is described for obtaining the modulation-transfer function from an edge in an image, making the procedure especially useful for evaluation of images not containing targets. Microdensitometric data obtained from an image-edge is treated to yield the square-wave response from which the sine-wave response, or the modulation-transfer function, is determined. The method only involves the taking of finite sums and differences. In addition to a discussion of the method, a detailed example is given of two typical applications.

The increasing use of the modulation-transfer function[1] in the design and performance evaluation of optical and photo-optical systems has been accompanied by an increasing variety of methods of its measurement. One method for obtaining the modulation-transfer function, based on a principle described by one of the authors,[2] is discussed.

The procedure to be described results in a good estimate of the modulation-transfer function of systems producing images which do not contain targets normally used for measurement purposes. Instead, data obtained from an edge in the image is treated to yield the square-wave response from which the sine-wave response, or the modulation-transfer function, is determined. This method, which theoretically is exact, only involves the taking of finite sums and differences. The accuracy of the procedure is limited primarily by the practical aspects of microdensitometry and graphical techniques. The theoretical basis and the mathematical treatments involved in modulation-transfer functions have been described[3-7] and will not be discussed in this paper.

Description of Method

If an edge in an image is assumed to have a step-function brightness distribution, like a knife-edge

Received 18 July 1963.

1. E. Inglestam, *Phot. Sci. Eng.*, **5**: 282 (1961).
2. R. V. Shack, *J. Res. Natl. Bur. Std.*, **56**: 245 (1956).
3. G. C. Higgins and F. H. Perrin, *Phot. Sci. Eng.*, **2**: 66 (1958).
4. F. H. Perrin, *J. SMPTE*, **69**: 151 (1960).
5. F. H. Perrin, *J. SMPTE*, **69**: 239 (1960).
6. R. M. Scott, *Phot. Sci. Eng.*, **3**: 201 (1959).
7. R. L. Lamberts, G. C. Higgins, and R. N. Wolfe, *J. Opt. Soc. Am.*, **48**: 487 (1958).

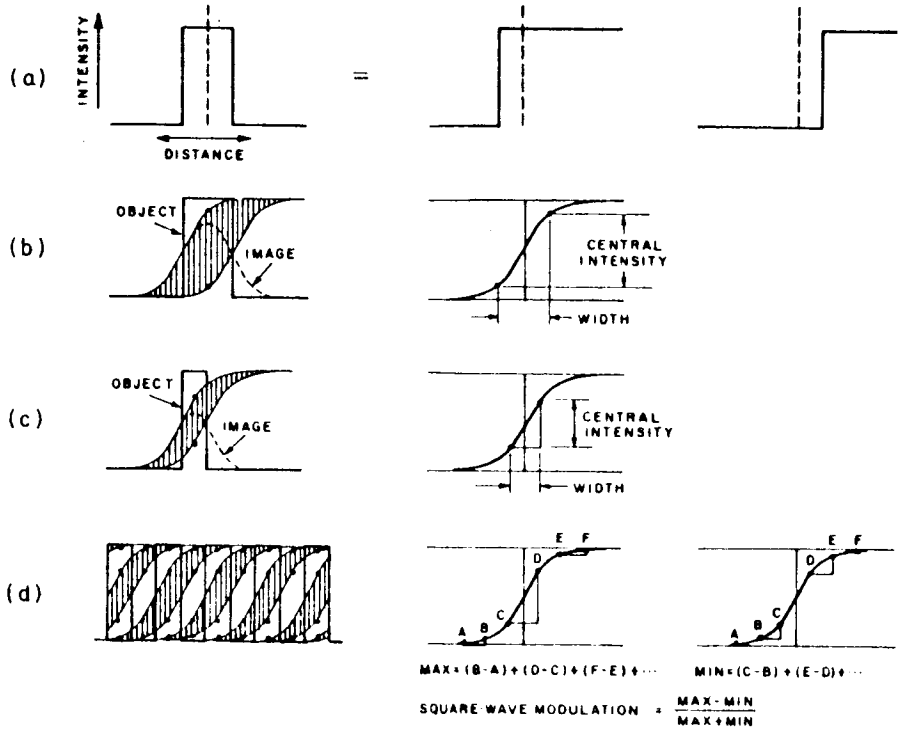

Fig. 1. Square-wave modulation from knife-edge image.

image, the image of any structure made up of sharp edges (Fig. 1a) can be calculated by the corresponding addition and subtraction of the images of each edge (Fig. 1b). Specifically, the intensity of the image of a bar of finite width can be calculated by the difference of two displaced edge-images or by the ordinate difference between two points on the knife-edge image curve plotted against the midpoint between the abscissas of the points, the separation of the points being equal to the width of the bar (Fig. 1, b and c). The central intensity of the image is obtained when the midpoint is at the center of the sharp-edge image curve.

If the object consists of bars sufficiently close together for the successive knife-edge images to overlap appreciably (Fig. 1d), the intensity at

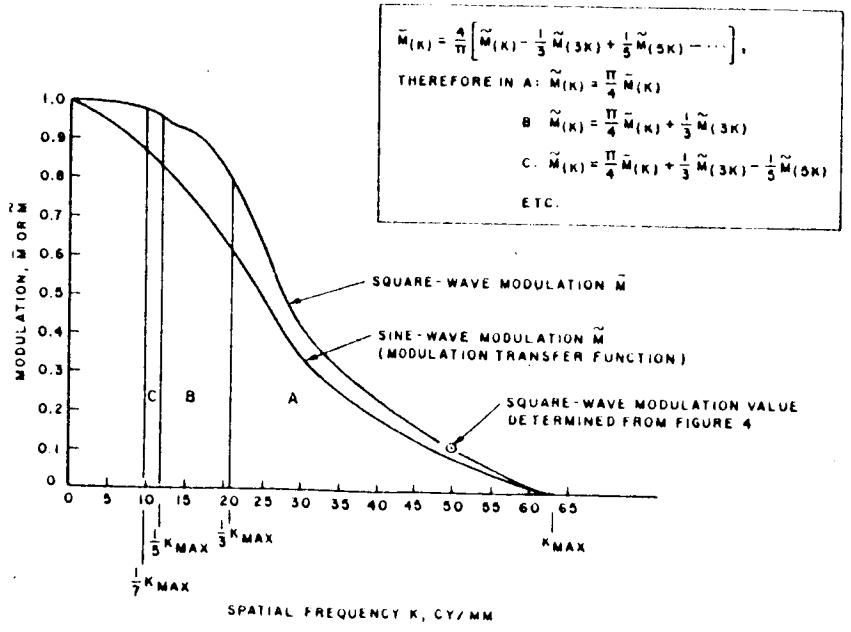

Fig. 2. Sine-wave modulation from square-wave modulation.

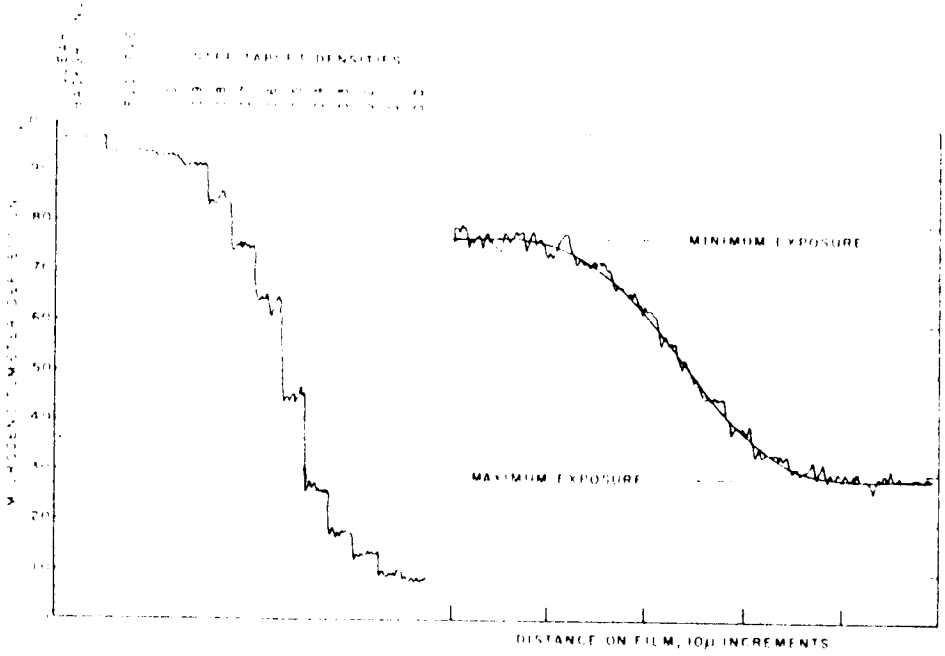

Fig. 3. Microdensitometer trace of sensitometric exposure (*left*) and image edge (*right*).

any point is the sum of the contributions from all the bars in the vicinity, or alternatively is the sum of the ordinate differences between pairs of points along the knife-edge image curve representing the bars. Thus, if the object is a square wave (bars and spaces all equal), the intensity at the center of a bar or space is obtained from the ordinate values of points equally spaced along the knife-edge image curve and straddling the center. The square-wave modulation is obtained from these two intensities by the usual formula. This procedure can be repeated for different frequencies in order to build up the square-wave modulation curve (Fig. 2).

Because the transfer function has a finite upper limit in spatial frequency, any square-wave image has only a finite number of harmonic components. In fact, for all spatial frequencies from $\frac{1}{3}$ maximum to the maximum itself, the square-wave image is itself a sine-wave, because only the fundamental can have a nonzero value. Consequently it is possible to derive the sine-wave modulation from the square-wave modulation by starting at the high-frequency end and working backwards introducing harmonic components when appropriate.

Example of Method

The determination of the modulation-transfer function of an aerial camera system is taken as an example of the use of the method. The method is, however, applicable to other optical and photographic systems or components as is briefly discussed later.

The first and most important step is to provide a sensitometric exposure on the film to be evaluated. This is done best in the camera at almost the same time as the exposure. No absolute intensity calibration is required, but care should be taken that the relative exposures are accurately known. A uniformly illuminated density step tablet is satisfactory if the duration of the exposure and the spectral quality of the illumination simulate the scene exposure. The exposures may be made at different times if the interval to processing is long enough so that any time effects between exposures and processing are minimized. From this sensitometric exposure a modified form of a characteristic (H & D) curve will be developed and the accuracy of the method depends on the accuracy of this curve.

The steps in this method, to proceed from an edge in a picture to the transfer function of the system, are as follows:

1. Select an edge in the scene which is straight for many resolution elements and is known to have a step-function brightness distribution. Examples are shadows of straight edges of buildings on smooth surfaces and the ridge of a peaked roof with different illumination on the two sides. The edge must separate two areas of uniform density which are large enough to be well resolved.

2. Trace the sensitometric density steps and the edge with the same slit and settings of the microdensitometer. The slit must be long enough (and thus the edge) to give a good trace with a minimum of grain noise. The slit must be narrow enough so that its transfer function $T(k)$ does not obscure the function of the system being evaluated.

$$T(k) = \frac{\sin \pi wk}{\pi wk}$$

where

w = effective width of slit
k = spatial frequency

Figure 3 illustrates a typical tracing.

R. L. Lamberts, *J. Opt. Soc. Am.*, **48**: 490 (1958).

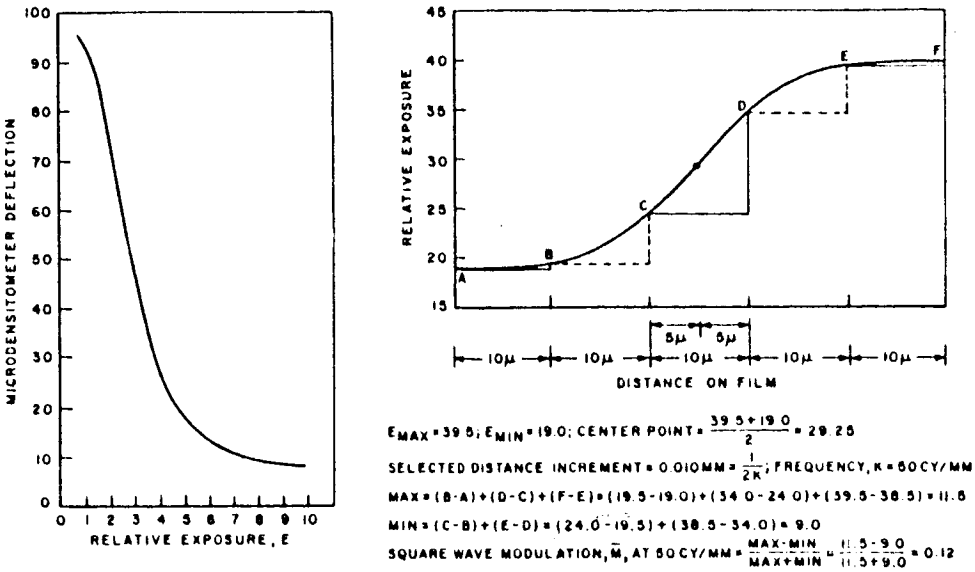

Fig. 4. Curves of sensitometric relative exposure vs. microdensitometer deflection (*left*) and relative exposure vs. distance on film of edge image (*right*)

3. Convert the deflections of the densitometer into relative exposures by plotting deflection vs. relative exposure from the sensitometric images. The left side of Fig. 4 is typical.

4. Draw a smooth curve through the edge trace (care at this point will be repaid later), convert the deflection axis to relative exposure using the curve made in Step 3, and draw the curve of relative exposure vs. displacement as shown on right side of Fig. 4. If the trace shows excessive deflections due to granularity, scan several sections of the edge and graphically average the traces.

5. Find the center of the central intensity. This point on the curve is the average exposure; that is,

$$\text{center point} = (E_{max} + E_{min})/2$$

6. Select a distance increment which is equal to $\frac{1}{2}k$ where k is a spatial frequency at which the transfer function is expected to have a value greater than zero. Center the selected distance increment on the center point and divide the remainder of the curve abscissa into the selected distance increments, as shown in Fig. 4. Determine the ordinate difference of each distance increment. Add the differences of every other increment (solid lines in Fig. 4), and consider this to be the MAX value. The MAX set must include the center increment. Add the differences of the remaining increments (dotted lines in Fig. 4), and consider this the MIN value.

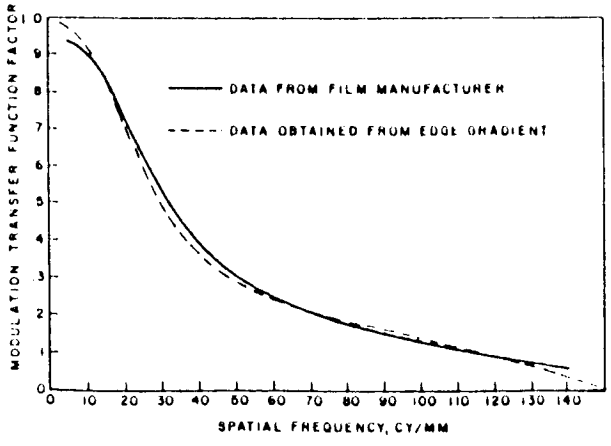

Fig. 5. Measurement of modulation-transfer function of Kodak Plus-X Aerecon Film, Type No. 8401, developed in D-19 developer for 8 min at 68° F.

7. Determine the square-wave modulation value of the selected frequency k, using the MAX and MIN values obtained in Step 6.

$$\text{Square-wave modulation} = \frac{(\text{MAX} - \text{MIN})}{(\text{MAX} + \text{MIN})}$$

As a check, MAX + MIN should equal $E_{max} - E_{min}$.

8. Repeat Steps 6 and 7 several times in each case selecting a different distance increment (spatial frequency) which will enable the plotting of the square-wave modulation curve as shown in Fig. 2.

9. Change the square-wave modulation curve to a sine-wave modulation curve. This is accomplished by treating sections A, B, C, etc. of the curve in Fig. 2 separately. In section A, consisting of the spatial frequency range of $\frac{1}{3}k_{max}$ to k_{max}, multiply the square-wave modulation M by $\pi/4$ to obtain the sine-wave modulation M.

In Section A,

$$M_A = (\pi/4)M_A$$

In Section B ($\frac{1}{3}k_{max}$ to $\frac{1}{2}k_{max}$), change the square-wave modulation to sine-wave modulation by

$$M_A = (\pi/4)M_A + \frac{1}{2}M_{3A}$$

Likewise, in Section C,

$$M_4 = (\pi/4)\,M_1 + 1/3\,M_3 - 1/5\,M_5$$

Correction for harmonic components above the 5th is usually not necessary as interpolation of the curve to a modulation value of 1.0 is adequate.

10. Remove the transfer function of the microdensitometer objective and slit which can be determined by scanning a knife-edge and applying the procedure described in this paper.

It is to be noted that this method gives the transfer function of the aerial camera system without a knowledge of the actual intensities at the target, the haze[9,10] in the atmosphere, or the wide-angle scattering in the system. This is because the brightness in the scene was assumed to be as measured photometrically in the image on the film. Thus, these effects are not determined by this method without additional knowledge of the target. Nevertheless, in those cases where only unstandardized targets are available, the method yields considerable useful information on aerial camera system performance.

Other Applications

The procedure can be applied to determine the modulation-transfer function of photo-optical devices other than aerial camera systems. For example, as mentioned in the application discussed above, the modulation-transfer function of a microdensitometer can be determined by this method.

Another example of application is the measurement of film modulation-transfer functions. Figure 5 shows the results obtained by this method and that obtained by the manufacturer.[11] The particular procedure followed in this case was:

1. An edge-image was produced on a high-resolution film.

2. The edge-image was contact-printed on the film being evaluated. The contrast of the edge-image produced in Step 1 and the exposure incident on the film in Step 2 were such that the minimum density produced on the film in Step 2 was above gross fog.

3. The film was processed along with a sensitometrically exposed film sample.

4. The processed film was scanned on a microdensitometer and the resulting edge-trace changed to an exposure distance plot using the microdensitometer trace of the sensitometric exposure.

5. The edge of Step 1 was scanned on the microdensitometer. After application of the procedure described in this paper, the transfer function of the microdensitometer plus the exposing edge was determined.

6. From the exposure distance plot of Step 4 a modulation-transfer function was produced which when divided by the modulation-transfer function produced in Step 5 yielded the film modulation-transfer function shown in Fig. 5.

Conclusions

The procedure described above gives the real part of the optical-transfer function[1] which, in the case of symmetrical line-spread functions, is equal to the modulation-transfer function. When unsymmetrical edge-traces are encountered, the imaginary part of the optical-transfer function can be determined by repeating the process using distance increments not centered on the central intensity. The repeated procedure should employ distance increments centered on points A, B, C, D, . . . in Fig. 4 and yields the Fourier sine transform of the line-spread function. As a check, this function should have its origin at zero. The modulation-transfer function is obtained by combining the first-obtained transfer function (which mathematically is the Fourier cosine transform) with the function obtained by the repeated process by taking the square root of the sum-of-the-squares.

The method for determining the modulation-transfer function discussed in this paper should not be employed when more conventional methods and suitable targets[10,12] are available yielding more accurate data. The procedure described does, however, offer a fairly rapid and accurate determination of modulation-transfer functions and is particularly useful with images not containing sine-wave or other types of targets.

Acknowledgment

The authors wish to thank Dr. R. E. Hufnagel for suggestions and Miss L. Bozak for invaluable assistance in the development of the procedure.

9. M. D. Rosenau, Jr., *Phot. Sci. Eng.*, **6**: 265 (1962).
10. M. D. Rosenau, Jr., F. Scott, and W. F. Thiessen, Jr., *Phot. Sci. Eng.*, **7**: 92 (1963).
11. *Manual of Physical Properties of Aerial and Special Materials*, Section 19, Eastman Kodak Co., Rochester, N.Y., 1963.
12. R. L. Lamberts, *Appl. Opt.* **2**: 273 (1963).

APPENDIX D

BASIC SEEING THEORY

APPENDIX D

BASIC SEEING THEORY

D-1. Introduction

The purpose of this section is to give the reader a short survey of the theory used to derive the equations used in Section II giving the dependence of the wavefront deviation on the logarithmic temperature gradient, θ^*. A complete study of this subject is given in the references quoted herein. It includes such factors as temperature and its gradient and time variation, solar radiation to the ground and to water vapor in the air, re-radiation from the ground to the air and humidity transfer between air and ground and its dependence on wind velocity and temperature. It has been found that a statistical approach to the problem can predict many of the features of the transmission of light through a turbulent atmosphere. This approach makes it unnecessary to treat all the thermodynamic variables in detail.

We proceed by defining statistical functions to describe the turbulent atmosphere and finding the variation of these functions with position. These are then used to find solutions to the wave equation, i.e., the equation for propagation of light. From such solutions, an expression for the mean square phase deviation is found in terms of variables which can be measured. Thus we arrive at equations used in the text to predict the atmospheric seeing.

D-2. Random Functions

The temperature and wind velocity at a point are random variables. Two important measures of such quantities are their mean value and their correlation function. If we let f(t) be the value of a random variable at time t_1 then we denote by $\overline{f(t_1)}$ its mean value, that is, the value of its average over the whole ensemble. Denoting by $f^*(t_2)$ the complex conjugate of $f(t_2)$ then the correlation function of f(t) for times t_1 and t_2 is

$$B_f(t_1,t_2) = \overline{\left[f(t_1)-\overline{f(t_1)}\right]\left[f^*(t_2)-\overline{f^*(t_2)}\right]} \qquad \text{(D-1)}$$

Clearly, $B_f(t_1,t_2) = B_f(t_2,t_1)$ when f is a real function and $B_f = 0$ when the quantities in the square brackets in (D-1) are independent of each other, that is, when the fluctuations of the quantity f(t) at times t_1 and t_2 are not related to each other.

A random function (i.e., a function of a random variable) is called stationary if its mean value is independent of the time. Stationary functions are more easily manipulated than other types and can sometimes be used for describing physical situations. However, they are inappropriate for many meteorological variables because these are frequently slow, smooth functions of the time of day. For this reason, the so-called "structure functions" were introduced by Kolmogorov.

D-3. Structure Functions and Homogeneous Fields

When f(t) is a (non-stationary) random function which changes with time, we consider instead of f(t) the first difference

$$F_\tau(t) = f(t+\tau) - f(t)$$

This is the change of f in time τ; and for slow, steady changes in f it will be independent of t. This new function can then be a stationary random function of time. It is now possible* to write the correlation $B_F(t_1, t_2)$ as a linear combination of so-called structure functions

$$D_f(t_i, t_j) = \overline{\left[f(t_i)-f(t_j)\right]^2}$$

(where the values of t are t_1, $t_1 + \tau$, t_2, $t_2 + \tau$). As a matter of fact, for $F_\tau(t)$ stationary, we need only consider the simpler function

$$D_f(\tau) = \overline{\left[f(t+\tau)-f(t)\right]^2} = \overline{\left[F_\tau(t)\right]^2} .$$

Consider now, for example, a meteorological parameter, f(r), which is a function of position. We will find it appropriate to apply the method of structure functions. Although the correlation, $B_f(\vec{r}_1, \vec{r}_2)$ is a function of each of the arguments separately and not just the difference, $D_f(\vec{r}_1, \vec{r}_2)$ is a function only of the difference, and we may write

$$D_f(\vec{r}_1 - \vec{r}_2) = \overline{\left[f(\vec{r}_1)-f(\vec{r}_2)\right]^2}$$

*Tatarski, V.I.; "Wave Propagation in a Turbulent Medium," McGraw-Hill, pp. 9-10.

or, in fact, if

$$\vec{r}_1 - \vec{r}_2 = r$$

$$D_f(\vec{r}_1 - \vec{r}_2) = D_f(r) \qquad \text{(D-2)}$$

where

$$r = |\vec{r}_1 - \vec{r}_2|.$$

D-4. The Parameters of Turbulence

We now proceed to apply the foregoing to the study of the change from an initially laminar flow to turbulent flow. The Reynolds number is

$$Re = \frac{vL}{\nu}$$

where

v is the velocity,

L is a characteristic length of the process, and

ν is the kinematic viscosity.

When this criterion exceeds its critical value, Re_{cr}, the character of the motion changes to turbulent flow.

If a velocity fluctuation v' occurs in a region of size ℓ in the original liminar flow, we can compute a characteristic period

$$\tau = \frac{\ell}{v'}$$

and the amount of power (per unit mass of fluid) converted to fluctuational motion is

$$\epsilon = \frac{v'^2}{\tau} = \frac{v'^3}{\ell} .$$

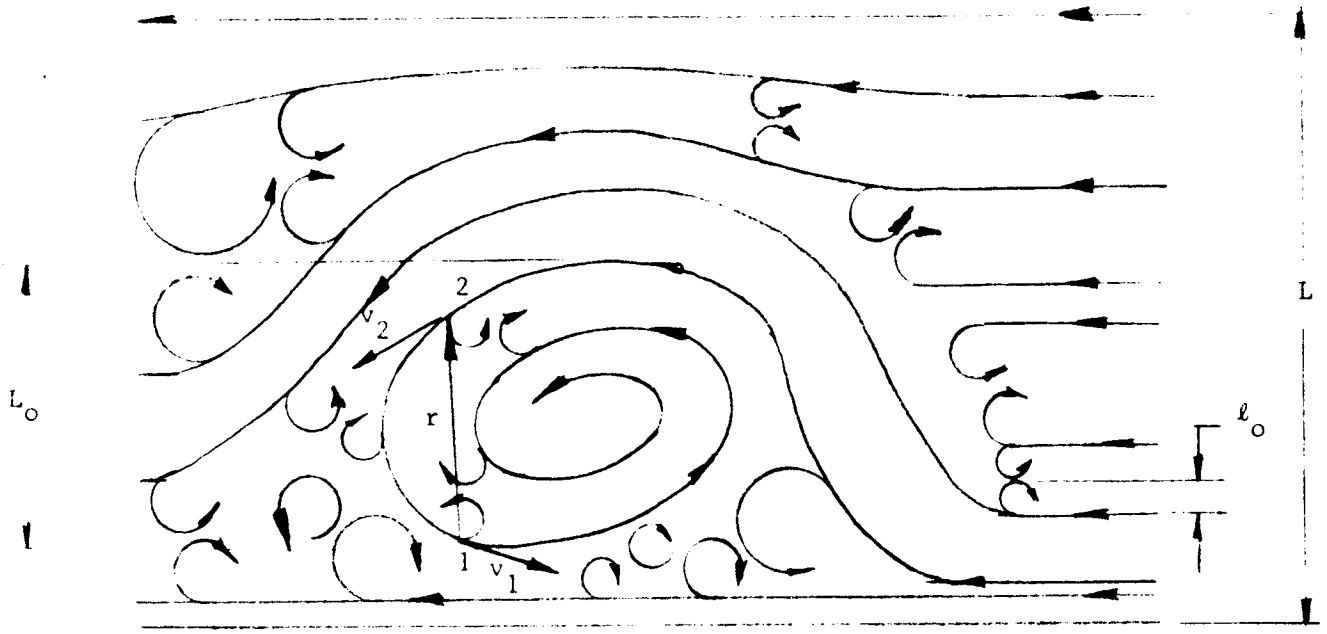

Figure D-1. Illustration of Parameters in Turbulent Flow

We will be interested in the dependence of this power on kinematic viscosity, eddy velocity and eddy size. To find this, we use dimensional analysis. Recalling that the kinematic viscosity can be written in terms of the shearing stress σ_s:

$$\nu = \frac{\sigma_s}{\frac{\partial v}{\partial y} \cdot \rho}$$

then

$$\frac{\partial v}{\partial y} \sim \frac{v'}{\ell}$$

hence, immediately

$$\nu = \frac{\sigma_s \ell}{v' \rho} \quad \text{or} \quad \frac{\nu v'}{\ell} \quad \frac{\sigma_s}{\rho}$$

Now, ϵ is the power eventually converted to heat per unit mass, hence

$$\epsilon = \frac{\text{stress x area x distance}}{\text{volume x density x time}}$$

$$\epsilon = \sigma_s \frac{\ell^2 x \ell}{\ell^3 x \rho x 1} = \frac{\sigma_s}{\rho \left(\frac{\ell}{v'}\right)} = \left(\frac{\sigma_s}{\ell \rho}\right) v'$$

and substituting ν to eliminate σ_s and ρ

$$\epsilon = \frac{\nu v'^2}{\ell^2} \qquad \text{(D-3)}$$

We call ℓ_o the inner scale of the turbulence (the size of the smallest eddies) and L_o the outer scale of the turbulence (the size of the largest, anisotropic eddies). Then the difference between velocities at points 1 and 2 is mainly due to eddies with dimensions of the order of the distance, r, from point 1 to 2. The energy transferred to an eddy of a given size comes essentially from larger eddies and is transferred in turn to smaller eddies. The rate of dissipation of energy into heat is then determined by the parameters connected with the smallest eddies and is of the order

$$\epsilon \sim \frac{\nu v_o^2}{\ell_o^2}$$

For larger eddies, the energy transferred is of the order of the kinetic energy per unit mass and thus the power transferred is

$$\epsilon \sim \frac{v_\ell^2}{\tau} \sim \frac{v_\ell^3}{\ell} .$$

Thus if we wish to write the dependence of velocity on ϵ and ℓ, we have

$$v'_\ell \sim (\epsilon \ell)^{1/3} . \qquad \text{(D-4)}$$

Now, the only parameters which can be involved in the structure function are the energy dissipation rate, ϵ, and the distance r. If we write for the structure function of the velocities

$$D_{rr} = \overline{\left(v_r - v'_r\right)^2} \qquad \text{(D-5)}$$

then we must seek a combination of r and ϵ with the dimensions of velocity squared, hence from (D-4)

$$D_{rr}(r) = C_D^2 \, (\epsilon r)^{2/3} \qquad \text{(D-6)}$$

This is referred to as the "<u>two-thirds law</u>."

By quite similar arguments, the structure function for the temperature fluctuation, $D_\theta(r)$, can be shown to obey a similar law

$$D_\theta(r) = \frac{a^2 \bar{N} r^{2/3}}{\epsilon^{1/3}}$$

where a is a numerical constant and $\bar{N}$ represents the amount of inhomogeneity which is dissipated per unit time due to molecular diffusion. For convenience, this is frequently written

$$D_\theta(r) = C_\theta^2 r^{2/3}$$

and C_θ^2 is called the structure constant for temperature.

In order to apply this directly to an analysis of wave propagation in a turbulent atmosphere, we must convert $D_\theta(r)$ to $D_n(r)$ where n is the refractive index. This is done* by starting with the empirical relationship between n and θ and then assuming that a small parcel of air is displaced vertically with adiabatic conditions holding. Taking into consideration the change of temperature and humidity with altitude, the change in index is calculated and we find

$$D_n(r) = C_n^2 r^{2/3}$$

and

$$C_n^2 = a^2 L_o^{4/3} \left(\frac{\delta N}{\delta z}\right)^2$$

where L_o is the outer scale factor and $\delta N/\delta z$ is the change of refractive index with altitude.

D-5. Electromagnetic Wave Propagation

The phase of the wave as it is propagated through the atmosphere is seen to be a direct function of distance and index of refraction. Hence for two rays, reaching two different points in the aperture of the alignment theodolite, we can write the following expression for the difference in optical length of path

$$S = \int_o^L \left[n(x_1, y_1, z_1, t) - n(x_2, y_2, z_2, t) \right] dz \qquad (D\text{-}7)$$

*Tatarski, V.I., Op.Cit., p.55ff.

where we have assumed that the path is essentially a straight line in the z direction. The value of this integral is fluctuating continuously, but if the points (x_1,y_1) and (x_2,y_2) are separated by a distance equal to the aperture diameter, and we average S over the period of observation and over the aperture we get a convenient measure of the angle of arrival and hence of the position of the return image in the focal plane of the alignment theodolite.

The angle of arrival, when S is calculated for two points at opposite edges of an aperture, D, is then $\tan^{-1} S/D$, and, for small angles, the linear displacement in the focal plane is FS/D where F is the focal length.

We now proceed to outline the method of determining S from the meteorological data using the model of a turbulent atmosphere sketched previously.

We assume that the index is close to 1.0 (as it is for air) and does not change very rapidly with distance or time. It is convenient to deal with the normalized fluctuating part of n defined by

$$N(\vec{r},t) \triangleq \left[n(\vec{r},t) - \overline{n(\vec{r})} \right] \Big/ \overline{n(\vec{r})}$$

where $\overline{n(\vec{r})}$ is the local time average of n.

In terms of N(r,t), the wave equation for a plane wave of the form

$$V(\vec{r},t) = A(\vec{r},t) \exp\left[i(kz-\omega t) \right]$$

becomes

$$\nabla^2 A + 2ik \frac{\partial A}{\partial z} + 2k^2 NA = 0. \qquad \text{(D-8)}$$

It is shown by Hufnagel and Stanley* that equation (D-8) need not be solved exactly but rather that it is only necessary to find a statistically averaged quantity. Further, they show that the significant quantity is the average mutual coherence factor

$$M(\vec{p};z) = \left\langle A(\vec{p}_1,z,t)\ A^*(\vec{p}_2,z,t) \right\rangle$$

where we are using $\vec{p}_1$ and $\vec{p}_2$ to represent vectors in the plane transverse to the direction of propagation. The solution given by them is

$$M = \left\langle \exp\left\{ ik \int_o^L \left[N(\vec{p}_1,z') - N(\vec{p}_2,z') \right] dz' \right\} \right\rangle \qquad (D\text{-}9)$$

The integral in (D-9) can be identified with that in (D-7) to within a constant factor almost equal to unity. The connection of the function S with the modulation transfer function, M, and the proof that M is a rigorous solution to the wave equation without neglecting the effects of diffraction and scintillation are important results of the paper by Hufnagel and Stanley and illustrate the power and utility of the concept of modulation transfer functions. The evaluation of the integral is facilitated by expanding the integral as a linear function of structure functions of the form

$$D_N \triangleq \left\langle \left[N(p_i,z_j) - N(p_k,z_\ell) \right]^2 \right\rangle$$

where the subscripts take on the values 1 or 2, resulting in

$$\left\langle S^2 \right\rangle = \int_o^z dz' \int_{-\infty}^{\infty} \left[D_N(r'';z') - D_N(z'';z') \right] dz'' \qquad (D\text{-}10)$$

*Hufnagel and Stanley, JOSA, v.54, p. 53ff.

where

$$r'' \triangleq \left[|p_1 - p_2| + (z'')^2 \right]^{1/2}$$

$$z'' \triangleq z_1 - z_2 \text{ and } z' \triangleq \frac{1}{2}(z_1 + z_2)$$

Thus, we have arrived at an expression for the mean square phase deviation as a function of the structure function of the index of refraction of the intervening atmosphere. This is, then, the junction point of the electromagnetic (or optical) problem with meteorological theory.

The initial inputs to the theory of turbulence are thus the gross meteorological parameters. These include the quantities involved in the heat balance, i.e., the heat fluxes out of and into a small volume of the atmosphere; also the wind velocity (as a function of height above the ground) and the heat capacities and density as functions of height. From these data, the theory predicts the characteristics of the turbulence, mainly the structure functions for temperature (or index of refraction) as functions of the path length and position. Then the theory of wave propagation will give information about the changes in the wavefront arising from the turbulence in the form of Cross Correlation functions for phase and intensity. It is only after this has been accomplished that we can arrive at the coherence function and eventually the rms deviation of the angle of arrival of the beam.

D-6. COMPARISON OF PREDICTED WITH CALCULATED SEEING DEVIATION

D-6.1 Predicted Seeing Deviation for the Perkin-Elmer Range

In the previous paragraphs we have derived an expression for mean square deviation of the phase of an electromagnetic wave passing through

a turbulent atmosphere (Equation D-10). This can be used to derive the numerical value of the rms signal from the alignment theodolite as follows: On substituting the expression for $D_N(r'',z')$ into that for $\langle S^2 \rangle$ we get

$$\langle S^2 \rangle = \int_0^z dz' C_N^2(z') \int_{-\infty}^{\infty} \left\{ \left[|\vec{P}_1 - \vec{P}_2|^2 + (z'')^2 \right]^{1/3} - (z'')^{2/3} \right\} dz''$$

and we can evaluate the inner integral so that we obtain

$$\langle S^2 \rangle = 2.91\, p^{5/3} \int_0^z C_N^2(z')\, dz' \qquad \text{(D-11)}$$

where $p = |\vec{P}_1 - \vec{P}_2|$.

For a horizontal path, $C_N^2(z')$ is constant and hence

$$\langle S^2 \rangle = 2.91\, p^{5/3}\, RC_N^2 \qquad \text{(D-12)}$$

We still do not have a useable expression for C_N^2 since our previous one contains the factor $\delta N/\delta z$. However, in the turbulent layer of air several tens of meters thick lying near the earth's surface the mean temperature follows a logarithmic law

$$\overline{\theta(h)} = \theta + \theta^* \log \frac{h}{h_o}$$

and hence

$$\frac{d\bar{\theta}}{dh} = \frac{\theta^*}{h}$$

From this, and the relation between temperature and index of refraction we find that

$$C_N(h) = 1.3 \left| \frac{d\bar{\theta}}{dh} + 0.98 \times 10^{-4} \right|^{2/3} h \times 0.9 \times 10^{-6} \qquad \text{(D-13)}$$

where 0.9×10^{-6} is the rate of change of index of refraction with temperature, 0.98×10^{-4} is the atmospheric adiabatic lapse rate and the factor 1.3 is experimentally determined. This formula holds only for unstable conditions $\left(\frac{d\theta}{dh} \text{ negative}\right)$ common on clear, sunny days. On substituting the value of $\frac{d\bar{\theta}}{dh}$ and neglecting small quantities

$$C_N(h) = 1.17 \times 10^{-6}\, \theta^* h^{-1/3} \qquad \text{(D-14)}$$

From this last equation, we see that a measurement of the temperature gradient $\left(\frac{d\theta}{dh}\right)$ will give $C_N(h)$ as a function of the height above the ground. Knowing C_N we can find $\langle s^2 \rangle$ and then we can find the rms error signal generated in the alignment theodolite since

$$\sigma_e = \frac{\left[\langle s^2(w) \rangle\right]^{1/2}}{w} \qquad \text{(D-15)}$$

In the actual experimental configuration, h was not a constant but varied from 3 feet to 9 feet from one end of the range to the other. Since C_N^2 is a function of h, we must find a suitable average value of h. This can be found by defining the equivalent path height, h_{eq}, according to

$$\int_o^R C_N^2\, dz = (1.17 \times 10^{-6}\, \theta^*)^2 \int_o^R h^{-2/3}\, dz$$

$$= (1.17 \times 10^{-6}\, \theta^*)^2\, h_{eq}^{-2/3}\, R$$

Along the outgoing path of the range used,

$$h = h_o + \alpha z = h_o + \frac{h_1 - h_o}{R} z$$

where $h_o = 3$ ft and $h_1 = 9$ ft.

Performing the integration above, we find

$$Rh_{eq}^{-2/3} = \frac{3h_o^{1/3}}{2} \left[\left(1 + \frac{\alpha R}{h_o} \right)^{1/3} - 1 \right]$$

and substituting the values of α, h_o, and h_1, we find

$$h_{eq} = 5.55 \text{ feet} = 169.2 \text{ cm}$$

so that

$$C_N(h) = 0.212 \times 10^{-6} \theta^* \qquad \text{(D-16)}$$

In practice, θ^* is found by plotting θ versus log h and measuring the slope of the faired curve. We now have all the quantities required to find $\langle s^2 \rangle$ from Equation (D-11) and σ_e, the error output, is found from Equation (D-15).

D-6.2 Aperture Correction Factor

Equation (D-15) was derived on the basis of the phase structure function given in Equation (D-10), where an expression for the difference in phase of the incoming wavefront between two points separated in a horizontal plane was found. In the real case of a theodolite using a prism, this phase difference between two points separated in azimuth is averaged over the vertical height of the prism, thereby reducing the "strength" of the seeing.

The factor σ_{eff}/σ_e, which represents reduction in the rms seeing predicted by Equation (D-15) due to this vertical averaging effect, can be found as follows.

Consider the aperture shown in Figure D-2. The average squared difference in the angle of arrival of the wavefront can be found as the square of the average of the wavefront deviations seen by the pairs of points 1 and 2, 3 and 4, and 5 and 6.

That is,

$$\left(\frac{\sigma_{eff}}{\sigma_e}\right)^2 = \frac{1}{9}\left\langle\left[(\phi_1-\phi_2)+(\phi_3-\phi_4)+(\phi_5-\phi_6)\right]^2\right\rangle$$

which can be written as

$$\left(\frac{\sigma_{eff}}{\sigma_e}\right)^2 = \frac{1}{9}\Big\langle(\phi_1-\phi_2)^2+(\phi_3-\phi_4)^2+(\phi_5-\phi_6)^2$$
$$+2\left[\phi_1\phi_3-\phi_1\phi_4+\phi_1\phi_5-\phi_1\phi_6-\phi_2\phi_3+\phi_2\phi_4\right.$$
$$\left.-\phi_2\phi_5+\phi_2\phi_6+\phi_3\phi_5-\phi_3\phi_6-\phi_4\phi_5+\phi_4\phi_6\right]\Big\rangle$$

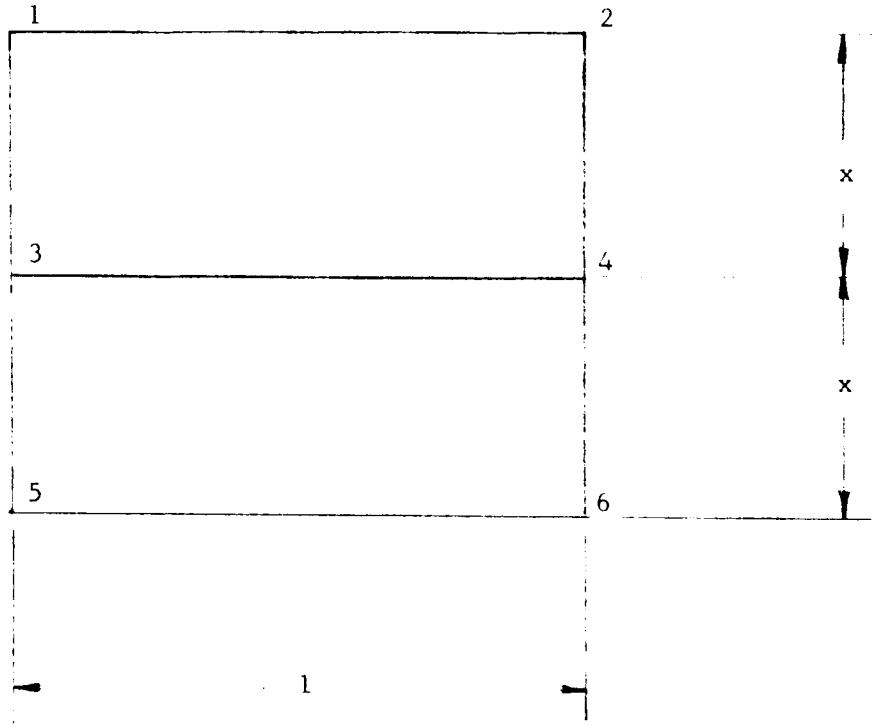

Figure D-2. Notation for Calculating Aperture Correction

In order to evaluate this equation we must consider the phase structure function of the wavefront deviations at the theodolite aperture. The phase structure function is defined as

$$D_{\phi\phi}(r_{ij}) = \left\langle \left[\phi(r_i) - \phi(r_j) \right]^2 \right\rangle \qquad \text{(D-17)}$$

where r_i and r_j are two points in the entrance aperture of the theodolite, and

$$r_{ij} = \left| \vec{r}_i - \vec{r}_j \right| .$$

Thus, the first three terms on the righthand side of Equation (2.14) can be written in the notation of Equation (D-16).

$$\left\langle (\phi_1 - \phi_2)^2 + (\phi_3 - \phi_4)^2 + (\phi_5 - \phi_6)^2 \right\rangle$$

$$= D(r_{12}) + D(r_{34}) + D(r_{56}) \qquad \text{(D-18)}$$

In order to simplify the 12 remaining terms we expand Equation (2.15)

$$D_{\phi\phi}(r_{ij}) = 2 \left\{ \left\langle \phi^2(r_i) \right\rangle - \left\langle \phi(r_i)\phi(r_j) \right\rangle \right\}$$

so that

$$\left\langle \phi_i \phi_j \right\rangle = \left\langle \phi^2(r_i) \right\rangle - \frac{1}{2} D_{\phi\phi}(r_{ij}) \qquad \text{(D-19)}$$

Substituting these into Equation (D-16) yields

$$9 \left[\frac{\sigma_{eff}}{\sigma_e} \right]^2 = D(r_{12}) + D(r_{34}) + D(r_{56}) - D(r_{13}) + D(r_{14})$$
$$+ D(r_{23}) - D(r_{24}) - D(r_{15}) + D(r_{16}) + D(r_{25})$$
$$- D(r_{26}) - D(r_{35}) + D(r_{36}) + D(r_{45})$$
$$- D(r_{46}) + 2 \sum_{i=1}^{6} (-1)^i \left\langle \phi^2(r_i) \right\rangle \qquad \text{(D-20)}$$

The condition of the isotropy and homogeneity of the atmosphere allows us to conclude that the statistics of the wavefront deviations remain constant over the entire aperture. Thus the values of

$$\left\langle \phi^2(r_i) \right\rangle$$

are all equal and the last term on the right-hand side of Equation (D-20). equals zero. Equation (D-16) then becomes

$$\left[\frac{\sigma_{eff}}{\sigma_e} \right]^2 = \frac{1}{9} \left[3D(1) - 4D(x) - 2D(2x) + 4D\left(\sqrt{1+x^2}\right) + 2D\left(\sqrt{1+4x^2}\right) \right] \qquad \text{(D-21)}$$

where the r_{ij}'s have been expressed in terms of the dimensions defined in Figure D-2.

The Kolmogoroff nature of atmospheric turbulence allows us to write the phase structure functions as follows:

$$D(y) = |\, y \,|^{5/3}$$

Thus, Equation (D-21) becomes

$$\left[\frac{\sigma_{eff}}{\sigma_e} \right]^2 = \frac{1}{9} \left[3 - 4x^{5/3} - 2\left(2^{5/3}\right)x^{5/3} + 4\left(1+x^2\right)^{5/6} + 2\left(1+4x^2\right)^{5/6} \right]$$

$$= \frac{1}{9} \left[3 - 10.36x^{5/3} + 4\left(1+x^2\right)^{5/6} + 2\left(1+4x^2\right)^{5/6} \right] \qquad \text{(D-22)}$$

Table D-1 below, shows the values of σ_{eff}/σ_e as a function of the prism dimension parameter x.

Table D-1

x	$\frac{\sigma_{eff}}{\sigma_e}$
0	1
0.2	.97
0.5	.95
1.0	.91
2.0	.85

It is worth noting that no meaningful reduction in atmospheric seeing is gained by changing the shape of the aperture within the practical limits for x shown in Table D-1.

D-6.3 RMS Seeing at Wilton

Equation (D-15) should then be modified by inclusion of the factor $B = \sigma_{eff}/\sigma_e$

$$\sigma_{eff} = \frac{B}{w} \left[\left\langle S^2(w) \right\rangle \right]^{1/2}$$

Substituting Equation (D-12), we find

$$\sigma_{eff} = \frac{B}{w} \left[2.91\, w^{5/3}\, ARC_N^2 \right]^{1/2} \qquad \text{(D-23)}$$

where A = 3.5 accounts for the fact that the theodolite beam traverses the same volume of air twice.

Substituting Equations (D-14) and (D-16) and the value of B for x = 0.5, corresponding to a square target prism, we find

$$\sigma_e = (0.95)(2.91x35)^{1/2}(1.17x10^{-6})\theta^* R^{1/2} h_{eq}^{-1/3} w^{-1/6} \qquad (D\text{-}24)$$

For the Wilton Seeing Range, the following parameters apply

$R = 850$ feet

$h = 5.5$ feet

$W = 1\text{-}1/2" = 0.125$ foot

Thus, Equation (D-24) becomes

$$\sigma_{eff} = \frac{(3.55)(850)^{1/2}\theta^*}{(5.5)^{1/3}(0.125)^{1/6}} = 83x10^{-6}\theta^* \text{ radians}$$

or

$$\sigma_{eff} = 17.1\ \theta^* \text{ arc seconds} \qquad (D\text{-}25)$$

D-6.4 RMS Seeing at Cape Kennedy

Substituting Equation (D-12) into (D-15) yields

$$\sigma_e^2 = \frac{3.5x2.91xw^{5/3}}{w^2} \int_o^{z'} C_N^2(z')\, dz' \qquad (D\text{-}26)$$

At Cape Kennedy the elevation angle of the line of sight from the theodolite to the target prism was 25° so that the height varies along the path according to

$$z' = h/\sin\alpha$$

where h is the altitude of any point on the path and $\alpha = 25°$.

Equation (2.23) thus becomes

$$\sigma_e^2 = \frac{10.4}{w^{1/3}\sin\alpha} \int_{h_o}^{h_m} C_N^2(h)\, dh$$

where

h_m = maximum altitude of optical path

and

h_o = minimum altitude of optical path.

Substituting C_N^2 from Equation (2.12) we find that

$$\sigma_e^2 = \frac{10.4(\theta^*)^2}{w^{1/3}\sin^2\alpha} (1.17\times10^{-6})^2 \int_{h_o}^{h_m} h^{-2/3}\, dh$$

$$= \frac{31.2(\theta^*)^2}{w^{1/3}\sin^2\alpha} (1.17\times10^{-6})^2 \left[h_m^{1/3} - h_o^{1/3} \right]$$

Then

$$\sigma_e = \frac{(31.2)^{1/2}(1.17\times10^{-6})\theta^*}{w^{1/6}\sin\alpha} \left[h_m^{1/3} - h_o^{1/3} \right]^{1/2}.$$

For the path of interest at Cape Kennedy,

h_m = 185 feet

h_o = 12 feet

α = 25 degrees

w = 0.167 foot = 2 inches

so that

$$\sigma_e = \frac{(15.4\times10^{-6})\theta^*}{w^{1/6}} \left[h_m^{1/3} - h_o^{1/3} \right]^{1/2} \qquad \text{(D-27)}$$

$$= 38.3\times10^{-6}\ \theta^* \text{ radians}$$

$$= 7.9\ \theta^* \text{ arc seconds.}$$

APPENDIX E

BIBLIOGRAPHY

APPENDIX E

BIBLIOGRAPHY

E-1

Blackman and Tukey, "The Measurement of Power Spectra," Dover, 1958.

Borne and Wolfe, "Principles of Optics," Macmillan, 1959.

O. G. Sutton, "Micrometeorology," McGraw-Hill, 1953.

Tatarski, V. I., "Wave Propagation in a Turbulent Medium," McGraw-Hill.

E-2

D. L. Fried and J. D. Cloud, "The Phase Structure Function for an Atmospherically Distorted Wave Front," Technical Memorandum No. 192, North American Aviation, Inc.

Hufnagel, R. H., and Stanley, N. R., "Modulation Transfer Function Associated With Image Transmission Through Turbulent Media," JOSA, Vol. 54, No. 1, Jan. 1964.

Interim Technical Report - PE Engineering Report No. 7756.

A. Offner, "Optical Design and Modulation Transfer Functions," Presentation given at Symposium held at Perkim-Elmer on March 6, 1963.

Ogara and Kahn, "A Bandpass Filter Technique for Recording Atmospheric Turbulence," British Journal Applied Phys. Vol. 14, 1963.